Design and Control of Dual Active Bridge Converter for Off-Board EV Charging Applications

Dissertation submitted to
Visvesvaraya National Institute of Technology, Nagpur
in partial fulfilment of the requirements for the award of
the degree

Master of Technology
In
Power Electronics and Drives

by
Aditya Sunil Kulkarni
(MT23PED001)

Under the guidance of

Dr. Pradyumn Chaturvedi

Department of Electrical Engineering
Visvesvaraya National Institute of Technology
Nagpur 440010 (India)

June 2025

Design and Control of Dual Active Bridge Converter for Off-Board EV Charging Applications

Dissertation submitted to
Visvesvaraya National Institute of Technology, Nagpur
in partial fulfilment of the requirements for the award of
the degree

Master of Technology
In
Power Electronics and Drives

by
Aditya Sunil Kulkarni
(MT23PED001)

Under the guidance of

Dr. Pradyumn Chaturvedi

Department of Electrical Engineering
Visvesvaraya National Institute of Technology
Nagpur 440010 (India)

June 2025

© Visvesvaraya National Institute of Technology (VNIT) 2009

Department of Electrical Engineering
Visvesvaraya National Institute of Technology, Nagpur

Declaration

I, **Aditya Sunil Kulkarni**, hereby declare that this dissertation titled "**Design and Control of Dual Active Bridge Converter for Off-Board EV Charging Applications**" is carried out by me in the Department of Electrical Engineering of Visvesvaraya National Institute of Technology, Nagpur. The work is original and has not been submitted earlier whole or in part of the award of any degree/diploma at this or any other institution/University.

Aditya Sunil Kulkarni
Date: 30/05/2025

Certificate

This is to certify that the dissertation titled "**Design and Control of Dual Active Bridge Converter for Off-Board EV Charging Applications**" is submitted by **Aditya Sunil Kulkarni** in partial fulfillment of the requirements for the award of the degree of **Master of Technology in Power Electronics and Drives** VNIT Nagpur. The work is comprehensive, complete and fit for final evaluation.

Dr. Pradyumn Chaturvedi
Associate Professor,
Department of Electrical Engineering
VNIT, Nagpur

Dr. B. S. Umre
Professor and Head,
Department of Electrical Engineering
VNIT, Nagpur
Date: 30.05.2025

Dr. A. Narendrababu
Assistant Professor,
Department of Electrical Engineering
VNIT, Nagpur

Visvesvaraya National Institute of Technology

Nagpur

Non-Plagiarism Certificate

Certified that M. Tech Dissertation titled "Design and Control of Dual Active Bridge Converter for Off-Board EV Charging Applications" submitted by Aditya Sunil Kulkarni, Enrollment No.:MT23PED001, ID NO.:30557 has been checked for plagiarism including references using TURNITIN software and the overlap is found within prescribed limits. A summary of report is given below.

ORIGINALITY REPORT			
16%	10%	14%	4%
SIMILARITY INDEX	INTERNET SOURCES	PUBLICATIONS	STUDENT PAPERS

Name: Aditya Sunil Kulkarni

Enrollment No.: MT23PED001

ID No.: 30557

30/05/2025

Project Guide: Dr. Pradyumn Chaturvedi
Associate Professor,
Department of Electrical Engineering
VNIT, Nagpur

30/5/25

Project Co-Guide: Dr. A. Narendrababu
Assistant Professor,
Department of Electrical Engineering
VNIT, Nagpur

ACKNOWLEDGEMENT

I take this opportunity to express my deepest gratitude to my guide, **Dr. Pradyumn Chaturvedi**, for his invaluable guidance, constant encouragement, timely suggestions, and constructive feedback throughout my research work. His support and the excellent research facilities at the **Power Electronics Research Lab (PERL)** significantly contributed to the successful completion of my research.

I sincerely acknowledge the guidance and support extended by **Mr. Sabarish Kalyanaraman** (IC Systems Architect, Power Conversion) and **Mr. Deepak K.** (Application Engineer) from **Texas Instruments, Bengaluru**. This project is the outcome of joint research work conducted between Power Electronics Research Laboratory (PERL) and Texas Instruments, Bengaluru.

I am profoundly grateful to **Prof. B.S. Umre**, Head of the Electrical Engineering Department at VNIT, Nagpur.

I also extend my sincere thanks to the PhD scholars, Saurabh Kamble, Akshaya Bonde, Sajid Sheikh and Aman Sheikh for their assistance during my project work. Their willingness to clarify my doubts and provide solutions whenever I approached them was invaluable.

Finally, I acknowledge the immense encouragement and support provided by my family, friends, and colleagues. Their support, along with the blessings of the God, has been fundamental to my achievements.

ABSTRACT

Modern Electric Vehicle (EV) technologies have shown significant development in the power electronic converter topologies which are being implemented at the various power conversion states. Whether it may be for On-Board (OBC) EV charging applications or for Off-Board EV charging applications. Isolated DC-DC converters play a crucial role in guaranteeing safety, minimizing noise, facilitating voltage level translation and improving overall power electronic system reliability and performance in a wide range of EV charging applications.

However, recent trends in the EV charging infrastructure shown that the majority of the EVs are taken on off-board charging mode due to the Reduced vehicle weight and Cost, Faster charging times, Improved thermal management, Integration with the grids and Smart charging. That generates requirement of a converter that can have High Power Capability in addition to the stated applications. One such prominent topology is a Dual Active Bridge (DAB) Converter. The DAB converter offers significant advantages, including Galvanic isolation, Bidirectional power flow, Inherent soft switching and High-frequency operation with High-power density which altogether improves safety, flexibility and efficiency in power electronic applications.

Considering the charging and discharging mode of EVs taking in account the bidirectional mode of operation in case of Vehicle-To-Grid (V2G) and Grid-To-Vehicle (G2V); The controller needs is designed which can have High loop bandwidth, Faster response time, and better adoption to the uncertainties in the system such as sudden load change or transition from Constant Current (CC) to Constant Voltage (CV) mode.

An appropriate mathematical model of the converter system with low model complexity and excellent large signal and small signal accuracy is developed for designing a robust control architecture for the system which can give better adaptability and improve the overall performance of the converter. Considering this possibilities and challenges for both simulation and hardware part, A mathematical model of the DAB converter along with Peak Current Mode Control (PCMC) for a digital controller is developed and has been verified via simulation and experimental results.

LIST OF FIGURES

Fig.1.1. Block diagram representation of EV charging infrastructure 1

Fig.1.2. CLLC Resonant Converter circuit diagram 4

Fig.1.3. Dual Flyback Converter circuit diagram 5

Fig.1.4. Dual Active Bridge (DAB) Converter circuit diagram 6

Fig.2.1. Dual Active Bridge (DAB) Converter circuit diagram 9

Fig.2.2 (a). Simplified circuit representation of DAB Converter 10

Fig.2.2 (b). Phasor Diagram of Forward power flow 11

Fig.2.2 (c). Phasor Diagram of Reverse power flow 11

Fig.2.3. Switching configuration during different modes of DAB 12

Fig.2.4. Circuit Diagram of DAB Converter with Different Phase Shift Ratios (D) 14

Fig.2.5. Zero Voltage Switching Capacitor charge and Discharge 16

Fig.2.6. Zero Voltage Switching Diode Conduction 17

Fig.2.7. Instantaneous Inductor Current in DAB 17

Fig.2.8. Inductance (L) vs Output Power (P_0) vs Phase shift (Ø) 20

Fig.2.9. Inductance (L) vs Phase shift (Ø 21

Fig.2.10. Output Power (P_0) vs Phase shift (Ø) at switching frequency of 100kHz 21

Fig.2.11. Waveforms of Primary Voltage, Secondary Voltage and Inductor Current divided into different time intervals 23

Fig.2.12. Gate Pulses for Primary side and secondary side bridge switches 23

Fig.2.13. Soft Switching of Primary side switch (S_1) 24

Fig.2.14. Soft Switching of Primary side switch (S_2) 24

Fig.2.15. load voltage, load current, and output current of secondary side bridge 24

Fig.3.1. Large Signal Diagram of Reduced-order Modelled DAB Converter 27

Fig.3.2. Circuit Diagram of DAB Converter Considering Parasitic Elements 28

Fig.3.3. Comparison of Large Signal Models 30

Fig.3.4. Circuit Diagram of Dual Active Bridge Converter 32

Fig.3.5. Waveforms of DAB Converter under SPS control 32

Fig.3.6. Charging Characteristics of Li-ion Battery (EV battery) 38

Fig.3.7. CC-CV Mode of Charging as Per Design Parameters 39

Fig.3.8. Bode Plot of Open Loop Plant Transfer Function ($G_{v\emptyset}(s)$) 40

Fig.3.9. Bode Plot of Open Loop Plant Transfer Function ($G_{i\emptyset}(s)$) 41

Fig.3.10. Simulation Setup for Signal Injection Technique Using PLECS 42
Fig.3.11. Obtained bode plots of Analytical and Simulated results Using PLECS 43
Fig.4.1. Proposed Control Architecture of DAB converter for EV charging 46
Fig.4.2. Circuit Diagram Depicting Voltage Mode Control of DAB Converter 47
Fig.4.3. Control System Block Diagram for Voltage Mode Control 48
Fig.4.4. Control System Block Diagram for Current Mode Control 49
Fig.4.5. Control System Block Diagram for Voltage Mode Control 52
Fig.4.6. Bode Plot of Compensated Loop Gain Transfer Function 52
Fig.4.7. Bode Plot of Closed Loop Transfer Function With Calculated Controller Parameters 53
Fig.4.8. Control System Block Diagram for Current Mode Control 54
Fig.4.9. Bode Plot of Closed Loop Transfer Function With Calculated Controller Parameters 55
Fig.4.10. Comparing reference voltage (3.3V) with the sensed load voltage (output of feedback sensor gain) which was brought down on the scale of 3.3V 55
Fig.4.11. Load Voltage and Load Current with Varrying Load Conditions 56
Fig.4.12. Load Voltage with Overshoots at Each Instant of Load Change Before it Settles Down at Constant Voltage 56
Fig.4.13. Load Voltage, Load Current and Phase Shift with Varrying Load Conditions for CV mode 57
Fig.4.14. Load Voltage, Load Current and Inductor Current with Varrying Load Conditions (50%-25%) for CV mode 57
Fig.4.15. Load Voltage and Load Current with Varrying Load Conditions 58
Fig.4.16. Comparing reference current (3.3V) with the sensed load current (output of feedback sensor gain) which was brought down on the scale of 3.3V 58
Fig.4.17. Primary Bridge Output Voltage (V_1), Primary Voltage (V_P), Inductor Current (I_L) and Secondary Voltage (V_S) for 50% Loading 59
Fig.4.18. Constant Load Current, Primary Bridge Output Voltage (V_1) and Secondary Voltage (V_S) for 50% Loading 59
Fig.4.19. Constant Load Current, Primary Bridge Output Voltage (V_1) and Secondary Voltage (V_S) for 100% Loading 60
Fig.4.20. Bode Plot of Uncompensated Loop Gain Transfer Function ($G_{L0}(s)$) 61

Fig.4.21. Bode Plot of Compensated Loop Gain Transfer Function ($G_L(s)$) 62
Fig.4.22. Load Voltage and Load Current with Varrying Load Conditions using Approach-2 for CV mode 63
Fig.4.23. Load Voltage and Load Current with Varrying Load Conditions Using Approach-2 for CC Mode 64
Fig.4.24. Bode Plot of Compensated Loop Gain Transfer Function ($G_L(s)$) (Zoomed) 64
Fig.4.25(a). Bode Plot of Compensated Loop Gain Transfer Function ($G_L(s)$) with Crossover Frequency of 1kHz 65
Fig.4.25(b). Bode Plot of Compensated Loop Gain Transfer Function ($G_L(s)$) with Crossover Frequency of 1kHz (Zoomed) 65
Fig.4.26(a). Load Voltage and Load Current with Varrying Load Conditions using New Compensation Parameters (1kHz Crossover Frequency) for CV Mode 66
Fig.4.26(b). Load Voltage with New Compensating Parameters (Zoomed) 66
Fig.4.26(c). Load Voltage and Load Current with Varrying Load Conditions using New Compensation Parameters (1kHz Crossover Frequency) for CC Mode 67
Fig.4.27. Peak Current Mode Control of DAB Converter 69
Fig.4.28. Bode Plot of Open Loop Gain ($G_{vi}(s)$) Peak Current Mode Control of DAB Converter 72
Fig.4.29. Bridge Output Voltage (V1), Transformer Primary Voltage (VP) and Inductor Current (IL) Implemented Using PCMC for 100% Loading (zoomed) 72
Fig.4.29. CV Mode Analysis of DAB Converter as per Design Parameters Comparison of Peak of Inductor Current During Transition Period, Without PCMC, With PCMC 73
Fig.5.1 High Level Block Diagram for Design of Dual Active Bridge (DAB) Converter 75
Fig.5.2 UCD3138A Working Flow Block Diagram 76
Fig.5.3 Hardware Setup of Dual Active Bridge (DAB) Converter 77
Fig.5.4 Case-1 (100/100V) Dual Active Bridge (DAB) Converter (50kHz) 78
Fig.5.5 Case-2 (100/100V) Dual Active Bridge (DAB) Converter (50kHz) 79
Fig.5.6 Case-3 (100/100V) Dual Active Bridge (DAB) Converter (100kHz) 80
Fig.5.7 Case-4 (100/75V) Dual Active Bridge (DAB) Converter (100kHz) 81

LIST OF TABLES

Table 1.1. Classification of DC-DC converters	3
Table 2.1. Comparison of Various Phase Shift Control Techniques	15
Table 2.2. Design Parameters of DAB	22
Table.3.1. Summary of Comparison of Various Modelling Methods for DAB Converter	31
Table 3.2. Design Parameters of DAB	40
Table 4.1. Comparison of Various Controller Design Techniques	68
Table 4.2. Design Parameters of DAB	71
Table 5.1 Specification of Components	77
Table 5.2 Design Parameters for Hardware setup	78
Table 5.3 Design Parameters for Hardware setup	80

NOMENCLATURE

EV	:	Electric Vehicle
G2V	:	Grid to Vehicle
V2G	:	Vehicle to Grid
DAB	:	Dual Active Bridge
SPS	:	Single Phase Shift
EPS	:	Extended Phase Shift
DPS	:	Dual Phase Shift
TPS	:	Triple Phase Shift
V_i	:	Input Voltage
V_1	:	Inverter Output Voltage
V_p	:	Transformer Primary Voltage
Vs	:	Transformer Secondary Voltage
∅	:	Phase Shift angle
S_1~S_4	:	Primary Side Switches
S_5~S_8	:	Secondary Side Switches
S_{C1}~S_{C4}	:	Capacitors of Primary Side Switches
S_{C5}~S_{C8}	:	Capacitors of Secondary Side Switches
V_0	:	Output Voltage
L	:	Inductor
HFT	:	High Frequency Transformer
$G_{v\emptyset}(s)$	:	Phase shift to Load voltage Transfer Function
$G_{i\emptyset}(s)$	:	Phase Shift to Load Current Transfer Function
K_p	:	Proportional Term
K_i	:	Integral term

LIST OF PUBLICATIONS

1. Aditya Kulkarni, H. R. Bhawane, P. Chaturvedi and S. Kamble, "Optimized Dual Phase Shift Control for Dual Active Bridge DC-DC Converter," 2024 IEEE International Conference on Power Electronics, Drives and Energy Systems (PEDES), Mangalore, India, 2024, pp. 1-6, doi: 10.1109/PEDES61459.2024.10961877.

2. Aditya Kulkarni, Shashi K Kondoju, P. Chaturvedi, “Parameter Identification and Controller Design of DAB Converter for Off-Board EV Charging Applications,” 2025 IEEE International Conference on Power Electronics Converters in Transportation and Energy Application (PECTEA), Bhubaneswar, India, 2025, pp 1-6 (*Accepted*)

INDEX

Abstract……. i

List of Figures…… ii

List of Tables…… v

Nomenclature……. vi

List of Publications……. vii

1 INTRODUCTION…… 1

1.1 Literature Review

1.1.1 Isolated Bidirectional DC-DC Converter (IBDC) Topologies……. 2

1.1.2 Dual Active Bridge (DAB) Converter……. 5

1.2 Research Gaps and objectives of Dissertation……. 7

1.3 Dissertation Overview……..... 8

2 DUAL ACTIVE BRIDGE DC-DC CONVERTER…… 9

2.1 Operating Principle

2.2 Working…… 11

2.3 Control Techniques of Dual Active Bridge (DAB) Converter…… 13

2.4 Soft Switching Operation…… 15

2.4.1 Soft Switching operation……. 16

2.4.2 Impact of Voltage Conversion Ratio(d) on soft Switching of DAB 17

2.5 Design Considerations…… 19

2.6 Simulation Results……. 22

2.6.1 Open loop operation…… 22

2.7 Conclusion……. 25

3 MODELLING OF DUAL ACTIVE BRIDGE CONVERTER…… 26

3.1 Various Modelling Techniques DAB Converter……. 26

3.2 Reduced Order Modelling of DAB Converter…… 31

3.3 Transfer Function of DAB Converter for Constant Voltage (CV) mode and Constant Current (CC) mode…… 37

3.3.1 Charging Characteristics of EV Battery……. 38

3.3.2 Derivation of Control to Output Transfer Function…… 39

3.4 Signal Injection Technique……. 41

3.5 Conclusion……. 44
4 CONTROL OF DUAL ACTIVE BRIDGE CONVERTER……. 45
4.1 Control Architecture of DAB for EV Charging……. 45
4.1.1 Design of Constant Voltage (CV) Controlled loop……. 46
4.1.2 Design of Constant Current (CC) Controlled loop……. 48
4.2 Controller Design…… 50
4.2.1 Approach-1: Considering Settling Time and Overshoot of The System 50
4.2.2 Approach-1: Considering Desired Crossover Frequency of The System 60
4.3 Peak Current Mode Control (PCMC) of DAB Converter…… 68
4.4 Conclusion…… 64
5 EXPERIMENTAL VERIFICATIONS……. 75
5.1 High Level Block Diagram of Design of DAB Converter…… 75
5.2 Experimental Results of Open Loop Configuration……. 77
5.3 Conclusion……. 81
6 CONCLUSION AND FUTURE SCOPE 82
6.1 Conclusion 82
6.2 Future Scope 83
REFERENCES 84

CHAPTER 1
INTRODUCTION

In modern power systems, DC-DC converters play a crucial role since they enable the conversion of DC power from one voltage level to another efficiently. They are applied in numerous various industries, including telecommunications, electric vehicles, portable electronics, and renewable energy integration [1]. DC-DC converters are critical components that enable the use of various energy sources and enhance the reliability and flexibility of power systems.

One of the fundamental uses of DC-DC converters is in the renewable energy area. The photovoltaic panels of solar sources and wind turbines produce DC power, which requires conversion to a different voltage level before it can be fed into the grid or stored in batteries. Also, battery operated EVs depend greatly on DC-DC converters to regulate the voltage levels between the battery pack and other various subsystems in the vehicle, providing effective energy distribution and optimal performance.

DC-DC converters are essential for facilitating fast and effective energy transmission in the context of EV charging infrastructure. By adjusting the voltage levels between the grid interface, energy storage devices, and the EV battery as needed, they enable high-power DC charging. On order to provide precise control over charge profiles, ensure battery protection, shorten charging periods, and increase overall system efficiency, advance charging stations particularly those that allow ultra-fast DC charging incorporate DC-DC converters [2]. As shown in Fig.1. the block diagram representation of EV charging infrastructure and role of DC-DC converters in it is being highlighted.

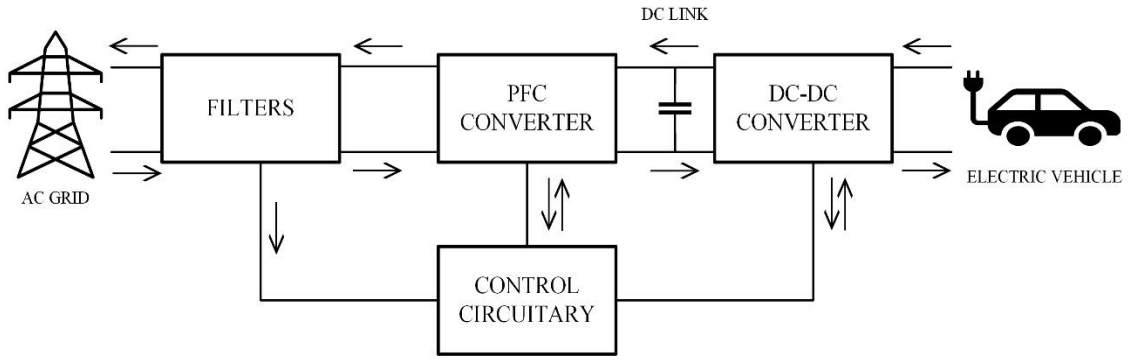

Fig.1.1. Block diagram representation of EV charging infrastructure

The rise in the use of electric vehicles has created increasing demand for efficient, scalable, and reliable charging infrastructure. DC-DC converters are one of the most important enablers in EV charging systems, especially in off-board charging stations where high-power energy transfer is necessary. These converters enable voltage level adaptation between the grid or intermediate energy storage devices and the EV battery, allowing controlled and efficient charging processes. Moreover, DC-DC converters help in the realization of constant current (CC) and constant voltage (CV) charging profiles, which are critical for battery health and rapid charging times [2].

Traditional transformers are being replaced by more adaptable and effective solid-state transformers (SSTs), which are revolutionizing electricity distribution networks. SSTs require DC-DC converters because they enable isolation, voltage control, and bidirectional power flow. Improved fault tolerance, better grid management, and smooth integration of renewable energy sources are all anticipated with the use of SSTs [2].

Innovation in the electricity industry is being propelled by the cooperation of solid-state transformers, microgrids, and DC-DC converters. Microgrids may function independently and smoothly incorporate renewable energy sources thanks to DC-DC converters, which provide effective energy conversion and administration. Furthermore, solid-state transformers' performance and dependability are improved by the incorporation of DC-DC converters, opening the door for a more robust and sustainable energy infrastructure.

1.1 Literature Review

1.1.1 Isolated Bidirectional DC-DC Converter (IBDC) Topologies

An important turning point in the history of DC-DC converters was the invention of semiconductor switches in the 1950s, which set the stage for improved performance and efficiency. With the commercialization of power semiconductor devices and the corresponding advancements in manufacturing technology, this trend intensified in the 1960s. Intense study into converter topologies, such the boost converter, where high efficiency, compactness, and low weight were crucial design factors, was prompted by early uses in the telecommunications and aircraft industries [2].

With the widespread use of power field-effect transistors (FETs) in the late 1980s, significant improvements in converter efficiency were achieved. FETs provided better high frequency switching performance than their bipolar junction transistor (BJT) counterparts, which led to lower switching losses, better thermal management, and less complicated gate driving needs [3].

Table 1.1. Classification of DC-DC converters

Sr. no.	DC-DC converter type	Features
1	Non-Isolated	• Simple structure, lower weight and cost. • Low and medium power level. • Electrically connected input and output.
2	Isolated	• High power levels. • Easy implementation of multi output topologies. • Meets most utility grid standards. • Noise and EMI problems reduced.
3	Unidirectional	• Power flow is only in one direction. • Simple control. • Lower cost and complexity.
4	Bidirectional	• Power flow in both directions. • Complex driver and control

Isolated bidirectional DC-DC (IBDC) converters have become a crucial technology among the different converter topologies used, especially in vehicle-to-grid (V2G) enabled interfaces, on-board auxiliary systems, and off-board charging stations. These converters provide bidirectional energy flow, which is essential for both charging and discharging operations in contemporary EV systems, while also providing galvanic isolation between the input and output, guaranteeing safety and electromagnetic compatibility [4]

IBDCs act as the interface between the external DC connection or energy source and the high-voltage battery pack in EV charging applications. In intricate scenarios like vehicle-to-home (V2H) and vehicle-to-grid (V2G), where energy stored in the car battery is either used to provide local loads or returned to the grid, their capacity to transfer power in both directions is particularly important. Galvanic isolation, which is usually accomplished with a high-frequency transformer, improves system robustness and operational safety by preventing electrical faults or disturbances on one side of the

converter from spreading to the other. Additionally, IBDCs make it easier to adjust the voltage level and precisely control the output voltage and current, which makes it possible to implement charging profiles like constant voltage (CV) and constant current (CC)[5][8].

To meet the requirements of EV charging systems for efficiency, power density, and control accuracy, several IBDC topologies have been created. The Dual Active Bridge (DAB) converter, one of the most widely recognized topologies, is made up of two active full-bridge circuits coupled by a high-frequency isolation transformer. Medium to high-power charging applications can benefit from the DAB topology's ability to facilitate soft-switching via phase shift modulation and high-efficiency bidirectional energy transfer. The CLLC resonant converter as shown in Fig,1.2. is another well studied design that uses a network of resonant tanks to do soft switching under various load circumstances. Applications needing high efficiency, minimal electromagnetic interference (EMI), and a broad output voltage range will benefit most from the CLLC topology [5].

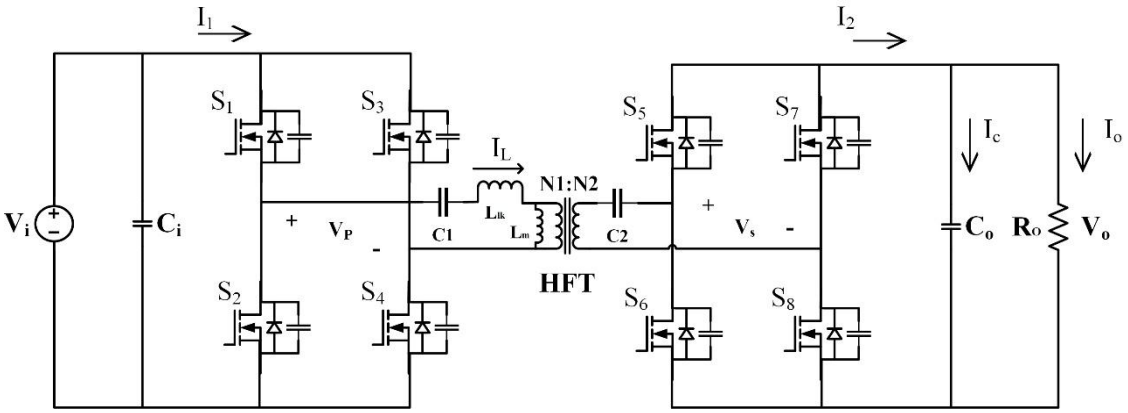

Fig.1.2. CLLC Resonant Converter Circuit Diagram

By incorporating the features of both series and parallel resonant circuits, alternative configurations—like series–parallel resonant converters—offer more flexibility and facilitate better regulation and soft-switching behaviour under a range of operating conditions. Push-pull and flyback-based IBDC topologies are occasionally employed for lower power applications because of their simpler circuit topology and fewer components. Two switches alternately activate the centre-tapped primary winding of push-pull converters inn contrast, flyback converters store energy in the transformer while it is turned on and release it to the output when it is turned off. With the right switching sequences and additional control circuitry, these topologies can be adjusted for

bidirectional operation. However, in comparison to full-bridge or resonant-based systems, these topologies typically offer limited scalability and lower efficiency.

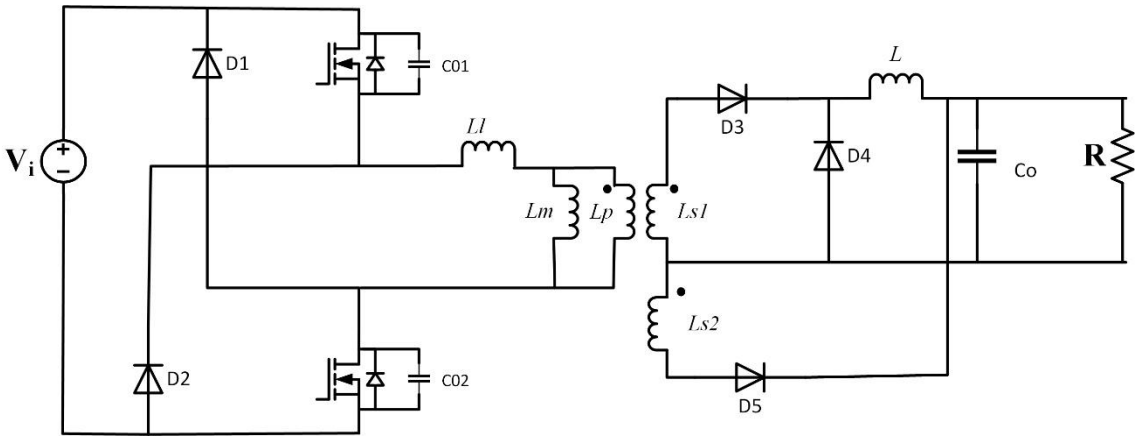

Fig.1.3. Dual Flyback Converter Circuit Diagram

The performance and feasibility of IBDC converters in EV charging systems are determined by several design aspects in addition to topology choices. The main prerequisite for minimizing power losses, lowering thermal stress, and enhancing the charging infrastructure's overall energy use is high efficiency. High-frequency operation and magnetic component optimization are frequently used to provide high power density, which is particularly significant for small and modular charger designs. Reducing switching losses and enhancing electromagnetic compatibility require the ability to function under soft-switching situations. The converter's dependability in commercial EV charging systems is further guaranteed by adherence to isolation and safety standards [6].

1.1.2 Dual Active Bridge (DAB) Converter

One of the most well-known and extensively researched isolated bidirectional DC-DC converter topologies is the Dual Active Bridge (DAB) converter, which is especially well-suited for medium-to high-power applications like electric vehicle (EV) charging systems. The structural component of the DAB is a high-frequency transformer that offers galvanic isolation between two full-bridge converters, one on the primary side and one on the secondary; as shown in Fig.1.4. Phase shift modulation (PSM) between the two bridges' gate signals regulates the energy flow in both directions. The direction and amount of power transfer can be efficiently controlled by varying the phase difference between the primary and secondary bridges [13][15][9].

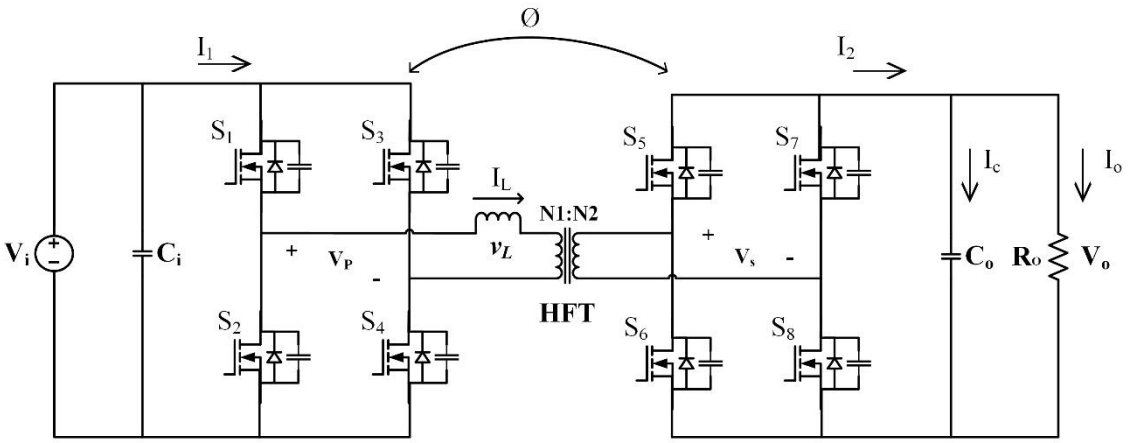

Fig.1.4. Dual Active Bridge (DAB) Converter Circuit Diagram

The DAB converter's ability to achieve zero-voltage switching (ZVS) under a variety of operating settings is one of its main advantages. This significantly reduces switching losses and increases overall efficiency. A key factor in the design for compact EV chargers is power density, which can be increased by using high-frequency operation to reduce transformer size and related magnetic components. Furthermore, the DAB's modular design and symmetric construction make it easy to integrate and scale into multiport converter topologies, which are becoming more and more important in smart charging stations that connect to energy storage systems, batteries, or renewable energy sources [7][8].

The analysis, control, and performance evaluation of a high-power, high-power-density DC-DC converter using the single-phase dual active bridge topology are explored in further detail in [9]. The impact of magnetizing inductance and snubber capacitance on the soft switching area is also examined in this study. The characterization of transmission power, dynamic modelling, soft-switching models, and common uses of the DAB architecture are the main topics of another study [10]. In meanwhile, many modelling approaches and closed-loop control strategies are thoroughly examined in [11]. Furthermore, [12] discusses zero voltage switching boundaries while presenting an average model and a reduced small signal model.

[16] analyses the DAB converter's peak current mode management, highlighting its benefits for boosting system resilience to dynamic load disturbances, decreasing overshoot during mode transitions, and improving transient response. Peak current mode control helps with cycle-by-cycle current restriction, which is essential for safeguarding

battery systems and power devices and allows for quicker correction of current irregularities by monitoring the instantaneous current in the high-frequency transformer. The complexity of the present literature on peak current optimization in DC-DC converters is evident in some of the methods that call for changes to the current topologies, which raises the number of devices. An approach is suggested in this thesis to deal with this difficulty. A hybrid control scheme is proposed, wherein CC and CV control are integrated with current mode feedback to ensure both accurate regulation and enhanced fault tolerance for a developed mathematical model of DAB converter designed to cope with a broad range of input, output, and power voltages. By minimizing peak current on switches and magnetics, this method seeks to increase converter efficiency and lower its overall cost [24][29].

1.2 Research Gaps and Objectives of Dissertation:

In Dual Active Bridge (DAB) converters, the increased peak current passing through the switching devices and magnetic components causes large power losses and places strict component rating requirements on the components. The rise in current exacerbates core and copper losses in magnetic components like transformers and inductors, as well as conduction losses in semiconductor devices. As a result, choosing components that can endure these greater pressures raises the cost of the converter since reliable performance requires improved thermal management techniques in addition to the use of robust and highly rated devices. While extensive literature exists on the general operation of DAB converters, there remains a pressing need for detailed small-signal and behavioural mathematical modelling that accurately captures the dynamics of the converter under various load conditions. Following are the objectives of this dissertation:

- To develop a comprehensive and control-oriented model of the Dual Active Bridge (DAB) converter, suitable for analytical analysis and controller design.
- To design and implement a robust control strategy that supports: Constant Current (CC) mode during the bulk charging phase of EV batteries. Constant Voltage (CV) mode during the saturation phase of EV charging. Peak Current Mode Control (PCMC) for enhancing transient performance and ensuring cycle-by-cycle current protection.

- To ensure system stability, fast dynamic response, and minimal overshoot.
- To explore the practical feasibility of implementing PCMC in DAB converters and investigate its interaction with existing CV and CC control loops—an area that remains underexplored in current literature.
- To validate the performance of the proposed control strategy using: MATLAB/Simulink and PLECS simul**ations** for dynamic analysis and tuning. Hardware experiments with a digital controller (UCD3138A) for real-time implementation and testing under open-loop and closed-loop conditions.
- To contribute to the development of a reliable, efficient, and scalable control framework for isolated bidirectional DC-DC converters used in off-board EV charging infrastructure.

1.3 Dissertation Overview:

The Dissertation includes several chapters, each having a prominent purpose within the research framework. **Chapter 1** serves as a introductory segment, including essential elements such as, Introduction, Literature Review, Research gap and Objectives of thesis. The Dual Active Bridge (DAB) converter is thoroughly examined in **Chapter 2**, which also covers its requirement, working principles, design considerations, and simulation findings related to the traditional single-phase shift control method, along with the other Phase Shift Modulation (PSM) techniques such as Extended Phase Shift (EPS), Dual Phase Shift (DPS) and Triple Phase Shift (TPS).

Chapter 3 comprises of Analysis and Modelling part of the converter. Which includes comparison of various mathematical modelling methods for a power electronic converter based upon their small signal and large signal accuracy, along with the defined sets of equation based upon the desired system parameters, for determining the transfer functions of the system for different operating modes. **Chapter 4** focuses on Controller Design part, where the PI controller parameter calculations for voltage and current loop ia done, and implementation of Peak Current Mode Control (PCMC) mode of operation and its advantages are discussed. Along with-it **Chapter 5** focuses on simulation and hardware results for a digital controller device UCD3138A providing empirical evidence of its performance and effectiveness in practical applications.

CHAPTER 2
DUAL ACTIVE BRIDGE DC-DC CONVERTER

The Dual Active Bridge (DAB) converter as shown in Fig.2.1 is particularly well suited for applications such as EV charging system, Solid State Transformers (SST) and Microgrids, Space Applications and Data Centre power converters. The DAB converter is especially well-suited for both on-board and off-board systems in EV charging applications. It enables effective energy transmission from the grid-side DC link to the vehicle battery in off-board fast chargers while guaranteeing electrical isolation and adherence to safety regulations. Furthermore, the DAB's bidirectional functionality enables regulated battery discharge back into the grid or to local loads in vehicle-to-grid (V2G) scenarios. Through proper phase shift and transformer turns ratio control, the design also offers constant current–constant voltage (CC-CV) charging profiles, maintaining compatibility with the dynamic demands of contemporary battery systems.

This chapter explores the operating principle, working mechanism, design considerations, and simulation of the DAB converter under various conditions. Additionally, simulations of bidirectional operation are conducted, for applications such as Vehicle to Vehicle (V2V) and Vehicle to Grid (V2G) EV charging and future grid systems.

2.1 Operating Principle:

The circuit diagram of DAB converter is presented in Fig.2.1 and equivalent of DAB converter is shown in Fig.2.2(a)

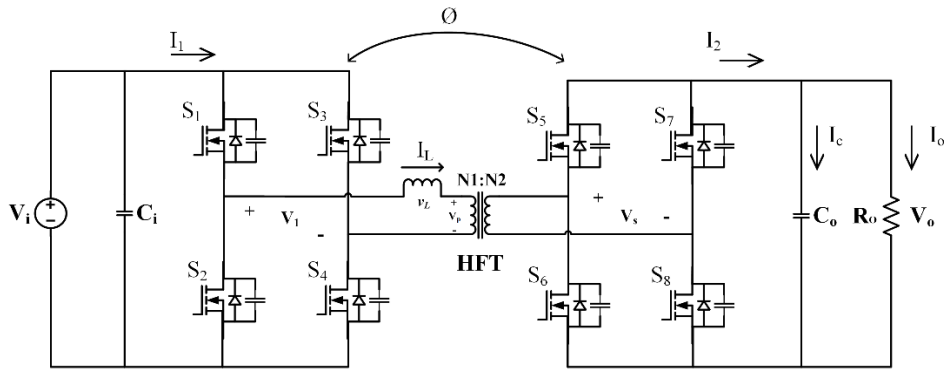

Fig.2.1. Dual Active Bridge (DAB) Converter circuit diagram

Through the utilization of AC power to transfer energy between two sources through a high-frequency transformer, the DAB converter operates as a DC-to-DC converter, Where primary side bridge acts as a inverter (DC-AC), and secondary side bridge acts as a rectifier (AC-DC). In order to modify the direction of power flow, this method entails altering the phase between the sources.

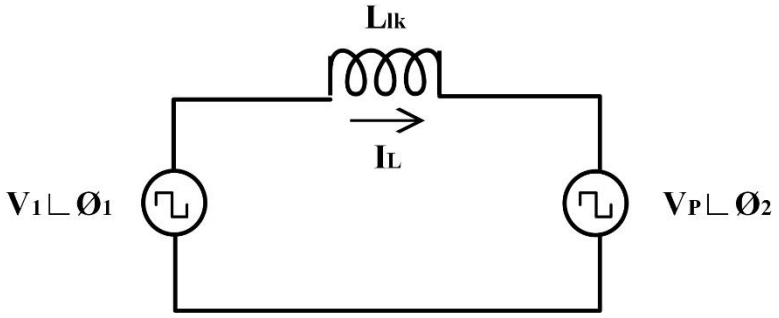

Fig.2.2 (a). Simplified circuit representation of DAB Converter

Initially, the AC power flow between the sources, denoted as V_1 and V_p with respective phases $\emptyset_1$ and $\emptyset_2$ as shown in Fig.2.2(a). The power transferred is determined by the current loop, with $\emptyset_1$ taken as reference.

$$\bar{I_L} = \frac{V_1 \angle \emptyset_1 - V_P \angle \emptyset_2}{j\omega L} \tag{2.1}$$

By representing the current in the time domain with respect to V_1 (where $\emptyset_1=0$), and subsequently averaging the power over one period, a simplified equation is derived.

$$I_L(t) = \frac{V_1}{\omega L}\sin(\omega t) - \frac{V_P}{\omega L}\sin(\omega t - \emptyset_2) \tag{2.2}$$

$$P_0 = V_P(t).I_L(t) \tag{2.3}$$

$$P_0 = \frac{V_1 V_P}{\omega L} sin\emptyset_2 \tag{2.4}$$

Eqn. 2.4. reveals that the phase difference ($Ø_2$) dictates power flow direction; a positive ($Ø_2$) indicates energy transfer from (V_1) to (V_p) while a negative ($Ø_2$) results in reverse power flow. The inductance between the sources facilitates this transfer. Power transmission in the DAB converter works similarly, but the fundamental ideas are the same regardless of whether high-frequency square waves are used in place of the sine waves produced in the primary and secondary full bridges.

In Figs. 2.2(b) and 2.2(c), phasor diagrams for operation of Dual Active Bridge are displayed. Power flows from source V_1 to V_p (forward power flow) in Fig. 2.2(b), where V_1 comes before V_p. Since V_P comes before V_1 in Fig. 2.2(c), power moves in the opposite direction from source V_P to V_1(Reverse power flow).

Where, Ø is the phase shift angle between V_1 and V_p.

θ is the angle between source voltage and inductor current.

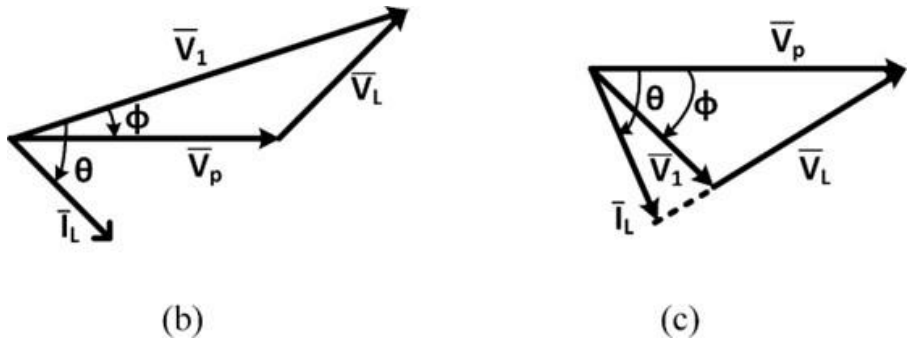

Fig.2.2. Phasor Diagram of (b) Forward power flow (c) Reverse power flow

2.2 Working:

Both the primary and secondary bridges are operated simultaneously in a single-phase, Dual Active Bridge (DAB) converter, with all switches operating at a 50% duty ratio. Each bridge produces square wave outputs as a result of the diagonal switches being coordinated to turn on and off simultaneously. Based on the inductor current waveform and the phase shift between the transformer's primary and secondary voltages, the switching sequence is thoroughly outlined and divided into six intervals. Fig. 2.3 shows these voltage and current waveforms graphically. S_1~ S_4 and S_5~ S_8 stand for primary and secondary side switches, respectively, and are accompanied by capacitors S_{C1} ~ S_{C4} and S_{C5} ~ S_{C8}, as well as diodes S_{D1} ~ S_{D4} and S_{D5} ~ S_{D8}.

The inductor current waveform shows both positive and negative phases at intervals I and II. In interval I, current flows through the primary diodes S_{D1} and S_{D4} and the secondary diodes S_{D6} and S_{D8}, whereas in interval II, current flows through the primary switches S_1 and S_4 and the secondary switches S_6 and S_7. The voltage across the primary (V_1) is equal to V_{dc} throughout the I and II intervals, whilst the voltage across the other

source (V_P) is equal to -V_0. Eqn. 2.5 approximates the present slope throughout this interval.

$$\frac{di_L}{dt} = \frac{V_1 + V_P}{L} \tag{2.5}$$

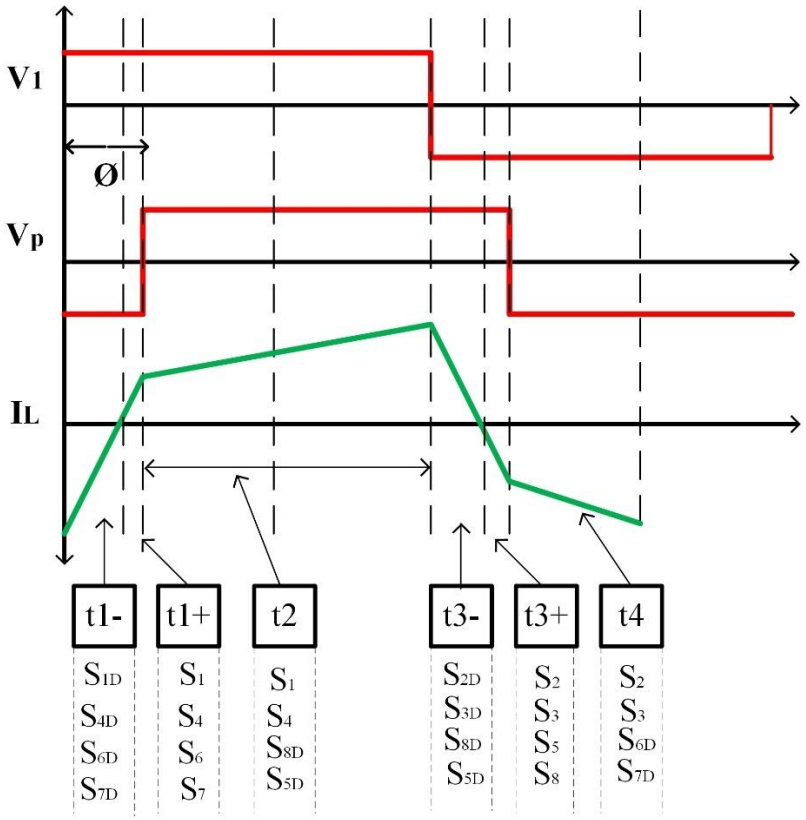

Fig.2.3. Switching configuration during different modes of DAB

The inductor current remains to flow in a positive direction all throughout Interval III. Both the voltage across the secondary side of inductor (secondary side voltage referred to primary) and the voltage at the inductor's input are positive, or V_o and V_{dc}, respectively. According to Eqn. 2.6, the difference between these voltages is therefore reflected across the leakage inductor and affects the rising current slope.

$$\frac{di_L}{dt} = \frac{V_1 - V_P}{L} \tag{2.6}$$

Because of the positive voltage between the secondary and the positive inductor current, diodes S_{D5} and S_{D8} function to promote current conduction during this period, even though switches S1 and S4 stay activated.

As seen in Fig. 2.3, the inductor current changes from its positive peak to zero during interval IV and from zero to a negative value during interval V. The voltage across the secondary stays at Vo during this time, whereas the voltage before the inductor is $-V_{dc}$. As shown in Eqn. 2.7, the difference between these voltages ($-V_{dc}$-V_o) consequently appears across the inductor, causing the current to decrease with a negative slope.

$$\frac{di_L}{dt} = -\frac{V_1 + V_P}{L} \tag{2.7}$$

Diodes S_{D5} and S_{D8}, as well as S_{D2} and S_{D3}, continue to be active during this IV interval. However, switches S_2 and S_3 & S_5 and S_8 are turned on to promote current conduction in interval V since the voltage before the inductor is now at $-V_{dc}$.

The inductor current remains negative during interval VI. During this time, the voltage across the secondary is $-V_o$, and the voltage before the inductor is $-V_{dc}$. As shown in Eqn. 2.8, this causes a voltage difference of ($-V_{dc}$+V_o) across the inductor, which lowers current with a negative slope. Since the voltage across the secondary is now $-V_o$, diodes S_{D6} & S_{D7} are enabled to promote current conduction while switches S_2 & S_3 stay activated at this time.

$$\frac{di_L}{dt} = -\frac{V_1 - V_P}{L} \tag{2.8}$$

2.3 Control Techniques of Dual Active Bridge (DAB) Converter

A variety of phase shift control strategies are developed which are crucial for the effective operation of dual active bridge (DAB) DC-DC converters, including Single Phase Shift (SPS), Extended Phase Shift (EPS), Dual Phase Shift (DPS), and the more modern and advanced Triple Phase Shift (TPS) control technique. Every method is essential for controlling the power flow and enhancing the converter's functionality. SPS control transfers power by varying the phase shift between the primary and secondary bridges. This idea is expanded upon by EPS control, which adds more degrees of freedom to provide more precise control over the power transfer process while lowering stress. Through the use of two distinct phase shifts, between two bridges and in the cross connected switches in the bridges DPS control improves efficiency by better controlling

the converter's operation. While TPS control takes it further by incorporating three different phase shifts, which makes finer control over performance of the converter.

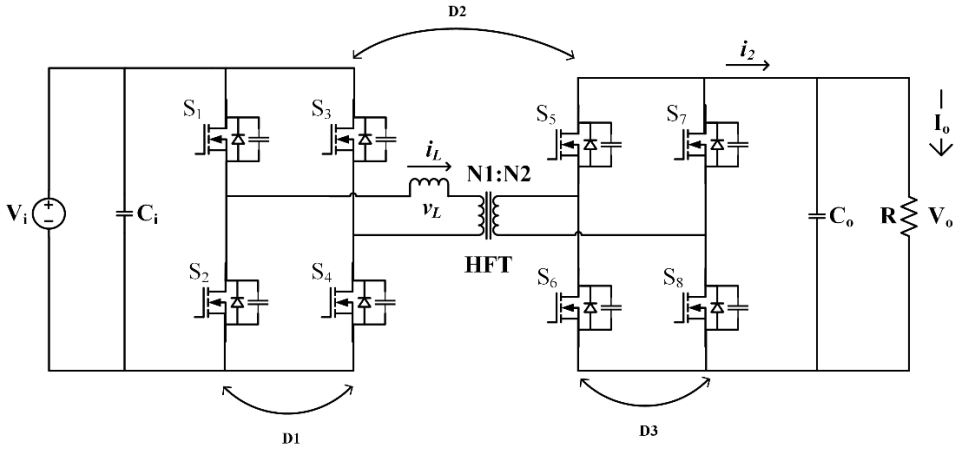

Fig.2.4. Circuit Diagram of DAB Converter with Different Phase Shift Ratios (D)

In Dual Active Bridge (DAB) converters, phase shift modulation is a commonly used control technique that permits effective and bidirectional power transfer. Single Phase Shift (SPS) is the most fundamental and widely applied phase shift control technique. In SPS, both bridges maintain a fixed duty cycle (In this case 50%), and the primary and secondary bridge switching signals' phase difference is the sole mechanism used to regulate power flow. From Fig.2.4 SPS can be explained as the technique where only controlling variable is phase shift between the bridges (D2) while inner phase shifts (D1 and D3) are zero. This method provides adequate performance for a variety of load scenarios, is easy to implement, and requires little computation work. However, because reactive power is present and cannot be independently controlled, SPS, which primarily regulates active power, may show low efficiency under light or fluctuating loads.

More advanced modulation methods like Extended Phase Shift (EPS), Dual Phase Shift (DPS), and Triple Phase Shift (TPS) have been developed to overcome these constraints. By permitting independent control of the duty cycle and phase shift on either side of the transformer, EPS increases flexibility and improves soft switching throughout a wider working range. As from Fig.2.4 in case of EPS the controlling parameters are phase shift between the bridges (D2) and phase shift in the either of the bridges (D1 or D3). By introducing two independent phase shifts, usually one on each bridge leg, DPS improves efficiency under a range of load circumstances by providing better control over both active

and reactive power. From Fig.2.4; DPS introduces additional degree of freedom with inner phase shift ratio where (D1=D3) and phase shift between the bridges (D2) being the controlling parameters. By allowing three degrees of freedom in phase shifting (D1, D2, D3), TPS expands on this idea and greatly improves the converter's controllability and efficiency, especially in applications that need accurate power flow regulation across a broad dynamic range. These advanced methods do, however, come with additional challenges in real-time digital control platforms, having greater computing cost, and more complicated control implementation.

The Single-Phase Shift (SPS) control approach is used in light of the goals of this study, especially the emphasis on modelling and control design for constant voltage (CV), constant current (CC), and peak current mode control (PCMC) in EV charging applications. SPS's simplicity, ease of analysis, and applicability for reduced-order modelling make it popular in both academic research and real-world applications. Furthermore, SPS is a sensible and effective option for the scope of this work because it captures the fundamental dynamics needed for an efficient control design in battery charging scenarios.

Table 2.1. Comparison of Various Phase Shift Control Techniques

Control	Degrees- Freedom	Efficiency	Complexity	Remarks
SPS	1 (D2)	Moderate to good	Low	Widely used, easy to implement
EPS	2 (D1 or D3 and D2)	Moderate to good	Moderate	Better soft-switching range
DPS	2 (D1=D3 and D2)	High	High	Enhanced power control
TPS	3 (D1, D2, D3)	Very High	Very High	Optimal Performance, complex to control

2.4 Soft Switching:

The term "soft switching" describes the use of techniques like Zero Voltage Switching (ZVS) or Zero Current Switching (ZCS) to reduce switching losses in a converter. The achievement of ZVS is especially significant when considering a Dual Active Bridge (DAB) converter. When the voltage across the switch drops to zero before

current flows through it, ZVS occurs. The soft-switching functionality of secondary side switches is explained in this section. It's crucial to keep in mind that the soft switching methodology for primary side switches is analogous to the approach outlined for the secondary side.

2.4.1 Soft Switching Operation

For understanding the operation of soft switching taking place in the DAB converter at particular time instances, let us take an example of defining the soft switching for secondary side switches S_5 and S_8; which are to be turned on while switches S_6 and S_7 are to be turned off.

Step-1: Capacitors across S_5 and S_8 (S_{C5} and S_{C8}) are responsible for blocking the full voltage while voltage across capacitors S_{C6} and S_{C7} is maintained at zero, since these switches are turned on.

Step-2: During the dead time, all switches on the secondary side remain off.

Step-3: Capacitors S_{C5} and S_{C8} discharge to zero, while capacitors SC6 and SC7 charge to their full capacity, as shown in Fig. 2.5.

Step-4: The current maintains its direction, causing diodes S_{D5} and S_{D8} to conduct and clamp the voltage across the switches to zero, as shown in Fig.2.6.

Step-5: Subsequently, switches S_5 and S_8 are turned on. Similarly, switches on the primary side are activated.

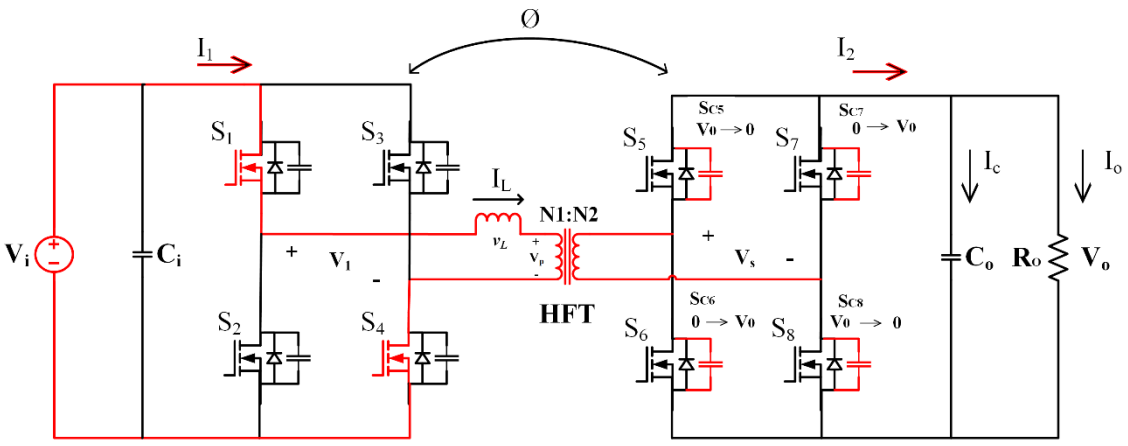

Fig.2.5. Zero Voltage Switching Capacitor charge and Discharge

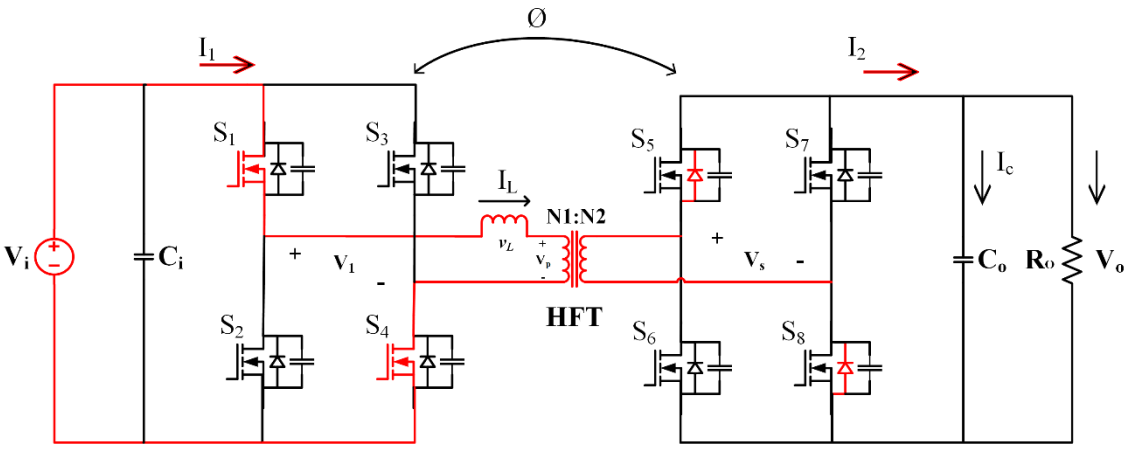

Fig.2.6. Zero Voltage Switching Diode Conduction

2.4.2 Impact of voltage conversion ratio (d) on soft switching of DAB:

An important requirement to realize the soft switching is that prior to any switch starting to conduct, its anti-parallel diode must be conducting. i_1 & i_2 are inductor instantaneous currents (Fig.2.7)

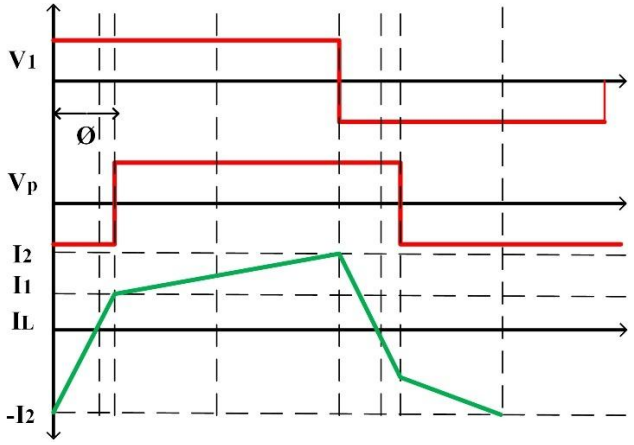

Fig.2.7. Instantaneous Inductor Current in DAB

All the lagging bridge switches and some of the leading bridge switches experience ZVS as a result of the inductive stored energy caused by the natural lagging current in one of the bridges. The ability to charge and discharge the MOSFETs' output capacitances ($Ec = 0.5CV^2$) is dependent on the stored inductive energy ($E_L = 0.5Li^2$), which is also influenced by the converter's load and the input to output voltage ratio. Hence the selection of inductor defines the maximum current stress in the switch node of the converter.

The currents at points i_1 and i_2 can be derived from the waveform as shown in Fig.2.7.

To ensure soft switching across primary bridge,

$$-i_2 \leq 0 \tag{2.9}$$

And for switches in the secondary bridge to be soft switched,

$$i_1 \geq 0 \tag{2.10}$$

$-i_2 \leq 0$ implies that S_{D1} and S_{D4} are conducting.

$i_1 \geq 0$ implies S_{D5} and S_{D8} are conducting.

From Fig.2.7. these instantaneous currents can be defined as,

$$i_1 = \frac{V_1}{2\omega L}(2\emptyset + (d-1)\pi) \tag{2.11}$$

$$i_2 = \frac{V_1}{2\omega L}(2d\emptyset + (1-d)\pi) \tag{2.12}$$

Where,

$$d = \frac{nV_0}{V_i} \tag{2.13}$$

From Eqn.2.11 and 2.12,

$$(2\emptyset + (d-1)\pi) \geq 0 \tag{2.14}$$

$$i_2 = \frac{V_1}{2\omega L}(2d\emptyset + (1-d)\pi) \geq 0 \tag{2.15}$$

Which leads to;

$$\emptyset \geq (1-d)\frac{\pi}{2} \tag{2.16}$$

$$\emptyset \geq \left(1 - \frac{1}{d}\right)\frac{\pi}{2} \tag{2.17}$$

It can be concluded from above equations that to achieve soft switching across the entire range of phase shift ($\emptyset$) in both primary and secondary side switches, the necessary condition can be given by Eqn.2.18

$$d = \frac{nV_0}{V_i} = 1 \tag{2.18}$$

In order to guarantee gentle switching throughout the whole phase shift range, the output voltage must match the input voltage when the High-Frequency Transformer's (HFT) turns ratio is N1:N2 = 1:1.

2.5 Design Considerations:

Based upon the desired power rating and application of the DAB converter, the selection of elements for design is carried out. The main parameters for the DAB converter are High frequency Transformer (HFT), Inductor, Switch selection, and output capacitor.

- **High Frequency Transformer (HFT):**

  Ferrite cores are preferred for developing a High-Frequency Transformer (HFT) because of their low electrical conductivity and high magnetic permeability. A number of variables, including operating power (VA), operating switching frequency (f), flux density (B_m), and wire current density (J), influence the choice of core. Calculations are made for factors such as product area (A_p), core area (A_c), and window area (A_w) in order to identify the proper core.

$$A_P = A_C * A_W = \frac{VA}{2fB_mJk_w} = 1 \tag{2.19}$$

  Number of turns required are calculated by,

$$N = N_P = N_s = \frac{V}{4fB_mA_C} \tag{2.20}$$

  Litz wires are used for transformer winding because of their reduced skin effect, particularly experienced at higher frequencies.

- **Inductor selection:**

  The selection of the inductor is the most important design parameter. The dual-active bridge converter's power transfer relationship is shown in Eqn. 2.21.

$$L = \frac{nV_iV_0}{8fP_0}\emptyset\left(1 - \frac{\emptyset}{\pi}\right) \tag{2.21}$$

  The value of inductor required can be calculated by;

$$L = \frac{nV_iV_0}{8fP_0} \tag{2.22}$$

Eqn. 2.25 makes it clear that improved power transfer capability is the outcome of a decreased inductance value. When the phase shift (ϕ) equals $\pi/2$, the most power transfer is achieved for a given switching frequency, inductor, input voltage, and output voltage.

The connection between the necessary inductor, output power, and phase shift is shown in Fig. 2.8. Higher power needs clearly require a higher inductor value, which in turn calls for a higher phase shift in order to be effectively controlled. Lower inductor values, on the other hand, can transfer the same amount of power but necessitate more precise control over the phase shift.

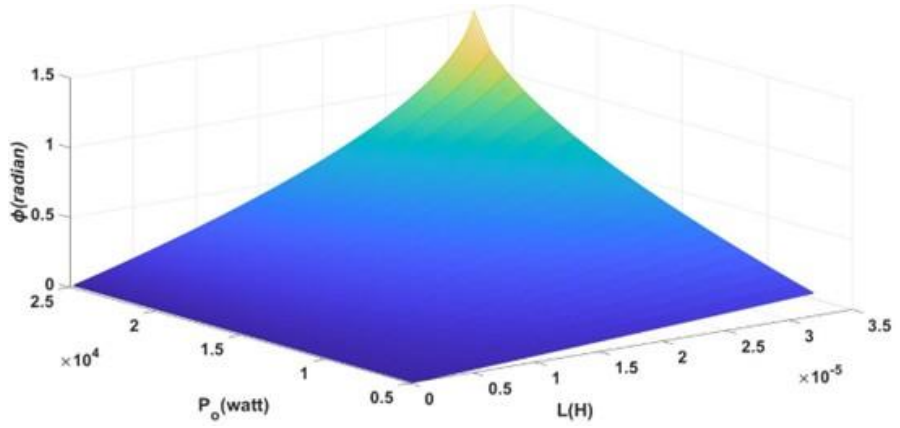

Fig.2.8. Inductance (L) vs Output Power (P_0) vs Phase shift (Ø)

- **Switching Frequency:**

An important factor in improving power density is the switching frequency. By decreasing the size of the magnetics, a higher switching frequency increases the power density. But it comes with a cost in terms of efficiency. In example, switching losses increase with increasing MOSFET output capacitance, especially at low loads, which adversely affects efficiency. As a result, size and efficiency trade-offs must be carefully considered when optimizing switching frequency.

- **Phase Shift:**

The equation defining the phase shift between the primary and secondary side bridges necessary to transfer the required power is given by;

$$P_0 = \frac{nV_iV_0\emptyset(\pi - \emptyset)}{2\pi^2 fL} \tag{2.23}$$

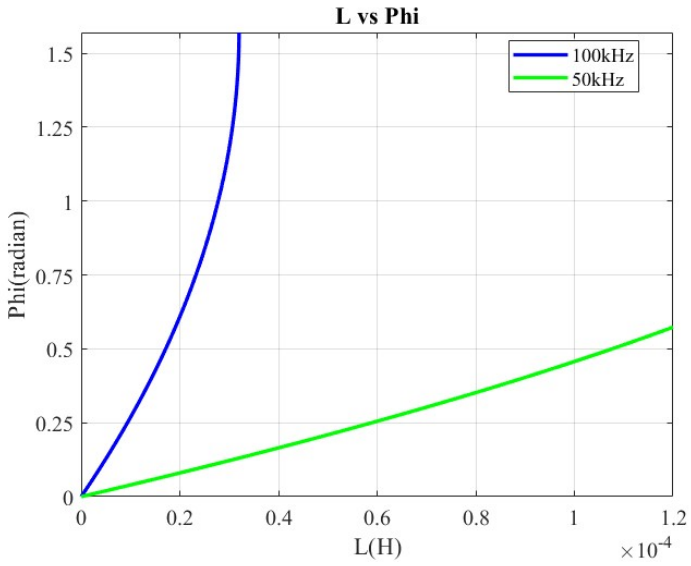

Fig.2.9. Inductance (L) vs Phase shift (Ø)

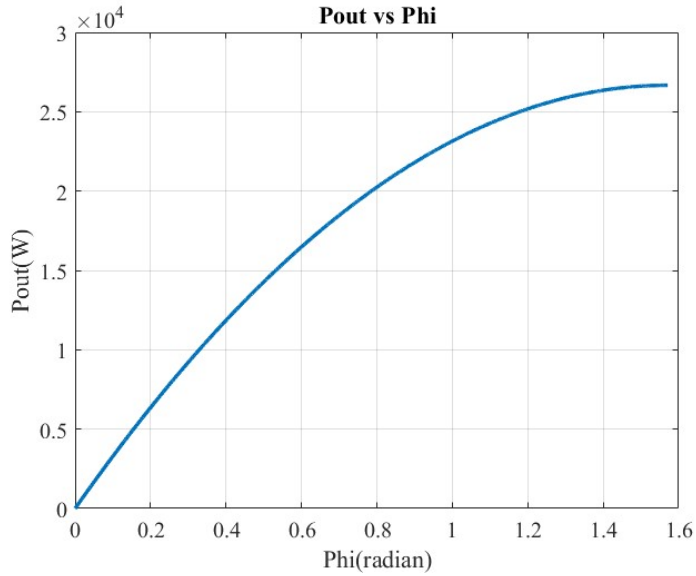

Fig.2.10. Output Power (P_0) vs Phase shift (Ø) at switching frequency of 100kHz

- **Output Capacitor:**

  Output capacitor value is calculated from the Eqn. 2.24

$$C_0 = \frac{\Delta Q}{\Delta V_0} \tag{2.24}$$

$$\Delta Q = \frac{V_i D^2}{4f^2 Ln}\left[(1-D) + \frac{D^2}{4}\right] \tag{2.25}$$

$$D = \frac{\emptyset}{\pi} \tag{2.26}$$

Where, ΔV_0 is peak to peak ripple.

2.6 Simulation Results:

The Traditional Single Phase Shift Control method was used in a MATLAB simulation with the parameters listed in Table 2.1. This method applies a phase shift between the High-Frequency Transformer's (HFT) primary and secondary side bridges. Simulation is carried out using the silicon carbide MOSFET (AIMCQ120R160M1T) characteristics.

The parameters such as, load voltage and load power etc. were decided as per the current trends in EV fast charging system, and rating of DC-DC converters used for fast charging [11].

Table 2.2. Design Parameters of DAB

Parameter	Notation	Value
Input Voltage	V_i	800 volts
Output Voltage	V_0	600 volts
Typical Power Level	P_{max}	10-25 kW
Target Output Power	P_0	6.6 kW
Inductor	L	80 µH
Switching Frequency	f_s	100kHz
Output capacitor	C_0	1000 µF
Turns ratio	N1:N2	1.33:1

2.6.1 Open loop operation:

From the parameters obtained from Table 2.2 the open loop simulation is performed as shown in Fig.2.11.

The current increases during the first interval as a result of the primary voltage (V_{pri}) being more than the secondary voltage (V_{sec}) which are being applied across the inductor. At all timing instances the voltage across inductor (V_L) can be defined as difference between primary and secondary bridge voltages which is (V_{pri})and (V_{sec}/n) respectively. During interval (t_1^+), secondary voltage starts becoming positive hence indicating a smaller slope then the previous interval (t_1^+), at instance (t_2) both voltages are equal and hence the slope remains constant. Similar approach to analysis can be defined for timing intervals (t_3) and (t_4). The amount and direction of the current over the

subsequent intervals are controlled by the phase shifts of primary and secondar side voltages.

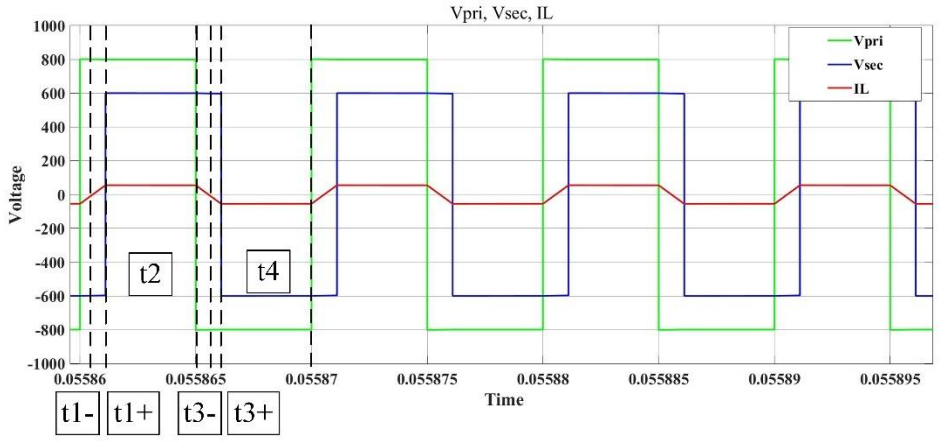

Fig.2.11. Waveforms of Primary Voltage, Secondary Voltage and Inductor Current divided into different time intervals

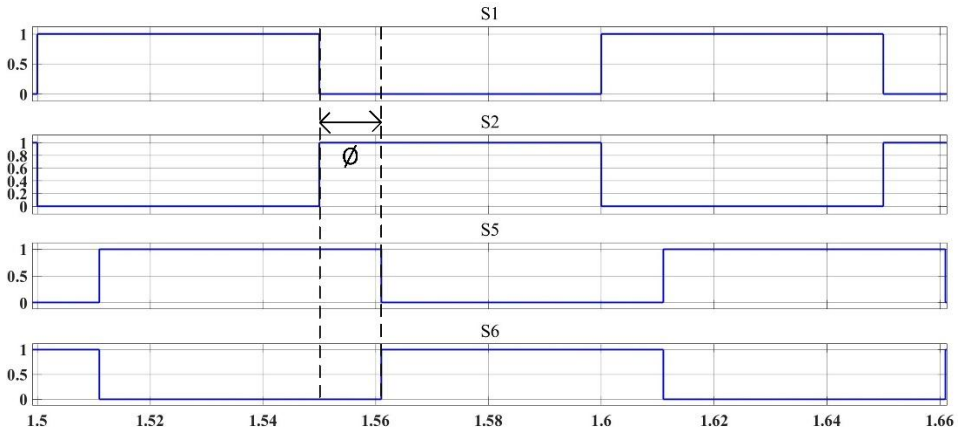

Fig.2.12. Gate Pulses for Primary side and secondary side bridge switches

For calculating the phase shift at a particular value of parameters, to obtain a desired output power level, for a traditional single phase shift approach from Table 2.2

$$P_0 = \left(\frac{N_1}{N_2}\right)\frac{V_i V_0 \emptyset(\pi - \emptyset)}{2\pi^2 f_s L} \tag{2.27}$$

$$P_0 = (1.33)\frac{800 \times 600 \times \emptyset(\pi - \emptyset)}{2\pi^2 100 \times 10^3 \times 80 \times 10^{-6}} \tag{2.28}$$

$$\emptyset = 0.6632rad\ (38°\ approx) \tag{2.29}$$

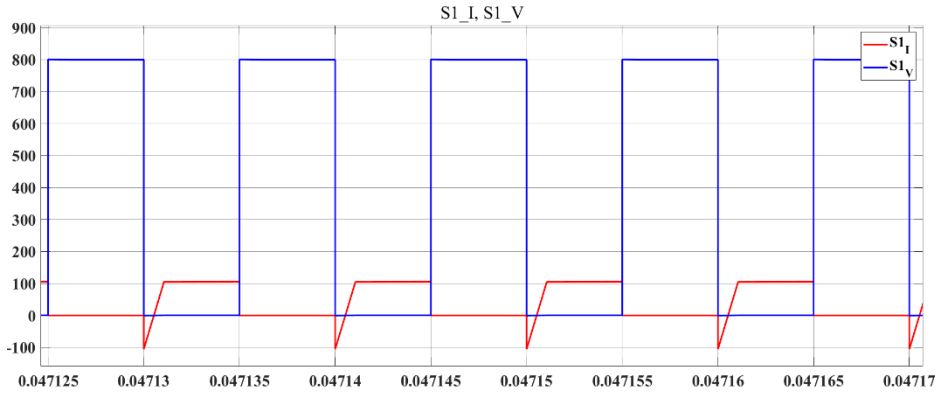

Fig.2.13. Soft Switching of Primary side switch (S_1)

It should be noted that, for better visualisation the current flowing from the switches (Fig.2.13) and inductor current (Fig.2.13) has been scaled by an appropriate factor

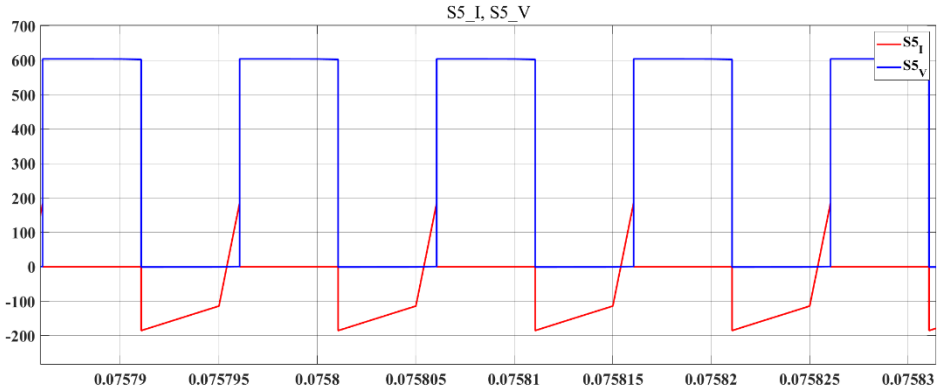

Fig.2.14. Soft Switching of Primary side switch (S_2)

The current flowing from the output of secondary current before the output capacitor (I_2) is nothing but the rectified version of the inductor current, and it can be seen from the simulation results as well (Fig.2.15)

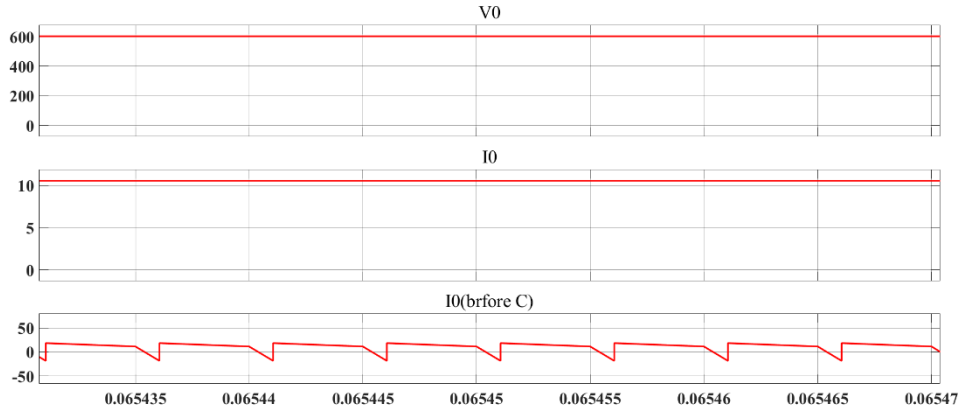

Fig.2.15. Load Voltage, Load Current, and Output Current of secondary side bridge

2.7 Conclusion:

The Dual Active Bridge (DAB) converter's working principle, mechanism, and design challenges are all covered in detail in this chapter, with an emphasis on how well the converter performs in different scenarios. To give a thorough grasp of the converter's behaviour, open-loop simulation has been examined. Extensive simulations have also been carried out to show the DAB converter's bidirectional operation with soft switching, underscoring its potential uses in future grid systems and vehicle-to-vehicle (V2V) and vehicle-to-grid (V2G) electric vehicle charging. The development of effective and adaptable power conversion solutions—which are necessary for contemporary and sustainable electrical infrastructures—is aided by these developments.

CHAPTER 3
MODELLING OF DUAL ACTIVE BRIDGE CONVERTER

For the design and execution of efficient control techniques, particularly in applications with dynamic operating conditions like electric vehicle (EV) charging, accurate modelling of power electronic converters is crucial. This chapter focuses on the modelling of the Dual Active Bridge (DAB) converter. Various modelling approaches are examined, emphasizing their applicability and constraints in relation to control design. In order to describe the essential dynamic behaviour of the DAB converter while preserving computational tractability for controller design, reduced-order modelling is chosen in this work due to the trade-off between model fidelity and analytical simplicity. Transfer functions for the converter in both constant voltage (CV) and constant current (CC) modes of operation are then derived in this chapter. These functions form the basis for the control architecture that is developed in later chapters.

3.1 Various Modelling Techniques of DAB converter:

One essential method for representing physical systems and behaviours is mathematical modelling [24]. Creating precise models for Dual Active Bridge (DAB) converters is more difficult than for traditional DC-DC converters, mainly because the inductor current (i_L), one of the important state variables, is simply alternating and has a zero average value, as shown in Fig. 3. This section provides a thorough review of the many modelling techniques used with DAB converters and simulates the evaluation of large-signal and small-signal models to help guide the design of control systems. Although the approaches can easily be expanded to more complex schemes like Dual Phase Shift (DPS) and Triple Phase Shift (TPS) modulation, the discussion focuses on DAB converters operating under Single Phase Shift (SPS) modulation because of the easier control, less complexity and its capability to capture fundamental dynamics of the converter system to design a appropriate control strategy [7].

- **Reduced-Order Modelling**

By ignoring the high-frequency dynamics of the inductor current and simply depicting the averaged current behaviour throughout a switching cycle, the Reduced-Order Model streamlines the DAB converter. The main dynamics between the control variable (the phase shift angle) and the output voltage or current are captured by the first-order model produced by this technique. Its simplicity, analytical tractability, and high correlation with simulation findings under typical operating conditions are its primary strengths. It works particularly well with single-phase shift (SPS) modulation and is accurate enough for the majority of closed-loop controller designs. However, unless appropriately developed, this model might not take into consideration high-frequency phenomena or parasitic effects.

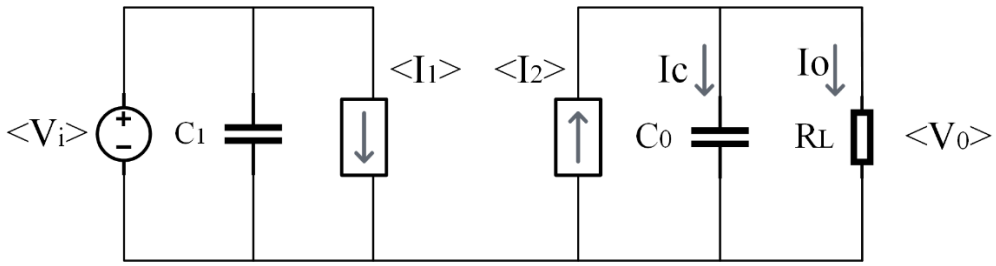

Fig.3.1. Large Signal Diagram of Reduced-order Modelled DAB Converter

As shown in Fig.3.1 The reduced order modelling works on principle of considering the output capacitor as a state variable and deriving a mathematical model based revolving around this state variable. The currents and voltages in the brackets are considered as the switching cycle average value of parameters, which comprises of the DC value and small AC variations within that parameter. Thus, simplifying DAB into a first order system.

After determining the mathematical sets of equation in the steady state model of the system, perturbations are introduced at the input terminal of the system which is a controlling parameter (Phase shift) as per Eqn.3.1 where $Ø_{nom}$ stands for nominal phase shift at steady state and $\Delta Ø$ shows the perturbations (small disturbances with high frequency AC variations)and changes in the output parameter (load voltage, or load current)as per Eqn.3.2 are observed to determine the appropriate transfer function of the system. Where I_2 is the DC value with Δi_2 being the variations in the load parameters

$$\emptyset = \emptyset_{nom} + \Delta\emptyset \tag{3.1}$$

$$< i_2 >_{T_s} = I_2 + \Delta i_2 \tag{3.2}$$

The study presented above indicates that the DAB reduced-order model is a first-order system. Additionally, the circuit model can be expressed for DAB modulated using the DPS and TPS. $G_{i\emptyset}(s)$ is the gain that distinguishes the models of various approaches. Comparing DAB modulated with the DPS or TPS to DAB modulated with the SPS, the computation of this gain is more complicated.

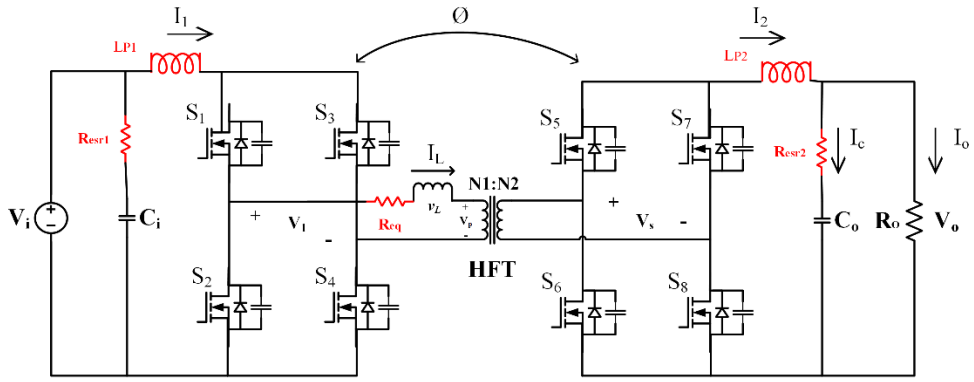

Fig.3.2. Circuit Diagram of DAB Converter Considering Parasitic Elements

With the parasitic parameters (R_{eq}, R_{esr1}, R_{esr2}, L_{P1}, and L_{P2}) shown in red, the reduced-order model may be marginally improved by taking into account the parasitic parameters [29] Because of these little parasites, the resulting model is more complicated. In actuality, though, the standard approach is precise enough for the controller design as mentioned in the later part of this section.

- **Generalized Average Modelling**

The By employing Fourier series expansion to incorporate the inductor current's fundamental frequency component, the Generalized Average Model retains the dynamics of the current. This averaging model is based on the representation of a signal $x(\tau)$ on the interval $\tau \in |t-T, t|$ by Fourier series (Eqn.3.3). Where, $\omega_s = 2\pi f_s$, and the complex number $< x >_k (t)$ is the k[th] coefficient.

$$x(\tau) = \sum_{-\infty}^{\infty} < x >_k (t) e^{jk\omega_s \tau} \tag{3.3}$$

The inductor current i_L is purely AC and as per [] the fundamental component of i_L and DC term of output voltage (V_0) are considered. The state space equation (Eqn. 3.4) and small signal perturbations are employed to derive the small signal model [24], as per Eqn.3.5

$$dx/dt = Ax + BU \tag{3.4}$$

$$y = Cx$$

$$G_{v\emptyset}(s) = C(sI - A)^{-1}B \tag{3.5}$$

This method makes it possible to depict the converter's behaviour more accurately, especially in situations that are rapidly changing. For frequency domain analysis, small-signal transfer functions can be derived using the state-space representation. However, it may be less feasible for real-time control design due to its higher model complexity and vulnerability to steady-state errors, which are brought on by the exclusion of higher-order harmonics.

- **Discrete Time Modelling**

A very precise depiction of the behaviour of the DAB converter is provided by the discrete-time modelling technique, particularly in high-frequency or digitally controlled systems. In contrast to continuous models, discrete-time models take into account that state variables, including output voltage and inductor current, only change at discrete sampling instances. This makes them compatible with digital control platforms. Within a switching cycle, a DAB working with single-phase-shift (SPS) modulation moves between four different switching states. A discrete-time representation in the following form is obtained using the state-space equations corresponding to each state. Then, the state at $t = (k+1)\tau, x[k+1]$ can be expressed using x[k] as,

$$x[k+1] = Fx[k] + GU[k\} \tag{3.6}$$

Where, $x = [i_L, V_0]^T, U = [V_i]$ and the vectors F and G can be calculated based upon the state space equation and period of each state. The dynamics of each interval are captured by the matrices F and G. Then, by adding perturbations to the phase shift and examining how they distribute across phase transition locations, small-signal models can be produced. This method's ability to account for non-idealities including sampling delays, modulation effects, digital control delays, and

Zero Voltage Switching (ZVS) transitions is a significant advantage. However, the discrete-time method's main drawback is its mathematical intricacy. Because there are several switching states in each period, the model necessitates the computation of matrix exponentials, which becomes much more complex. Bilinear Taylor expansion approximations can minimize the computational load, but they are still far more complex than reduced order or average models, and their practical application usually calls for simulation tools like MATLAB.

Upon analysing all the modelling techniques that can be implemented for a DAB converter, as per the reference [24] each modelling technique was implemented and compared by doing simulation analysis, as shown in Fig.3.3,

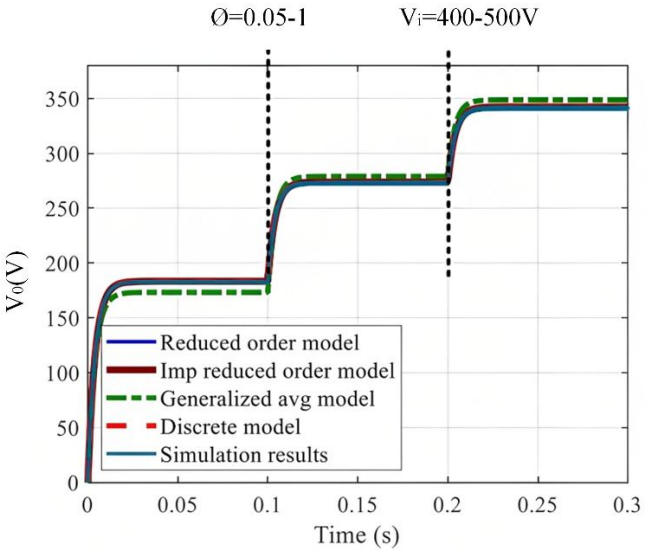

Fig.3.3. Comparison of Large Signal Models

The system was designed with transformer turns ratio of 2:1. With leakage inductance of 70µH and a load resistor of 4Ω. The switching frequency was maintained at 20kHz. An equivalent resistor as seen in Fig.3.2, R_{eq} is utilized to symbolize the power losses brought on by transformers and power equipment. The simulation takes into account a dead time of 200 ns. The large-signal models and simulation results are compared in Fig.3.3. At t = 0.1 s, the input voltage V1 steps from 400 to 500 V, and at t = 0.2 s, the phase shift ratio Ø steps from 0.05 to 0.1. It is to be noted that the generalized average model contains some steady-state errors since the third and higher order components of i_L are disregarded, but all four models predict the V_0 step response rather well.

Table.3.1. Summary of Comparison of Various Modelling Methods for DAB Converter

Modelling Methods	Model Complexity	Accuracy
Reduced Order	Low	High
Generalised Average model	Moderate	Poor
Discrete Time	High	High

The reduced-order model provides the best trade-off between computational simplicity and modelling accuracy among the methods examined, especially for controller design in EV charging applications. Despite its simplifications, the reduced-order model accurately forecasts the dynamic behaviour of the converter under typical operating conditions, according to simulation results in the reviewed literature. Its simplicity makes it easier to perform peak current mode control (PCMC) and derive transfer functions for both constant current (CC) and constant voltage (CV) modes. In order to ensure analytical clarity without sacrificing crucial system dynamics, the reduced-order model has been used as the basis for the creation of the control system.

3.2 Reduced Order Modelling of DAB converter:

In power electronics, reduced-order modelling is a popular technique for streamlining intricate system dynamics while maintaining the fundamental behaviour required for system analysis and control design. Reduced-order models offer an easy method to analyse and regulate the Dual Active Bridge (DAB) converter without using the complete nonlinear or switching models, which are sometimes too complicated for analytical treatment. This modelling technique simplifies the linkages between control inputs, such phase shift, and system outputs, like voltage or current, by utilizing the high switching frequency of the DAB to average out fast dynamics.

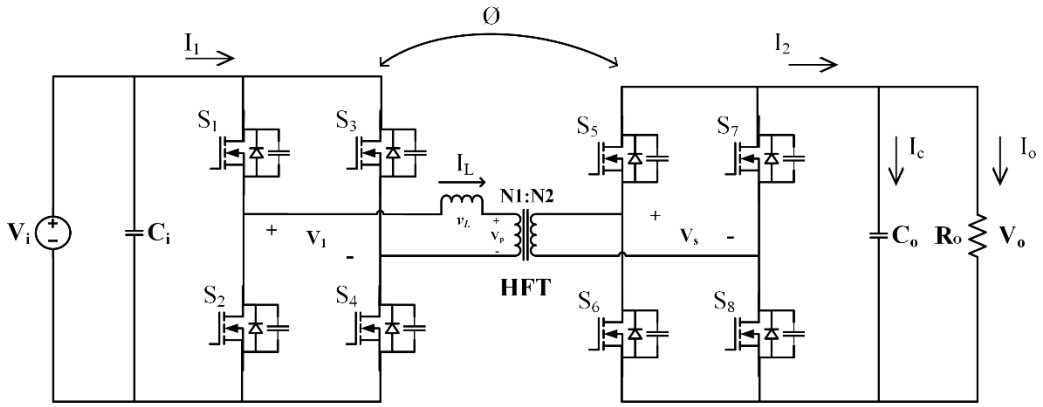

Fig.3.4. Circuit Diagram of Dual Active Bridge Converter

The voltage across inductor V_L can be defined as;

$$V_L = L\frac{di_L}{dt} = V_1 - V_P = V_1 - \frac{V_s}{n} \tag{3.7}$$

Where,

$$n = \frac{N_2}{N_1} \tag{3.8}$$

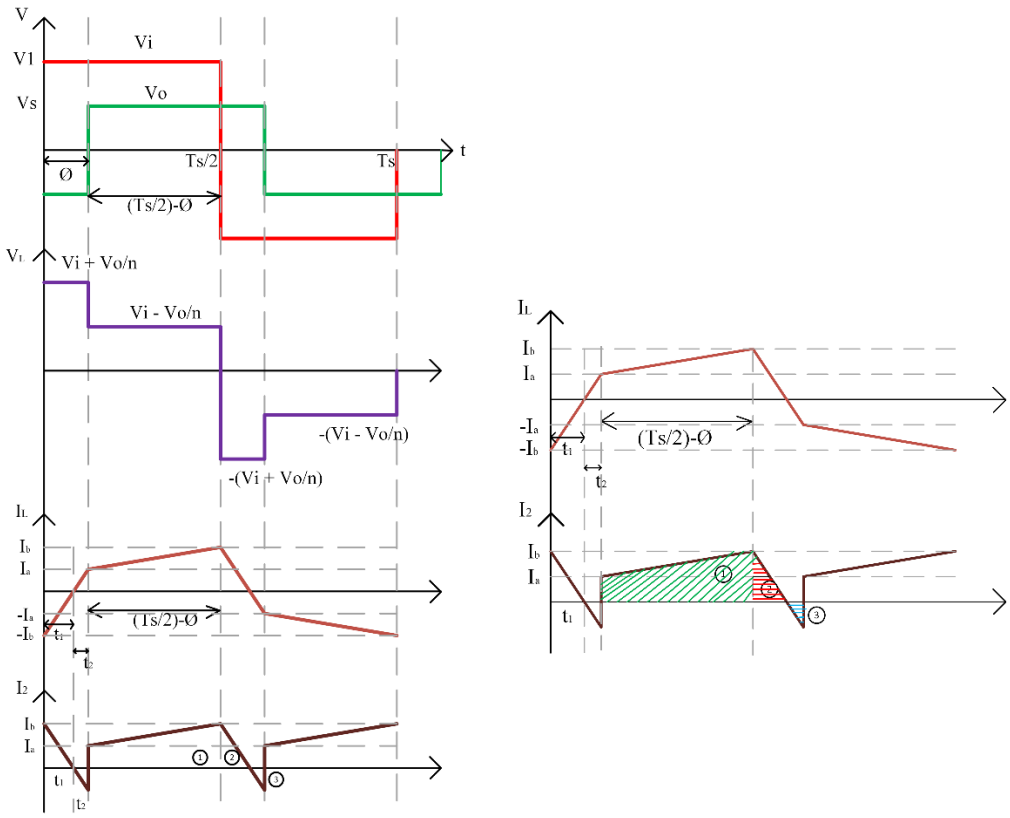

Fig.3.5. Waveforms of DAB Converter under SPS control

From the Fig. 3.5 Where the operation of DAB is shown under SPS control, It can be seen that the inductor current follows a AC nature with four slope changes at every switching cycle, this slope changes follows a pattern where the slopes at instances later of half of the switching cycle (after $T_s/2$) are just negative of the slopes at switching instances t_1 and t_2 following the basic principle of single phase H bridge converter, the output current of secondary bridge (i_2) is rectified version of the inductor current(i_L) and it has been proved in he previous chapter as well (refer section 2.6), The peak of inductor current at each of this instances t_1 and t_2 is labelled as I_a and I_b respectively.

This average ridge output current (i_2) can be defined as;

$$I_{2(avg)} = \frac{Q_{stored}}{n\frac{T_s}{2}} \tag{3.9}$$

The peak currents I_a and I_b from the Fig.3.5 can be defined as;

$$I_b = \left(\frac{V_i + \frac{V_o}{n}}{L}\right) \times t_1 \tag{3.10}$$

$$I_a = \left(\frac{V_i + \frac{V_o}{n}}{L}\right) \times t_2 \tag{3.11}$$

$$\therefore I_a + I_b = \emptyset \times \left(\frac{V_i + \frac{V_o}{n}}{L}\right) \tag{3.12}$$

$$\therefore I_b - I_a = \left(\frac{T_s}{2} - \emptyset\right) \times \left(\frac{V_i + \frac{V_o}{n}}{L}\right) \tag{3.13}$$

Thus, the charge stored in the half switching cycle, is nothing but the area under the $I_{2(avg)}$ curve which is also a rectified inductor current waveform, and that can be calculated as;

As per Fig. 3.5;

$$Q = 1 + 2 - 3 \tag{3.14}$$

$$Q = \frac{1}{2}(I_a + I_b)\left(\frac{T_s}{2} - \emptyset\right) + \frac{1}{2}t_1 I_b - \frac{1}{2}t_2 I_a \tag{3.15}$$

From Eqn.3.9 and Eqn.3.10

$$Q = \frac{1}{2}(I_a + I_b)\left(\frac{T_s}{2} - \emptyset\right) + \frac{1}{2}\left(\frac{V_i + \frac{V_o}{n}}{L}\right) - \frac{1}{2}\left(\frac{V_i + \frac{V_o}{n}}{L}\right) \tag{3.16}$$

Hence from Eqn. 3.12 and 3.13;

$$Q = \frac{1}{2}\emptyset\left(\frac{T_s}{2} - \emptyset\right)\left(\frac{V_i + {V_0}/{n} + V_i - {V_0}/{n}}{L}\right) \tag{3.17}$$

$$Q = \left(\frac{V_i\emptyset\left(\frac{T_s}{2} - \emptyset\right)}{L}\right) \tag{3.18}$$

Thus from Eqn.8 and Eqn.3.18 the average value of output current can be determined as;

$$I_{2(avg)} = \frac{Q}{n\frac{T_s}{2}} = \frac{\left(\frac{V_i\emptyset\left(\frac{T_s}{2} - \emptyset\right)}{L}\right)}{n\frac{T_s}{2}} \tag{3.19}$$

$$= \frac{V_i\emptyset\left(1 - {\emptyset}/{{T_s}/{2}}\right)}{nL}$$

$$= \frac{V_i D\,{T_s}/{2}\,(1 - D)}{nL}$$

$$= \boldsymbol{\frac{V_i D(1 - D)}{2nLf_s}}$$

Where D is defined as phase shift ratio; $D = \frac{\emptyset}{\pi}$

Eqn.3.20 defines the average value of output current which is essential for determining the overall control to output transfer function of the system

Hence, we have;

$$I_{2(avg)} = \frac{V_i D(1 - D)}{2nLf_s}$$

$$I_{2(avg)} = \frac{V_i\emptyset(\pi - \emptyset)}{2n\pi^2 Lf_s} \tag{3.20}$$

Perturb and Linearize;

$$I_{2(avg)} = \boldsymbol{I_2} + \Delta \boldsymbol{i_2} \tag{3.21}$$

$$\emptyset = D_\emptyset + \Delta\emptyset$$

$$V_i = V_{dc} + \Delta v_i$$

Firstly, Perturbing w.r.t V_i

Let,

$$\frac{\emptyset(\pi - \emptyset)}{2n\pi^2 L f_s} = \sigma \tag{3.22}$$

$$\therefore I_{2(avg)} = \sigma\, V_i \tag{3.23}$$

$$\therefore I_2 = \sigma\, V_{dc}$$

$$\& \ (I_2 + \Delta i_2) = \sigma(V_{dc} + \Delta v_i)$$

$$\therefore \Delta i_2 = \sigma \Delta v_i \tag{3.24}$$

Similarly, Perturbing with respect to D,

Let,

$$\frac{V_i}{2n\pi^2 L f_s} = \mu \tag{3.25}$$

$$\therefore I_{2(avg)} = \mu(\emptyset(\pi - \emptyset)) \tag{3.26}$$

$$\therefore I_2 = \mu(D_\emptyset(\pi - D_\emptyset)$$

$$\& \ (I_2 + \Delta i_2) = \mu((D_\emptyset + \Delta\emptyset)(\pi - (D_\emptyset + \Delta\emptyset)))$$

$$= \mu(\pi D_\emptyset - D_\emptyset^2 - D_\emptyset \Delta\emptyset + \Delta\emptyset\pi - D_\emptyset\Delta\emptyset - \Delta\emptyset^2)$$

$$= \mu[D_\emptyset(\pi - D_\emptyset) + \Delta\emptyset(\pi - 2D_\emptyset)]$$

$$\therefore \Delta i_2 = \mu[\Delta\emptyset(\pi - 2D_\emptyset)] \tag{3.27}$$

Considering input voltage to be constant and ripple free (Δv_i=0)

From Eqn. 3.22, Eqn.3.24, Eqn. 3.25, Eqn.3.27

$$\Delta i_2 = \left[\frac{V_i}{2n\pi^2 L f_s}\right] \Delta\emptyset(\pi - 2D_\emptyset) \tag{3.28}$$

$$\frac{\Delta i_2}{\Delta\emptyset} = \left[\frac{V_i}{2n\pi^2 L f_s}\right] (1 - 2D_\emptyset)$$

Hence, the control to output gain ($G_{i\emptyset}$) can be defined as;

$$\boldsymbol{G_{i_2\emptyset}(s) = \frac{V_i(1 - 2D_\emptyset)}{2n\pi^2 L f_s}} \tag{3.29}$$

From the Fig.3.4 It can be seen that,

$$I_2 = I_c + I_o \tag{3.30}$$

The average value of I_2 can be expressed as,

$$I_{2(avg)} = < i_2(t) >_{T_s} = C_o \frac{d < V_o(t) >_{T_s}}{dt} + \frac{1}{R_o} < V_o(t) >_{T_s} \tag{3.31}$$

$$\therefore C_o \frac{d < V_o(t) >_{T_s}}{dt} = < i_2(t) >_{T_s} - \frac{1}{R_o} < V_o(t) >_{T_s} \tag{3.32}$$

From Eqn.3.20, and taking Laplace transform of Eqn.3.32,

$$sC_0 < V_0(s) > = g < V_i(s) > \emptyset(\pi - \emptyset) - \frac{1}{R_0} < V_0(s) > \tag{3.33}$$

Such that,

$$g = \frac{1}{2n\pi^2 L f_s} \tag{3.34}$$

Since we already know the linearized function of average bridge output current (I_2), now the next step is to perturb and linearize the Eqn.3.35 to obtain relation between load voltage and phase shift/phase shift ratio;

$$< V_0 > = \boldsymbol{V_0} + \Delta \boldsymbol{v_0} \tag{3.35}$$

$$\emptyset = D_\emptyset + \Delta\emptyset$$

$$V_i = V_{dc} + \Delta v_i$$

Using perturbation and linearization; from Eqn.3.29

$$sC_0 \Delta v_0(s) = [g V_{dc}(s) \Delta\emptyset(s)](\pi - 2D_\emptyset) - \frac{\Delta v_0(s)}{R_0} \tag{3.36}$$

$$\therefore sC_0 \Delta v_0(s) + \frac{\Delta v_0(s)}{R_0} = [g V_{dc}(s) \Delta\emptyset(s)](\pi - 2D_\emptyset)$$

$$\Delta v_0(s) \left[\frac{1 + sC_0 R_0}{R_0}\right] = [g V_{dc}(s) \Delta\emptyset(s)](\pi - 2D_\emptyset)$$

$$\therefore \frac{\Delta v_0(s)}{\Delta\emptyset(s)} = g V_{dc}(\pi - 2D_\emptyset) \left[\frac{R_0}{1 + sC_0 R_0}\right]$$

$$\therefore \boldsymbol{G_{v\emptyset}(s) = \frac{V_{dc}}{2nLf_s}(\pi - 2D_\emptyset)\left[\frac{R_0}{1 + sC_0 R_0}\right]} \tag{3.37}$$

Hence, the complete control to output transfer function, for phase shift to load voltage and phase shift to load current;

$$G_{v\emptyset}(s) = \frac{(\pi - 2D_{\emptyset})}{2n\pi^2 f_s L C_o}\left(\frac{V_i}{s + \frac{1}{R_o C_o}}\right) \tag{3.38}$$

Similarly, for control to output (phase shift to load current) transfer function can be calculated as;

$$G_{i\emptyset}(s) = \frac{(\pi - 2D_{\emptyset})}{2n\pi^2 f_s L C_o R_0}\left(\frac{V_i}{s + \frac{1}{R_o C_o}}\right) \tag{3.39}$$

3.3 Transfer Function of DAB converter for Constant Voltage (CV) mode and Constant Current (CC) mode:

After establishing the mathematical modelling framework for the Dual Active Bridge (DAB) converter, this section concentrates on obtaining and verifying the transfer functions that are pertinent to constant voltage (CV) and constant current (CC) mode operations. These transfer functions are the foundation of control system design because they describe the dynamic relationship between the control input, usually the phase shift, and the output variables, such as voltage or current, under various operating conditions. In order to obtain precise frequency-domain representations, the signal injection technique is used with PLECS, in which small perturbations are applied to the control input and the corresponding response of the output is observed. This allows for the extraction of empirical transfer functions, which are then examined using Bode plots to evaluate system gain, phase response, etc. In order to guarantee steady and precise performance of the DAB converter under various load conditions, the generated transfer functions are used as the foundation for the following design and tuning of control loops for CC and CV charging profiles.

3.2.1 Charging Characteristics of EV Battery:

The charging properties of the battery itself serve as a major guidance for the design of control techniques for EV battery chargers. Commonly seen in electric vehicles, lithium-ion batteries have a well-defined charging profile that usually consists of two

phases: a constant current (CC) phase and a constant voltage (CV) phase. The charger provides a constant current during the CC phase, and the battery voltage progressively increases. The charging process moves into the CV phase, where the voltage is maintained constant and the current progressively tapers down, as soon as the terminal voltage hits the designated threshold. In order to guarantee battery longevity, safety, and quick charging without overcharging or overheating, these two charging modes—CC and CV—are essential.

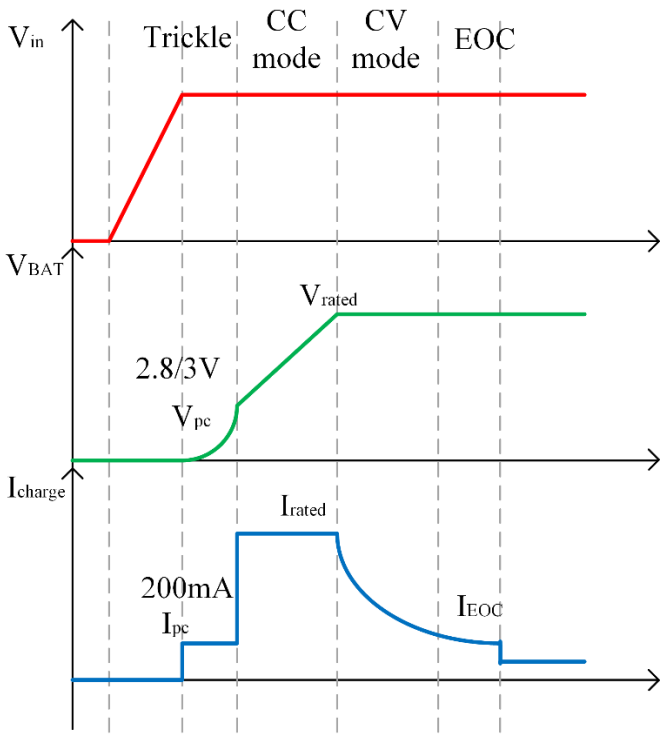

Fig.3.6. Charging Characteristics of Li-ion Battery (EV battery)

As per the charging characteristics of the battery shown in the Fig.3.6 Initially, when charger is powered up by applying the input voltage, the charger measures the cell voltage, if the cell voltage is less than the pre charged threshold voltage, the charger enables the trickle charging in which it charges the battery to approximately 10% of full charging rate (if the charging rate of battery is 2Ah the trickle charging rate is 200mAh). This process helps battery from damage by high surge currents. This trickle charging process continues until the battery reaches its minimum charging voltage threshold (in case of Li-ion batteries it is 2.8 to 3V) if the charger is not able to achieve this voltage, it can be said that the battery is short circuited or damaged.

Once the cell voltage crosses the pre-charging threshold voltage, the charger shifts to 100% full charging rate, where the charger charges the battery with Constant Current (CC) mode. In this case the cell voltage rises until the Constant Voltage threshold limit (70-80%). Then the charger shifts to Constant Voltage (CV mode) finally charger current falls through minimum value, the charger notices the limit and once the charging current reaches the End of Charge (EOC) stage (10% of rated value) the charger stops the charging.

To derive these characteristics of the battery as per the design parameters of the DAB converter the battery was modelled as a resistive load for the initial purposes and boundaries for the analysis and experimental verification were plotted as per Fig.3.7

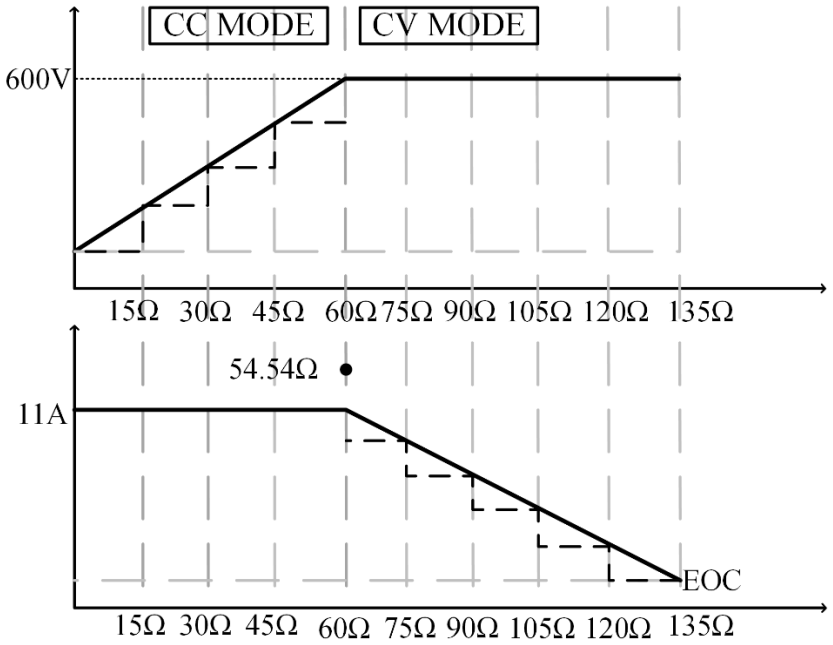

Fig.3.7. CC-CV Mode of Charging as Per Design Parameters

3.2.1 Derivation of Control to Output Transfer Function

The design parameters of the converters used are as per Table.3.1 where the converter is chosen to have a typical power rating of 6.6kW and a maximum power level of 10kW. As per the design calculations explained in chapter 2 (section 2.4). at a maximum phase shift of 90˚(π/2) the maximum power is obtained based upon what the value of leakage inductance of HFT was chosen which approximately comes out to be (80μH), And from where the nominal phase shift was obtained for achieving the target power level.

Table 3.2. Design Parameters of DAB

Parameter	Notation	Value
Input Voltage	V_i	800 volts
Output Voltage	V_0	600 volts
Typical Power Level	P_{max}	10-25 kW
Target Output Power	P_0	6.6 kW
Inductor	L	80 µH
Nominal Phase Shift	$D_{ø}$	38˚ (0.663)
Switching Frequency	f_s	100kHz
Output capacitor	C_0	1000 µF
Turns ratio	N1:N2	1.33:1

Hence, from the modelling of DAB converter with the derivations of control to output transfer functions as per the Eqn.3.38 and Eqn.3.39 and the values of parameters as per the Table 3.2 the transfer functions can be redefined as

$$G_{V\emptyset}(s) = \frac{12309.20}{s + 20.5023} \tag{3.40}$$

$$G_{i\emptyset}(s) = \frac{224.2484}{s + 20.5023} \tag{3.41}$$

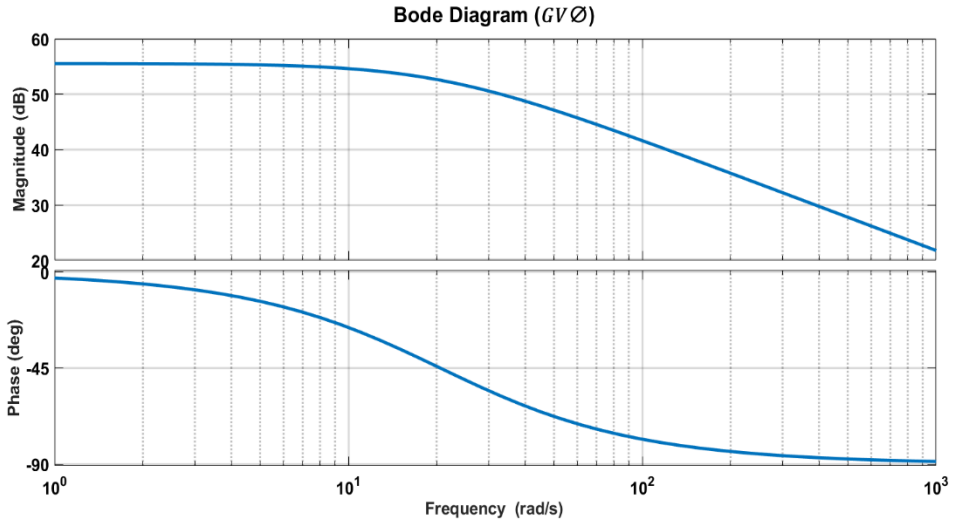

Fig.3.8. Bode Plot of Open Loop Plant Transfer Function ($G_{vø}(s)$)

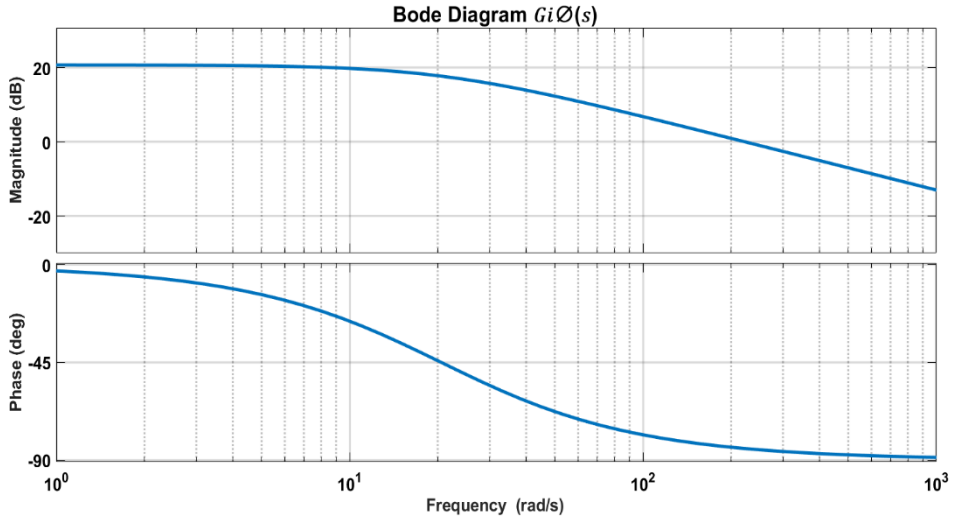

Fig.3.9. Bode Plot of Open Loop Plant Transfer Function ($G_{i\emptyset}(s)$)

As shown in the Fig.3.7 and Fig.3.8 as per the bode plots of open loop transfer functions for load voltage to phase shift and load current to phase shift as per the derived results in the equations Eqn.3.40 and Eqn.3.41 it can be seen that the plant operates in the first order control system where the only pole of the system is determined by the state variable of the converter which in DAB case is the output capacitor.

As Reduced-order modelling suggests, we do not take the dynamics of inductor current into the account because of its purely sinusoidal AC nature with an average value of zero, which can create complexity in modelling the DAB converter.

Since the pole of the system holds a real value and lies on the Left Half Plane (LHP) the converter is stable with phase margin of 90˚.

3.3 Signal Injection Technique:

One prominent frequency-domain methodology for describing the dynamic behaviour of power electronic systems is signal injection technique. Without needing a complete analytical solution of the converter's intricate time-domain equations, it is especially helpful for estimating transfer functions and testing small-signal models. This method involves injecting a small disturbance into the system at a chosen input point, usually a sinusoidal signal with a known frequency and amplitude. The resulting steady-state or transient response is then evaluated at a specified output node. The transfer function of the system can be empirically approximated and displayed as a Bode plot by

sweeping the injection frequency over a specified range and measuring the gain and phase shift at each point. The technique is particularly useful in power converters like the Dual Active Bridge (DAB), where it can be theoretically demanding and prone to idealistic assumptions to derive transfer functions analytically under various control modes (e.g., constant current and constant voltage).

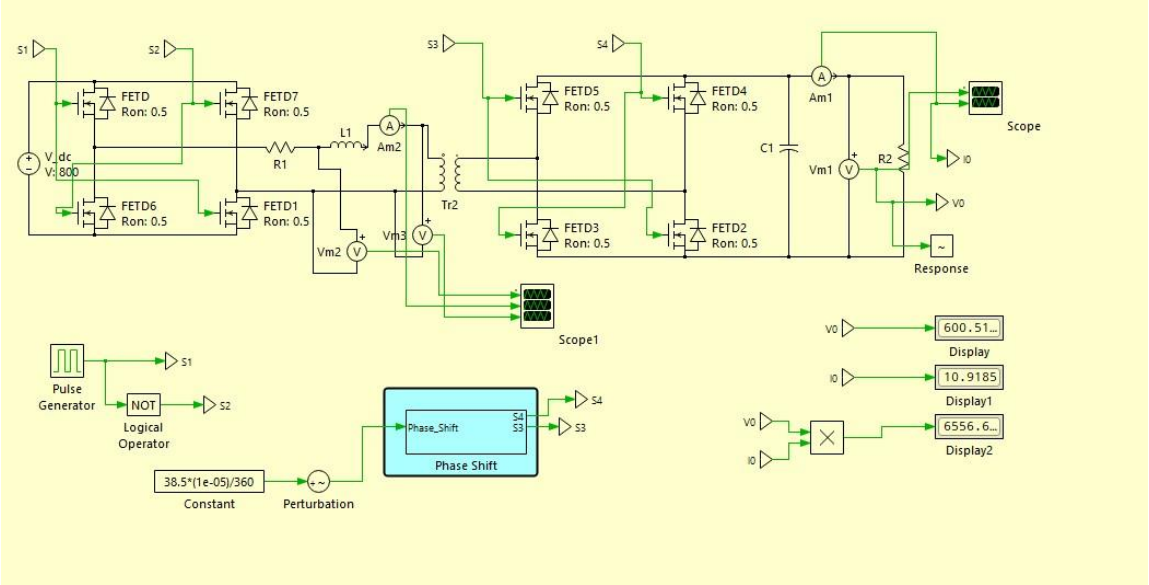

Fig.3.10. Simulation Setup for Signal Injection Technique Using PLECS

As Shown in Fig.3.9 the simulation setup of DAB converter was created in the "PLECS standalone", and parameters were selected as per the design considerations. The Phase shift which is input in our case was perturbed with sinusoidal signals ranging from frequency 20Hz to 50kHz (half of the switching frequency) in logarithmic manner with an amplitude of 10% of the nominal value of the input parameter. These perturbations were added by using "*Impulse response analysis*" tool present in the PLECS Standalone. And the response at the load voltage was observed.

After noticing all the set points of frequency of the injected signals the transfer function was obtained with the help of bode plot, as shown in Fig.3.10. It can be seen from the obtained bode plots the phase plot of both the results follows the exact same trace indicating that the location of poles is in the same place as that of analytical calculations.as per the magnitude plot is considered it can be seen that there is a significant difference in the gain plot obtained from the analytical results and the gain plot obtained from the simulated results.

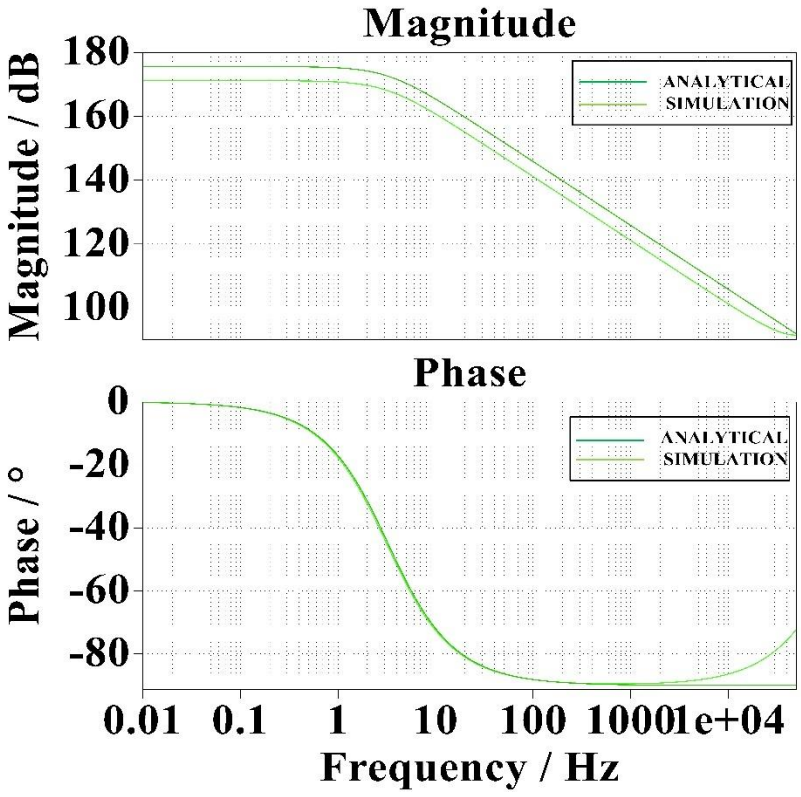

Fig.3.11. Obtained bode plots of Analytical and Simulated results Using PLECS

The difference in the gain obtained from both the scenarios could be due to the parasitic parameters present in the system, and the nature and value of the output capacitor chosen for the analysis. Since for the analytical purposes the magnitude plot has very less gain compared to that of the simulation results, taking out the capacitive element from the DC gain results in similar magnitude plot obtained from the simulation and as shown in the Fig.3.10 as well.

Hence choosing the appropriate value of the parameters and considering the parasitic elements while designing the systems become crucial as long as parameters such as DC gain are considered. But as far as phase plot is considered the Reduced order modelling can be verified and proven to be more accurate and less complex.

3.4 Conclusion

With an emphasis on determining the most efficient method for control-oriented analysis in electric vehicle (EV) charging applications, this chapter provided a thorough examination of the modelling approaches relevant to the Dual Active Bridge (DAB) converter. Discrete-time modelling, generalized average modelling, and reduced-order modelling were all thoroughly compared. The complexity, correctness, viability of execution, and applicability to control design of each approach were assessed. This assessment led to the conclusion that reduced-order modelling was the best approach because of its ease of analysis, enough accuracy, and suitability for use with conventional control design techniques. The small-signal transfer functions necessary for designing and implementing controllers in both constant voltage (CV) and constant current (CC) charging modes could be reliably derived using this method.

The chapter then looked at lithium-ion EV battery charging characteristics, emphasizing the importance of CV and CC modes and how they affect converter behaviour. The reduced-order model was then used to create transfer functions for each mode, which captured the dynamic interaction between the output variables and the control input (phase shift). The PLECS simulation platform was used to implement the signal injection technique in order to validate these analytical results. The analytically produced Bode plots were compared with the frequency response characteristics that were obtained by inserting frequency-domain perturbations into the control signal and examining the system's output response. The correctness of the modelling approach and the appropriateness of reduced-order modelling for controller design in DAB-based EV chargers are confirmed by the strong agreement between the simulated and analytical transfer functions.

CHAPTER 4
CONTROL OF DUAL ACTIVE BRIDGE CONVERTER

Following the development and validation of a suitable mathematical model in the previous chapter, the control technique necessary for the Dual Active Bridge (DAB) converter to operate effectively and steadily in electric vehicle (EV) charging applications is the primary emphasis of this chapter. Implementing the conventional constant current (CC) and constant voltage (CV) charging profiles required by lithium-ion battery systems requires efficient DAB control. The control objectives and design technique for both CV and CC control loops are presented at the beginning of this chapter, along with important factors to take into account when choosing controller parameters. Frequency-domain technologies like Bode plot analysis enhance the design process, which is then executed and validated using MATLAB/Simulink. The dynamic performance of the closed-loop framework in both charging modes is illustrated by the simulation results. Furthermore, a concise synopsis and theoretical understanding of Peak Current Mode Control (PCMC) are provided, emphasizing its potential benefits in enhancing transient response and current limiting in subsequent control framework improvements. In order to achieve a workable and reliable EV charging system with DAB topology, this chapter thus constructs a comprehensive control architecture on the basis of the modelling efforts previously created.

4.1 Control Architecture of DAB for EV charging:

The charging characteristics of lithium-ion batteries used in electric vehicles (EVs) requires both constant current (CC) and constant voltage (CV) modes of operation, as determined in the previous chapter. The Dual Active Bridge (DAB) converter needs to have a control architecture that can separately regulate voltage and current based on the battery's instantaneous state of charge (SOC) in order to accomplish this functionality. The battery functions in CC mode during the first stage of charging, when a controlled current is delivered until the terminal voltage reaches the highest allowable limit. After this, the control mode changes to CV, where the charging current naturally decreases off and the

voltage is maintained at a constant level. Both the CC and CV control loops are implemented in a cascaded architecture in the DAB converter control system to enable this dynamic behaviour.

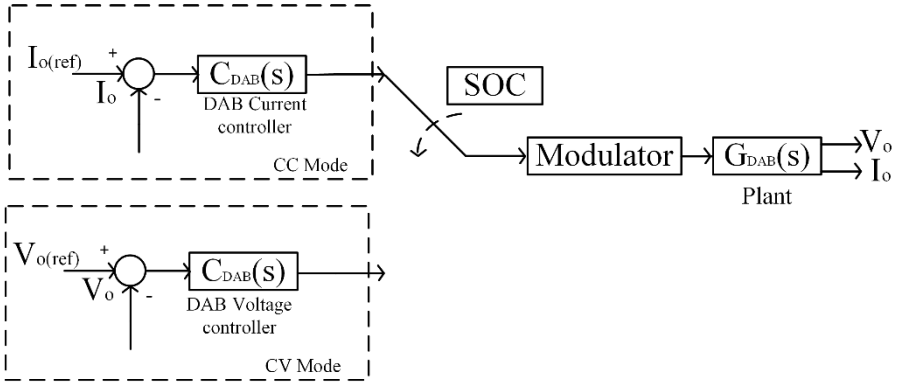

Fig.4.1. Proposed Control Architecture of DAB converter for EV charging

Despite having separate feedback and compensator designs, the CC and CV loops in this arrangement are functionally coordinated to activate in response to the charging state. Real-time battery parameters—specifically, the SOC or output voltage threshold—determine which active loop is used. The DAB converter will smoothly transition to the charging phase thanks to this mode-switching logic, which prevents instability and performance deterioration. The system can retain accurate management during the charging process while guaranteeing battery safety and optimizing performance by implementing this dual-mode control design.

4.1.1 Design of Constant Voltage (CV) Controlled loop

During the final phase of electric vehicle (EV) battery charging, the Dual Active Bridge (DAB) converter's constant voltage (CV) control loop is used to manage the output voltage. To regulate power transfer and preserve the desired output voltage, this control approach modulates the phase shift between the primary and secondary bridges. This method works especially well in off-board EV charging systems, where precise voltage control is necessary to guard against overcharging and guarantee battery safety. Important benefits of voltage mode control include accurate voltage regulation, versatility over a broad variety of output voltages, and increased efficiency via ideal phase shift operation. Additionally, it improves dynamic load handling, which enables the converter to adapt to changes in battery behaviour and charging circumstances.

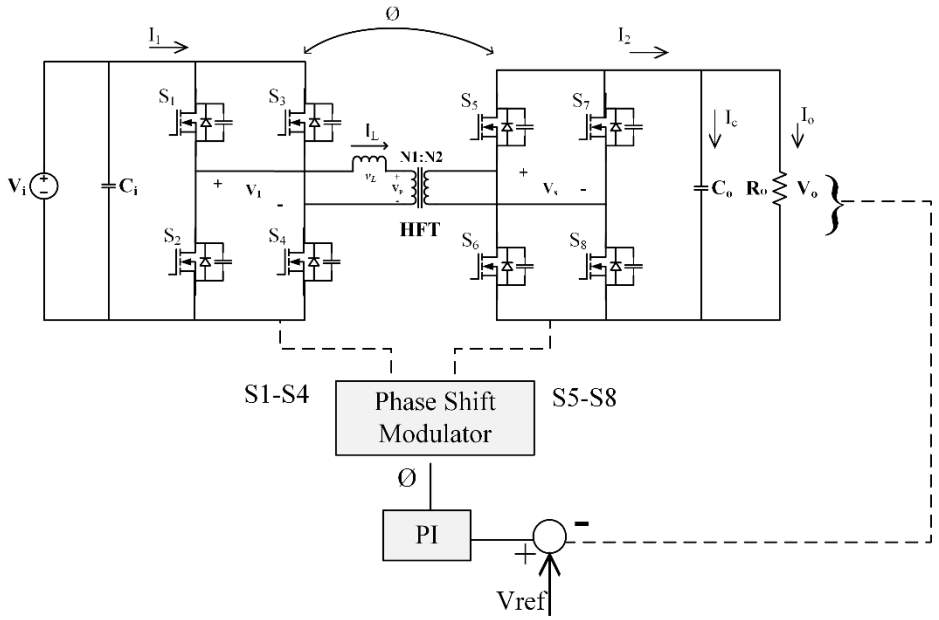

Fig.4.2. Circuit Diagram Depicting Voltage Mode Control of DAB Converter

Furthermore, this control technique works well with multiport systems, in which a single DAB converter can support several energy paths while preserving constant output voltage levels. All things considered, the CV loop makes it possible for the converter to operate safely, effectively, and steadily during the constant voltage phase of EV charging.

As shown in Fig.4.3 the block diagram explaining the control system for maintaining the constant voltage can be divided into three major parts with plant transfer function G(s) being the control to output transfer function which has been already derived as per the mathematical modelling of the converter for both output parameters; load voltage and load current. The next block is "H(s)", which is also called as the feedback sensor gain, and it is specified for a particular sensor which is being used. Talking about the practical implementation of this converter, the standard microcontrollers available works on the voltage level of 3.3Volts, hence the sensor gain has to be chosen in such a manner that it should be able to brough down the load parameters into a signal with voltage level of 3.3V. this sensor gain K_s is defined as:

$$- K_s = \frac{Actual\ Output\ Voltage\ (Physical\ Quantity)}{Sensor\ Output\ (Voltage\ or\ Digital\ Value)} \quad (4.1)$$

The choice and adjustment of a suitable controller is a crucial part of the Dual Active Bridge (DAB) converter's control system architecture. The DAB converter displays first-order system behaviour in both constant voltage (CV) and constant current (CC) modes, according to the analytical transfer functions that were determined in the previous

chapter. This streamlines the control design procedure and qualifies it for use with a Type-1 controller, like the Proportional-Integral (PI) controller, for implementation. Because of its simple design, ease of use, and ability to effectively eliminate steady-state error while maintaining sufficient dynamic response, the PI controller is frequently used in power converter applications. When it comes to the DAB converter, the PI controller modifies the phase shift command in accordance with the error between the reference and actual output voltage or current. For EV charging applications, a PI controller is adequate to deliver stable regulation, fast transient response, and low overshoot because of the reduced-order model's simplicity and first-order dynamics.

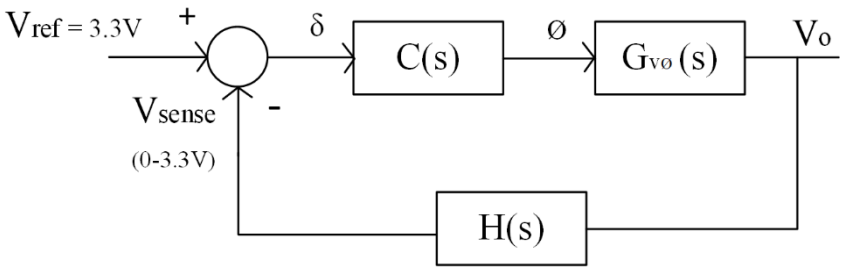

Fig.4.3 Control System Block Diagram for Voltage Mode Control

As per the transfer function for voltage mode control defined in previous chapter

$$G_{V\emptyset}(s) = \frac{12309.20}{s + 20.5023} \tag{4.2}$$

Considering sensor gain as feedback for voltage loop, to step down the load parameters at 3.3V standard range for microcontrollers/DSPs, with 5% overshoot at the output response,

$$H_v(s) = \frac{3.3}{630} = 0.\ 005238 \tag{4.3}$$

4.1.2 Design of Constant Current (CC) Controlled loop

As In the first stage of electric vehicle (EV) battery charging, the Dual Active Bridge (DAB) converter's constant current (CC) control loop is in charge of controlling the output current. In this mode, the converter ensures a safe and regulated charging rate by maintaining a set current output regardless of changes in battery voltage. This is particularly critical during the bulk charging stage of lithium-ion batteries, where a high and stable current is given until the battery voltage hits its rated threshold. In order to

modify the power flow and match the current demand, the DAB converter modifies the phase shift angle. Accurately tracking the reference current while reducing transient overshoot and maintaining system stability is the control goal in CC mode.

The PI controller processes the error to produce the proper control action after the CC loop utilizes a current sensor to measure the actual output current and compare it to the reference. The matching transfer function obtained from the reduced-order model serves as the foundation for the current loop controller's design. The controller parameters are tuned in CC mode to account for the generally faster response and tighter current regulation needed in this phase, even if the overall structure of the control system is still comparable to that employed in the voltage loop. To achieve the best charging pace, safeguard the battery, and get ready for a seamless transition into the constant voltage phase, the CC control loop must be implemented precisely.

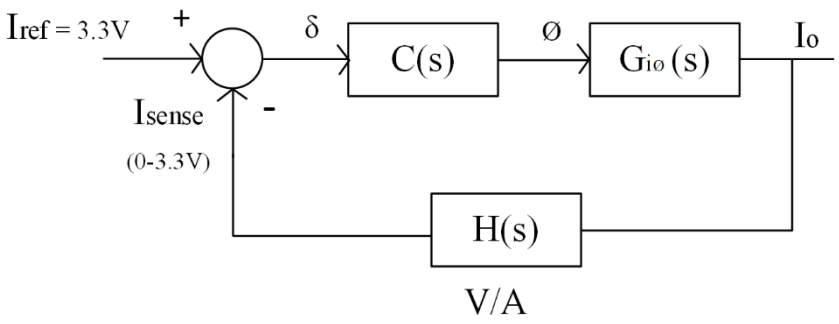

Fig.4.4 Control System Block Diagram for Current Mode Control

As per the transfer function for voltage mode control defined in previous chapter

$$G_{i\emptyset}(s) = \frac{224.2484}{s + 20.5023} \tag{4.4}$$

$$H_i(s) = \frac{3.3}{11.55} = 0.28571\ (\frac{V}{A}) \tag{4.5}$$

The current sensor used for sensing the load current will convert it into a signal within a range of 3.3V, Indicating that as per the design parameters if the load current is 11.55A (considering 5% overshoot in the system response) the signal will have a magnitude of 3.3V, similarly if load current is 1A the feedback signal will be 0.3V to a microcontroller.

4.2 Controller Design:

This section emphasizes on the methodical design of controllers for the Dual Active Bridge (DAB) converter's voltage and current regulation loops. Using the reduced-order modelling that was previously discussed, For the purpose of designing the controller parameters, two different approaches are taken into consideration: the first follows the guidelines given in the reference literature and selects controller gains based on desired transient performance metrics like settling time and percentage overshoot; the second uses the classical pole placement method, in which the controller is adjusted to position the closed-loop pole in a way that meets the requirements for stability and speed of response.

4.2.1 Approach-1: Considering Settling Time and Overshoot of The System

Considering the case of Constant Voltage (CV) mode of the control, the plant transfer function (which is also a control to output transfer function) is given by;

$$G_{V\emptyset}(s) = \frac{12309.20}{s + 20.5023} \tag{4.6}$$

And similarly, we have already defined the feedback sensor gain for the voltage loop given by, (Eqn.4.6)

$$H_v(s) = \frac{3.3}{630} = 0.\ 005238\,V \tag{4.7}$$

As per Fig.4.3 the controller transfer function C(s) for a PI controller is given in the form of;

$$C(s) = \left(K_p + \frac{K_i}{s}\right) = \left(\frac{K_p s + K_i}{s}\right) \tag{4.8}$$

Which makes a complete loop gain transfer function as;

$$G_L(s) = G_{v\emptyset}(s)H(s)C(s) = \frac{64.476(sK_p + K_i)}{s(s + 20.5235)} \tag{4.9}$$

Similarly, the close loop transfer function of the overall system can be defined as;

$$T(s) = \frac{G_{v\emptyset}(s)C(s)}{1 + G_{v\emptyset}(s)C(s)H(s)} \tag{4.10}$$

$$\therefore T(s) = \frac{\frac{12309.20}{(s+20.5235)}\left(\frac{sK_p + K_i}{s}\right)}{1 + \frac{64.476(sK_p + K_i)}{s(s+20.5235)}} \tag{4.11}$$

$$T(s) = \frac{102309.20(sK_p + K_i)}{s^2 + [20.5 + 64.476K_p]s + 64.476K_i} \tag{4.12}$$

As per ref. [4] the values of controller parameters are chosen for a maximum settling time of 30ms and a damping factor (ζ) greater than 0.69 defining the desired performance region of the system. Hence, considering a 5% maximum overshoot (M_p) and 30ms of settling time, for a second order closed loop system

$$M_p = 0.05 = e^{\frac{-\xi\pi}{\sqrt{1-\xi^2}}} \Rightarrow \xi = \mathbf{0.69} \tag{4.13}$$

Hence it matches the value of critical damping factor required. Similarly,

$$t_s = 0.03 = \frac{4}{\varepsilon\omega_n} \Rightarrow \boldsymbol{\omega_n = 193.236\ rad/sec} \tag{4.14}$$

Comparing the poles of obtained closed loop equation (Eqn.4.15) with the standard second order closed loop system ($\Delta_d(s)$) we get,

$$\Delta_d(s) = s^2 + 2\xi\omega_n s + \omega_n^2 \tag{4.15}$$

$$2\xi\omega_n = 2 \times 0.69 \times 193.236 = 20.5 + 64.476K_p$$

$$\boldsymbol{K_p = 3.818}$$

And,

$$\omega_n^2 = 64.476K_i \tag{4.16}$$

$$\therefore \boldsymbol{K_i = 579.13}$$

Thus, the total control system can be defined as;

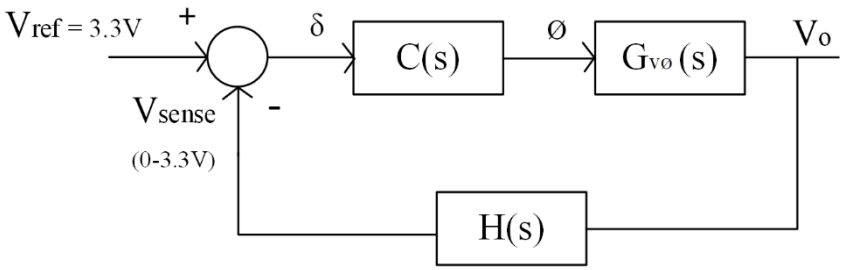

Fig.4.5. Control System Block Diagram for Voltage Mode Control

$$G_{V\emptyset}(s) = \frac{12309.20}{s + 20.5023}$$

$$H(s) = 0.0055$$

$$C(s) = \frac{3.818s + 579.13}{s}$$

$$G_L(s) = G_{v\emptyset}(s)H(s)C(s) = \frac{64.476(3.818s + 579.13)}{s(s + 20.5235)}$$

$$T(s) = \frac{G_{v\emptyset}(s)C(s)}{1 + G_{v\emptyset}(s)C(s)H(s)}$$

$$= \frac{102309.20(sK_p + K_i)}{s^2 + [20.5 + 64.476K_p]s + 64.476K_i}$$

$$= \frac{102309.20(3.818s + 579.13)}{s^2 + 266.66s + 37340.068}$$

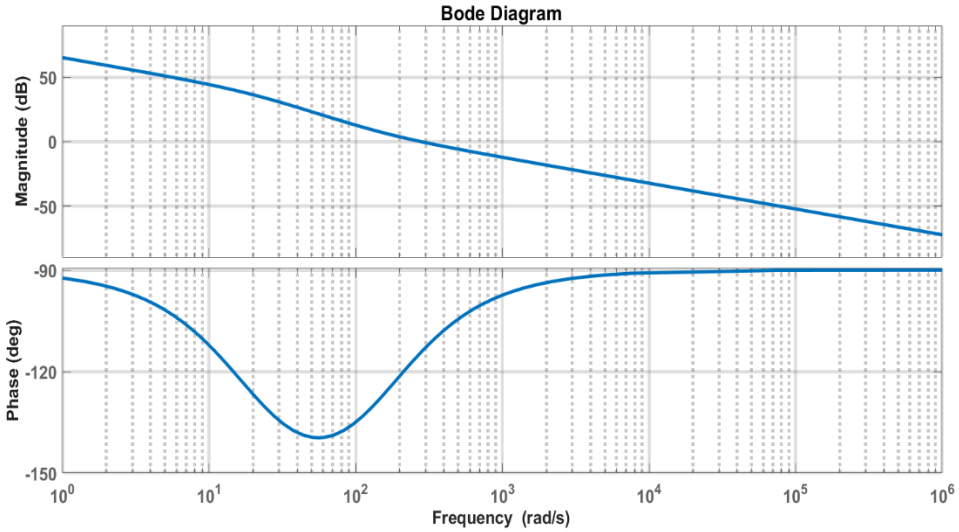

Fig.4.6. Bode Plot of Compensated Loop Gain Transfer Function

From the bode plot of close loop transfer function as shown in Fig.4.6 it can be seen that the closed loop system exhibits the stable response with both poles lying in the left half plane and have an adequate phase margin.

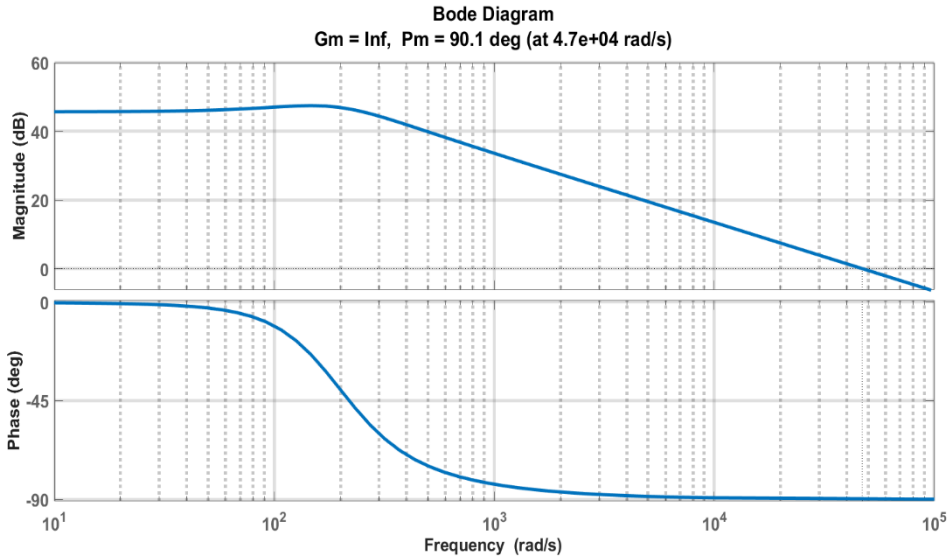

Fig.4.7. Bode Plot of Closed Loop Transfer Function With Calculated Controller Parameters

Similarly, considering current loop for Constant Current (CC) mode, as per Eqn.4.11 and Eqn.4.12

$$G_{i\emptyset}(s) = \frac{224.2484}{s + 20.5023} \tag{4.17}$$

And similarly, we have already defined the feedback sensor gain for the current loop given by, (Eqn.4.18)

$$H_i(s) = \frac{3.3}{11.55} = 0.\ 2857\ V \tag{4.18}$$

As per Fig.4.3 the controller transfer function C(s) for a PI controller is given in the form of;

$$C(s) = \left(K_p + \frac{K_i}{s}\right) = \left(\frac{K_p s + K_i}{s}\right) \tag{4.19}$$

Which makes a complete loop gain transfer function as;

$$G_L(s) = G_{i\emptyset}(s)H(s)C(s) = \frac{64.476(sK_p + K_i)}{s(s + 20.5235)} \tag{4.20}$$

It can be seen from the Eqn.4.20 that for both voltage and current loop, the loop gain transfer function is in the same form (same DC gain) hence, as mentioned above the PI controller parameters for both the loops are same

$$\therefore \boldsymbol{K_p = 3.818} \tag{4.21}$$

$$\therefore \boldsymbol{K_i = 579.13} \tag{4.22}$$

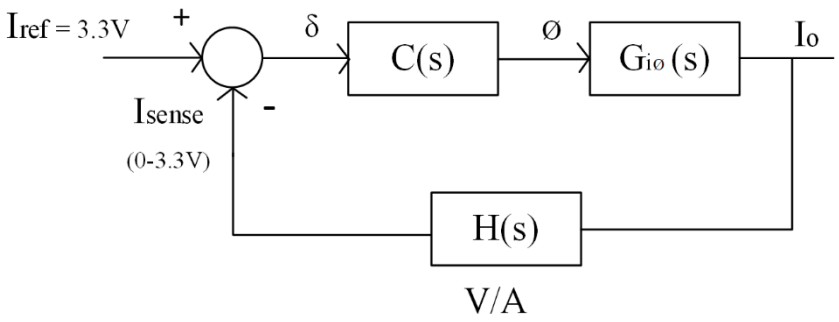

Fig.4.8. Control System Block Diagram for Current Mode Control

$$G_{i\emptyset}(s) = \frac{224.2484}{s + 20.5023}$$

$$H(s) = 0.2857$$

$$C(s) = \frac{3.818s + 579.13}{s}$$

$$G_L(s) = G_{i\emptyset}(s)H(s)C(s) = \frac{64.476(3.818s + 579.13)}{s(s + 20.5235)}$$

$$T(s) = \frac{G_{v\emptyset}(s)C(s)}{1 + G_{v\emptyset}(s)C(s)H(s)}$$

$$= \frac{224.2484(sK_p + K_i)}{s^2 + [20.5 + 64.476K_p]s + 64.476K_i}$$

$$= \frac{224.2484(3.818s + 579.13)}{s^2 + 266.66s + 37340.068}$$

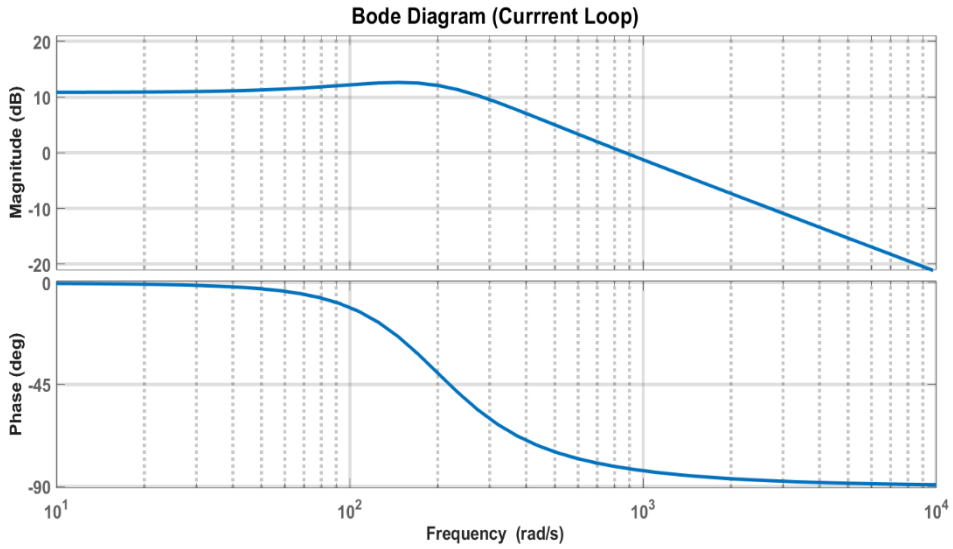

Fig.4.9. Bode Plot of Closed Loop Transfer Function With Calculated Controller Parameters

Once the Parameters were obtained, the closed loop simulations were performed with the MATLAB/Simulink where for CV mode, the resistive load was chosen and was step down in the order of 100%-75%-50%-25% similarly for CC mode it was set in the increasing manner of 25%-50%-75%-100%. Below are the simulation results obtained from the calculated PI parameters subjected to first method of designing PI controller parameters.

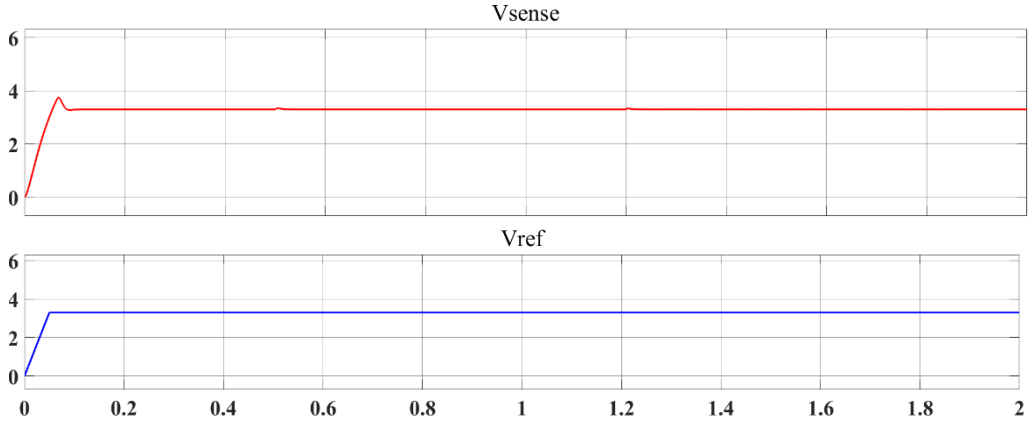

Fig.4.10. Comparing reference voltage (3.3V) with the sensed load voltage (output of feedback sensor gain) which was brought down on the scale of 3.3V

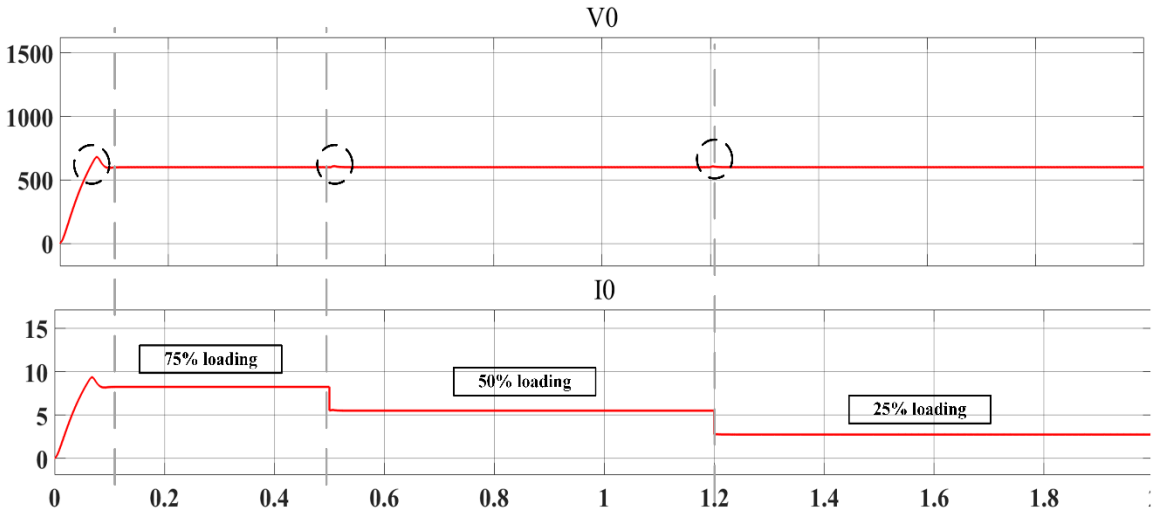

Fig.4.11. Load Voltage and Load Current with Varrying Load Conditions

As shown in Fig.4.10 the load current is varied with respect to the load from 75% loading to 25% loading. Considering this change in the load with EV battery characteristics mentioned in the Chapter 3, it can be described as the Constant Voltage (CV) stage of the battery as once the rated battery voltage is reached current starts decreasing till it reaches End of Charge (EOC) which is tried to be simulated in this manner.

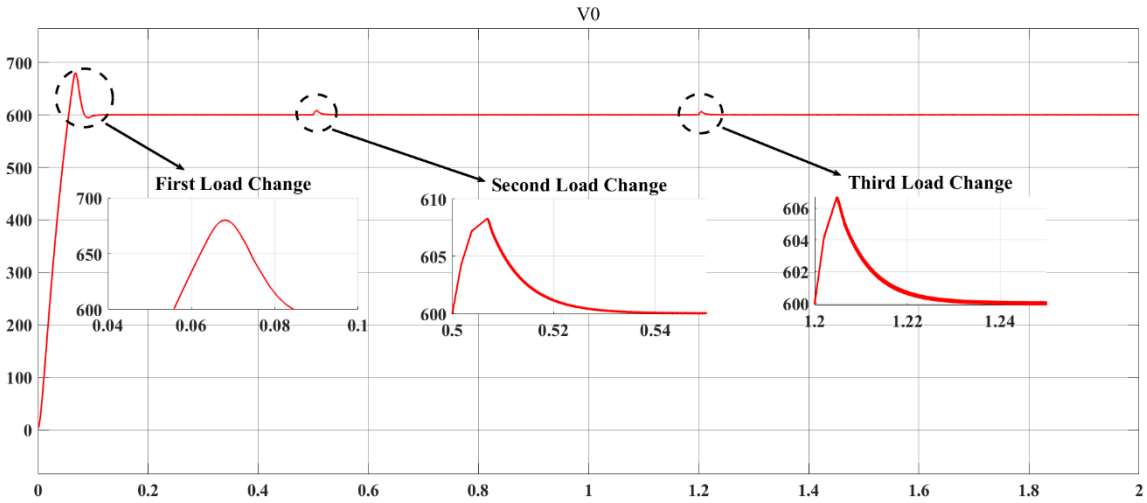

Fig.4.12. Load Voltage with Overshoots at Each Instant of Load Change Before it Settles Down at Constant Voltage

As per Fig.4.11, variations in the load voltage are observed at the instances of load change. In the first load change when load was brought down to 75% loading the peak overshoot observed was around 11% and at the instance of second load change it decreased to 1.8% and at the last instant it was negligible proving the controller works according to

desired results. Similarly, during settling it took around 20-30ms for each instance to get settled.

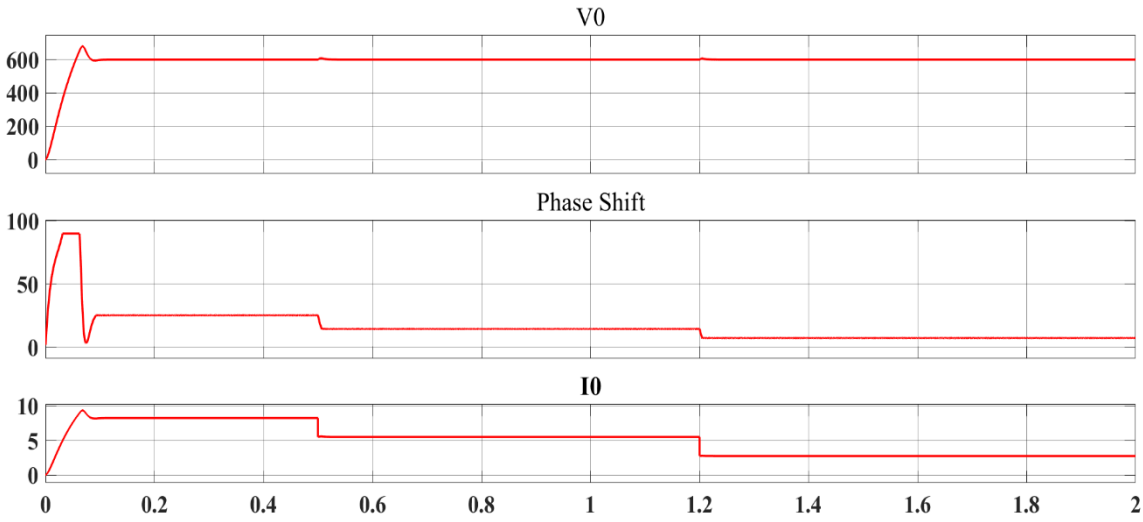

Fig.4.13. Load Voltage, Load Current and Phase Shift with Varrying Load Conditions for CV mode

In case of CV mode as discussed earlier, during varying load conditions the load voltage remains constant by adjusting the phase shift between the bridges accordingly. This can be seen from Fig.4.12 as at rated condition the phase shift first reaches its rated value, and once the rated voltage is reached, as per the instances of change in the load it adjusts itself to a fixed value for that interval to obtain the desired CV mode state of the converter.

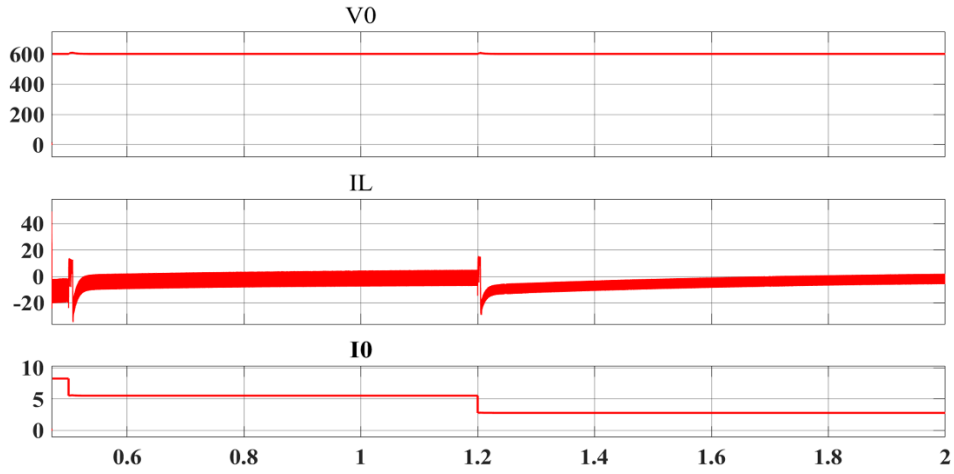

Fig.4.14. Load Voltage, Load Current and Inductor Current with Varrying Load Conditions (50%-25%) for CV mode

As shown in Fig.4.13 the load voltage is varied with respect to the load from 25% loading to 100% loading. Considering this change in the load with EV battery characteristics mentioned in the Chapter 3, it can be described as the Constant Current (CC) stage of the battery as current starts increasing till the rated battery voltage is reached in this case with our design parameters can be termed as at 100% loading which is tried to be simulated in this manner.

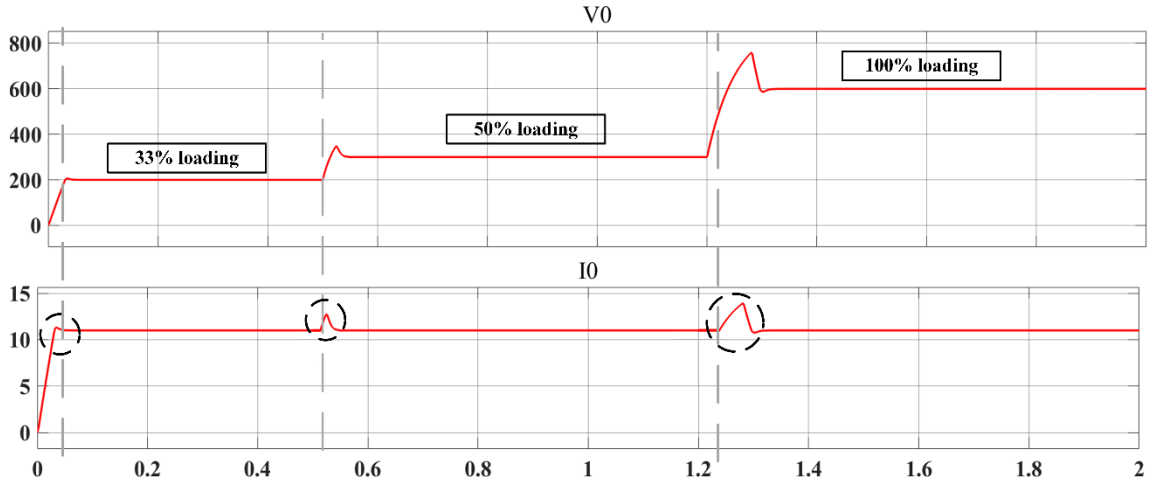

Fig.4.15. Load Voltage and Load Current with Varrying Load Conditions

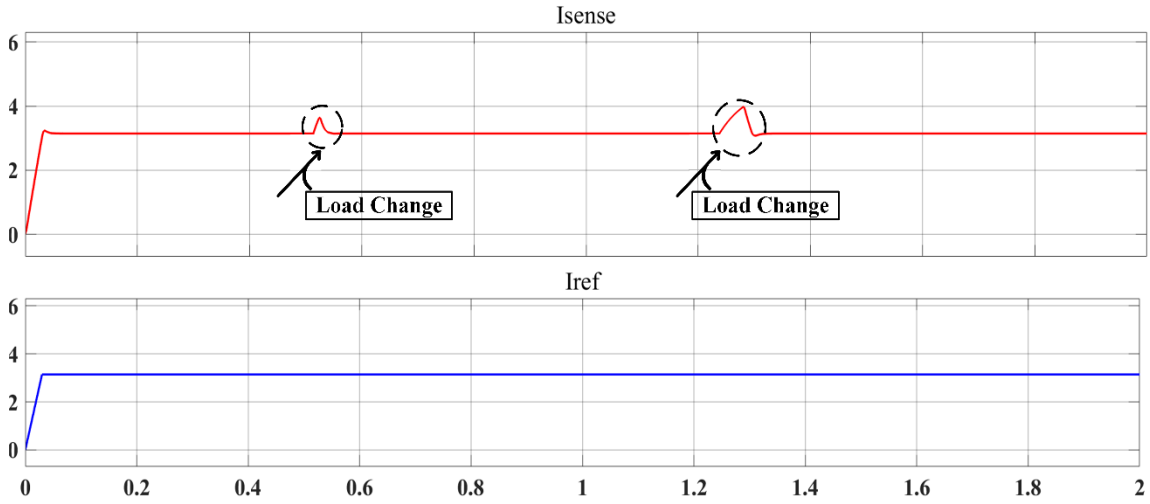

Fig.4.16. Comparing reference current (3.3V) with the sensed load current (output of feedback sensor gain) which was brought down on the scale of 3.3V

From Fig.4.16 it can be noted that the phase shift across both the voltages of the inductor (V_1 and V_P) is implemented with the output voltage being 50% of its rated value, maintaining same load current.

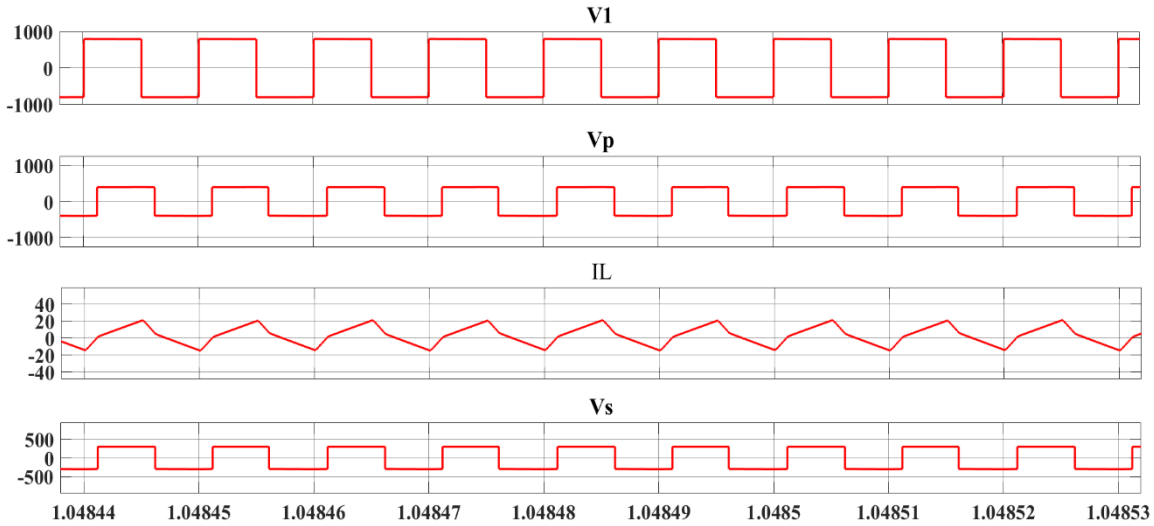

Fig.4.17. Primary Bridge Output Voltage (V_1), Primary Voltage (V_P), Inductor Current (I_L) and Secondary Voltage (V_S) for 50% Loading

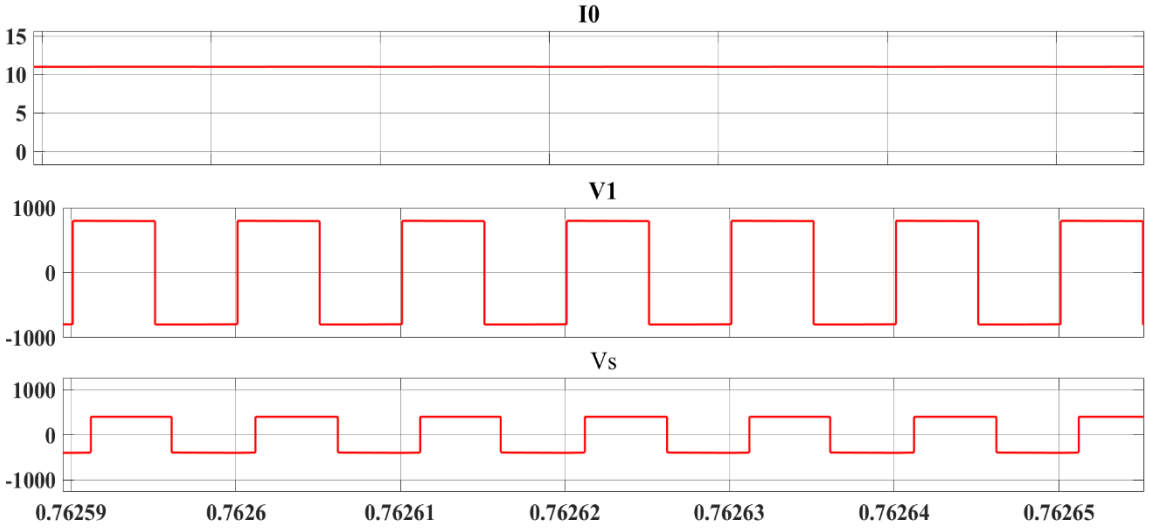

Fig.4.18. Constant Load Current, Primary Bridge Output Voltage (V_1) and Secondary Voltage (V_S) for 50% Loading

Similar analysis can be observed for the case of 100% rated loading, where it can be seen that for a constant current of 11A (rated) the load voltage and similarly the secondary side voltage of the HFT (high Frequency Transformer) achieves the rated value (Fig.4.18). A conclusion can be drawn as for a same value of PI controller parameters, with similar system parameters (%overshoot, settling time) the converter is able to operate at both CC and CV modes. The high overshoot near the rated values is because of the design of PI controller parameters were carried out considering these rated values which also are the worst case for the converter, but as it can be seen for lower loadings the converter was able to exhibit better performance.

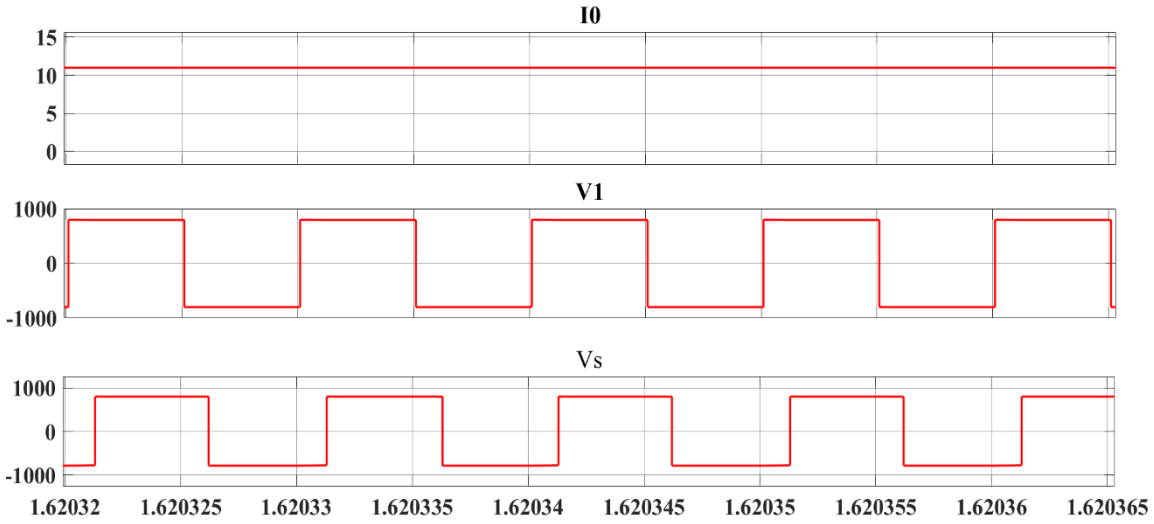

Fig.4.19. Constant Load Current, Primary Bridge Output Voltage (V_1) and Secondary Voltage (V_S) for 100% Loading

4.2.2 Approach-2: Considering Desired Crossover Frequency of The System

This method follows a classical design approach for obtaining PI controller parameters, where a pole is placed at a particular frequency to obtain a desired crossover frequency from where the desired loop gain bandwidth and K_P, K_i parameters can be obtained.

For simplifying the analysis this method is divided into 6 steps:

- Step-1: Define Plant Transfer Function ($G_{V\emptyset}(s)$) and Sensor gain (H(s)).
- Step-2: Calculate the "Uncompensated loop gain" with (C(s)) =1.
- Step-3: Plot the bode plot and calculate the required frequency f_L at which the zero should be added to achieve the desired crossover frequency f_c.
  *(*Note: As per the ref., the desired crossover frequency should be one twentieth of the switching frequency)*
- Step-4: Define high frequency gain $G_{c\infty}$ which is chosen to obtain the desired crossover frequency.
- Step-5: Calculate the Controller transfer function from obtained parameters.
- Step-6: Define Compensated loop gain (which will be product of un-compensated loop gain and obtained controller transfer function)

- For CV Mode:

$$G_{V\emptyset}(s) = \frac{12309.20}{s + 20.5023} \tag{4.23}$$

$$H(s) = 0.0055 \tag{4.24}$$

The uncompensated loop gain $G_{L0}(s)$ is calculated by putting C(s)=1 in the loop gain transfer function and it is given as.

$$G_{L0(v)}(s) = G_{v\emptyset}(s)H(s).1 = \frac{67.7006}{s + 20.5235} \tag{4.25}$$

$$G_{L0(v)}(s) = \frac{T_0}{1 + \frac{s}{w_0}} = \frac{\frac{67.7006}{20.52}}{1 + \frac{s}{20.52}} = \frac{3.299}{1 + \frac{s}{20.52}} \tag{4.26}$$

$$\therefore T_0 = 3.299$$

$$\therefore f_0 = 3.262Hz$$

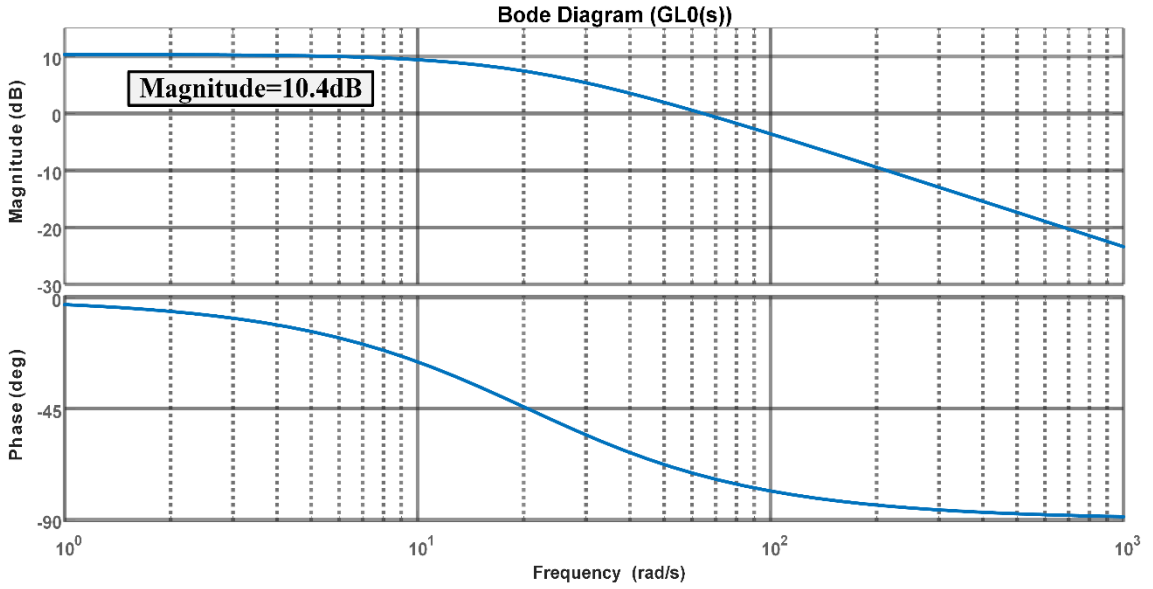

Fig.4.20. Bode Plot of Uncompensated Loop Gain Transfer Function ($G_{L0}(s)$)

The next part of designing the controller is to calculate the high frequency gain "$G_{c\infty}$" which is chosen to obtain the desired crossover frequency. The desired crossover frequency is taken as one twentieth of the switching frequency, hence for a 100kHz switching frequency,

$$f_c = 5000Hz \tag{4.27}$$

$$G_{c\infty} = \frac{f_c}{T_0 f_0} = \frac{5000}{3.29 \times 3.26} = 306.74 \tag{4.28}$$

The frequency at which inverted zero is to be added to achieve the desired crossover frequency is chosen sufficiently lesser than the desired crossover frequency, such that an adequate phase margin (θ) is to be maintained.

$$f_L = \frac{f_c}{10} = 500Hz = 3141.592rad/sec \tag{4.29}$$

Where, θ defines the desired phase margin for loop transfer function (in the case of parameters we have chosen, it is safe to consider the PM of minimum 60˚).

Hence, the controller transfer function (C(s)) can be defined as;

$$C(s) = G_{c\infty}(1 + \frac{w_L}{s}) \tag{4.30}$$

Hence, from Eqn.4.24 and Eqn.4.26,

$$C(s) = 306.74\ (1 + \frac{3141.592}{s}) \tag{4.31}$$
$$= \frac{306.74s + 9.63 \times 10^5}{s}$$

Therefore, the loop gain transfer function is defined by,

$$G_L(s) = G_{v\emptyset}(s)H(s)C(s) = \frac{102.57(306.74s + 9.63 \times 10^5)}{s(s + 20.5235)} \tag{4.32}$$

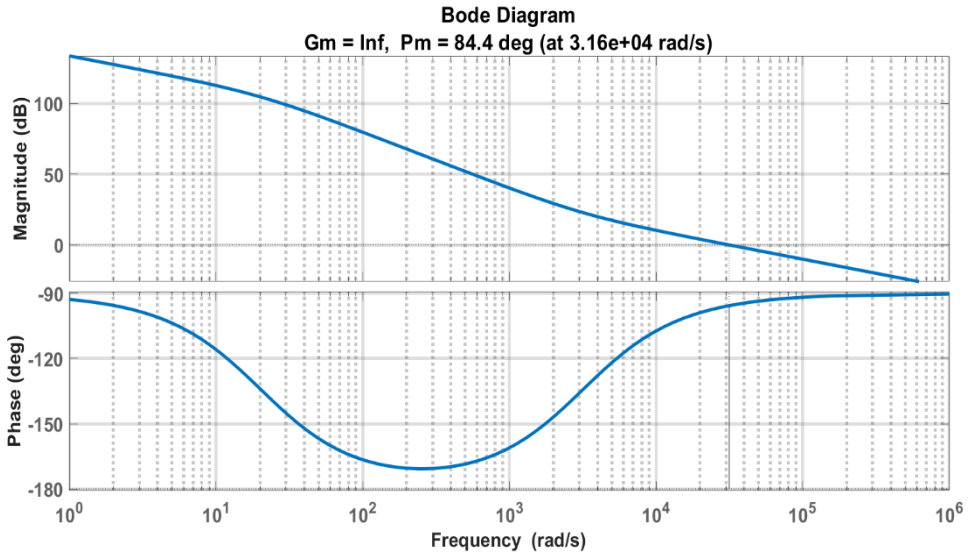

Fig.4.21. Bode Plot of Compensated Loop Gain Transfer Function ($G_L(s)$)

It can be seen from the bode plot of obtained loop gain transfer function (Fig. 4.21) the adequate phase margin of approximately 84˚ is obtained which signifies the stable

operation of the system along with the desired crossover frequency of (5kHz) $3.16x10^4$ rad/sec.

- For CC mode:

$$G_{i\emptyset}(s) = \frac{224.2484}{s + 20.5023}$$

$$H(s) = 0.2857$$

The uncompensated loop gain $G_{L0}(s)$ is calculated by putting C(s)=1 in the loop gain transfer function and it is given as.

$$G_{L0(v)}(s) = G_{v\emptyset}(s)H(s).1 = \frac{67.7006}{s + 20.5235} \tag{4.33}$$

$$G_{L0(v)}(s) = \frac{T_0}{1 + \frac{s}{w_0}} = \frac{\frac{67.7006}{20.52}}{1 + \frac{s}{20.52}} = \frac{3.299}{1 + \frac{s}{20.52}} \tag{4.34}$$

$$\therefore T_0 = 3.299$$

$$\therefore f_0 = 3.262Hz$$

Since the uncompensated loop gain transfer function of CC mode is similar to that of CV mode, it can be concluded that like first approach the value of PI parameters for both the loops is same.

And hence, pursuing the simulation analysis for both modes;

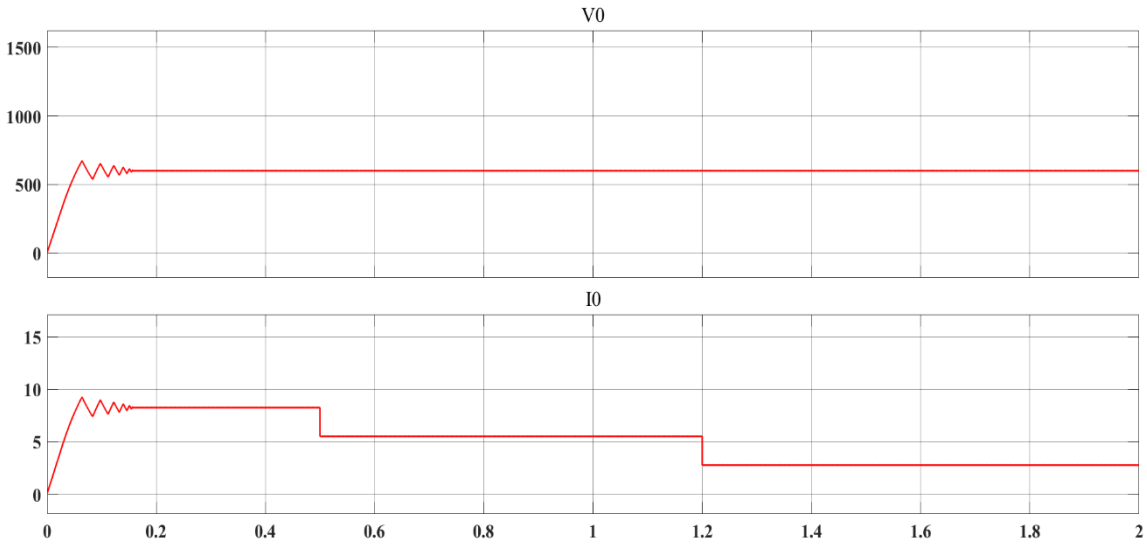

Fig.4.22. Load Voltage and Load Current with Varrying Load Conditions using Approach-2 for CV mode

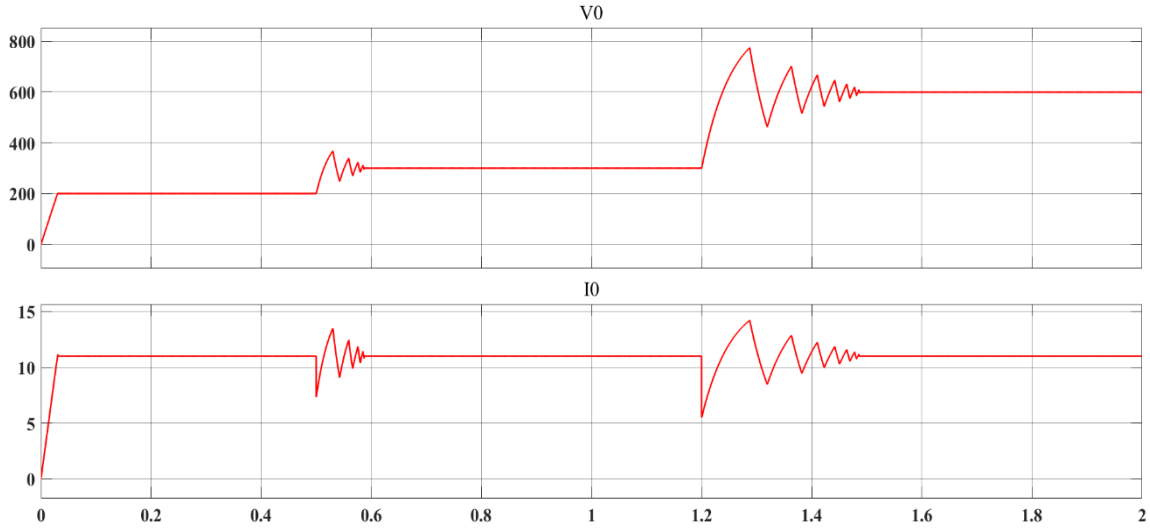

Fig.4.23. Load Voltage and Load Current with Varrying Load Conditions Using Approach-2 for CC Mode

As seen from Fig.4.22 and Fig.4.23 for both CV and CC modes, after substituting the calculated values of PI parameters in the control architecture both systems show similar responses with increased noise profile at settling stage as well as when the load is varied. Though the desired crossover frequency was achieved along with adequate phase margin, and high loop bandwidth the question remains on the increased noise profile on both the cases.

If observed clearly, from the bode plot of compensated loop gain transfer function (Fig.4.19) the gain of the system at switching frequency (100kHz) is near about -10dB which is clearly more than the standard limit of gain at switching frequency for high frequency controller design (<-40dB). (Fig.4.24)

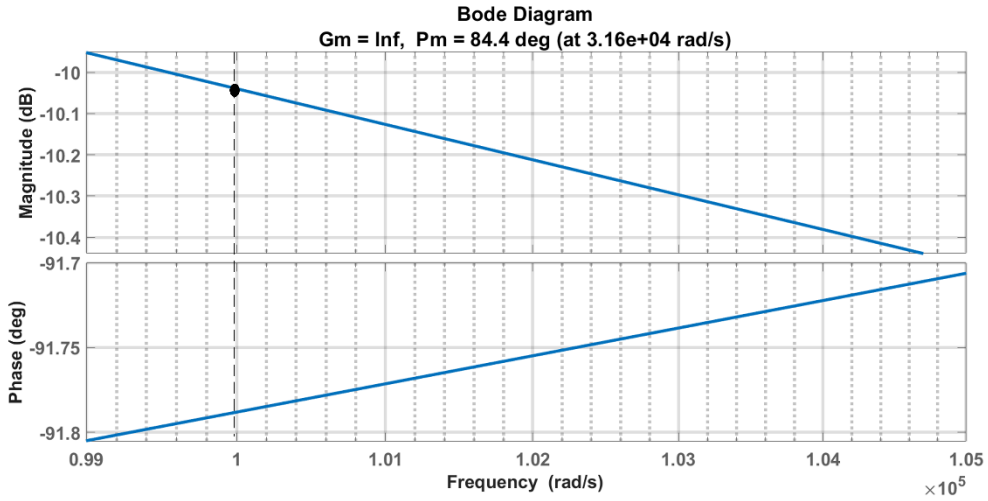

Fig.4.24. Bode Plot of Compensated Loop Gain Transfer Function ($G_L(s)$) (Zoomed)

This high gain at switching frequency causes trouble, as the control system processes errors and generates a compensating action and if the loop gain is high at the switching frequency, any high frequency disturbances (like switching ripple, EMI or sensor noise) gets amplified rather than attenuated. So, it becomes necessary to keep this gain at high switching frequency gain at the minimum value as possible.

This can be done by adjusting the crossover frequency and thus modifying the PI parameters to check at a instant where this gain is reduced to less than -40dB. Therefore, after calculating and substituting for each crossover frequency it was observed that, at the value of 1000Hz (1kHz) crossover frequency, the gain was near about -40.72dB. (Fig.4.25) thus, showing signs of reduced noise profile at the load parameters of the converter.

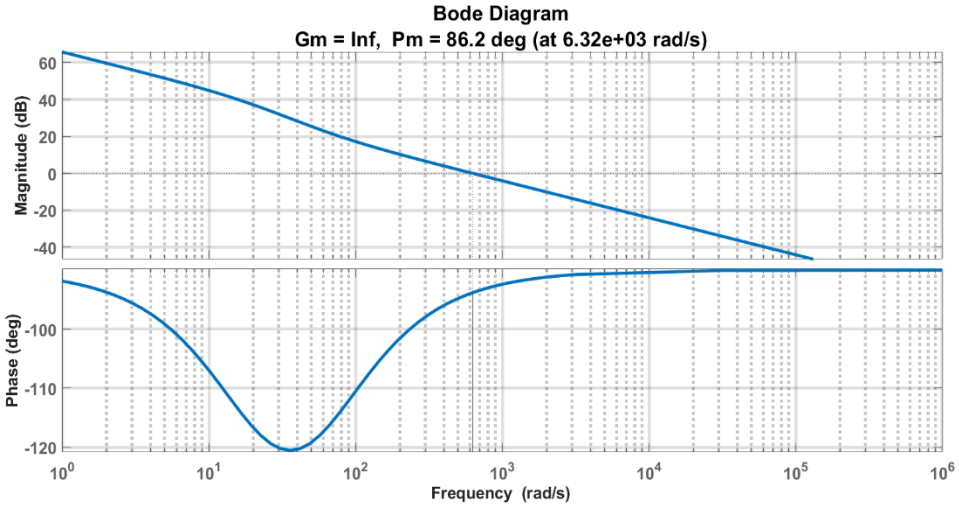

Fig.4.25(a). Bode Plot of Compensated Loop Gain Transfer Function ($G_L(s)$) with Crossover Frequency of 1kHz

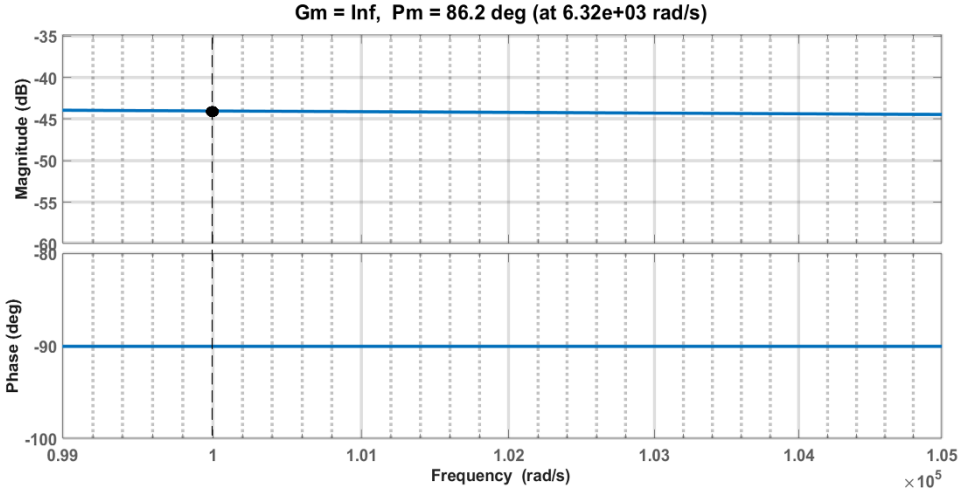

Fig.4.25(b). Bode Plot of Compensated Loop Gain Transfer Function ($G_L(s)$) with Crossover Frequency of 1kHz (Zoomed)

This calculated PI parameters were then used for performing the simulation analysis under the environment of same design parameter consideration.

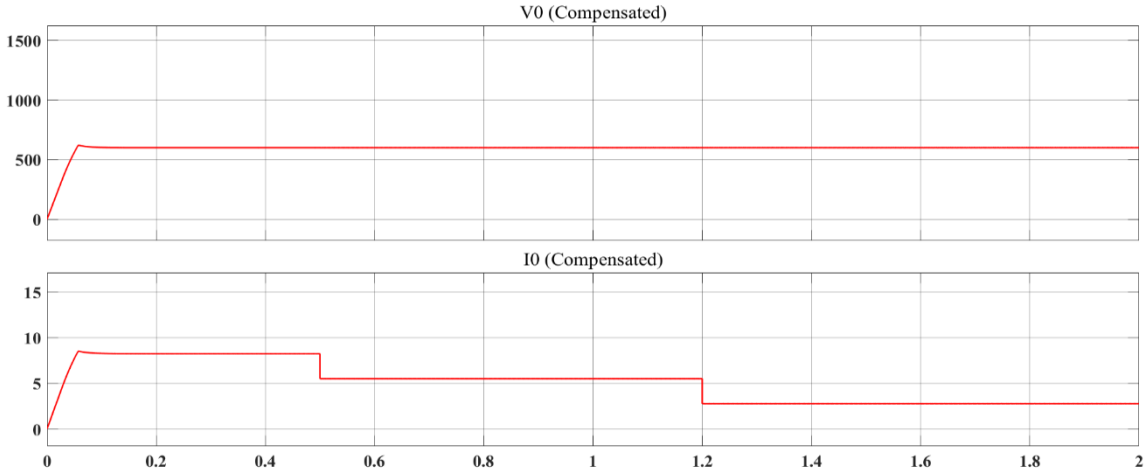

Fig.4.26(a). Load Voltage and Load Current with Varrying Load Conditions using New Compensation Parameters (1kHz Crossover Frequency) for CV Mode

As it can be seen from Fig.4.26(a) where the simulation for CV mode was performed for same loading conditions, the output response profile was much improved with very finely tuned response with minimal overshoots, along with desired settling time. But it is to be noted as shown in Fig.4.26(b). which shows the zoomed version of load voltage plot, the small noise distractions can be observed which do not exactly impact the loading conditions and desired profiles of load parameters but since this distortions vary in maximum range of (-1V to 1V) , this magnitude is enough to change the controlling parameter (Phase shift) at every instance of distortion resulting in calculative burden on the controller, thus causing excessive runtime for the controller in practical applications.

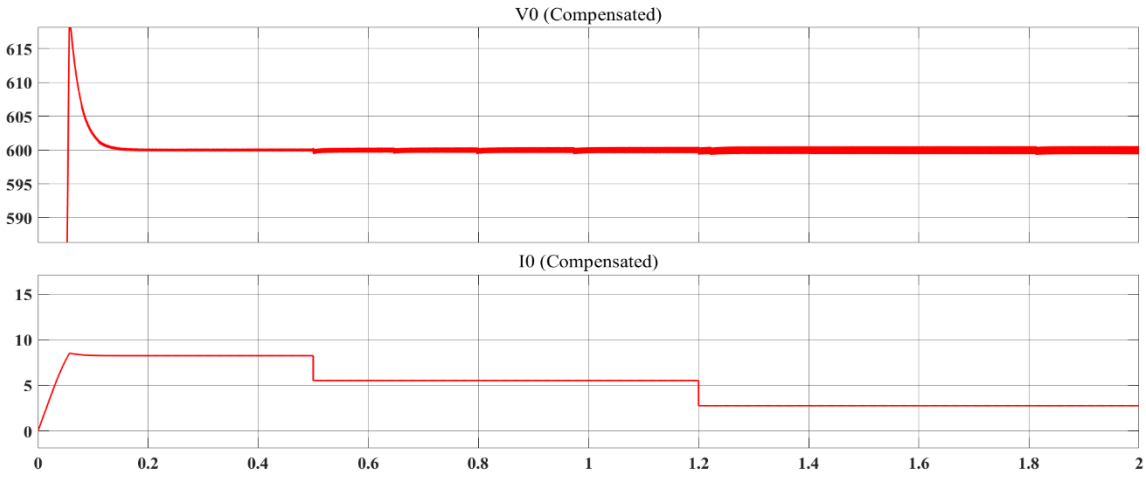

Fig.4.26(b). Load Voltage with New Compensating Parameters (Zoomed)

Similar analysis can be concluded for CC mode, as shown in (Fig.4.26(c)) where compared to response observed by Approach 1, the current profile shows an undershoot along with a overshoot before settling down to rated value, with more magnitude, though the noise profile is improved significantly by adjusting the crossover frequency (which is already more than the crossover frequency of loop gain transfer function calculated through approach 1) and response exhibit tuned profile for loading parameters.

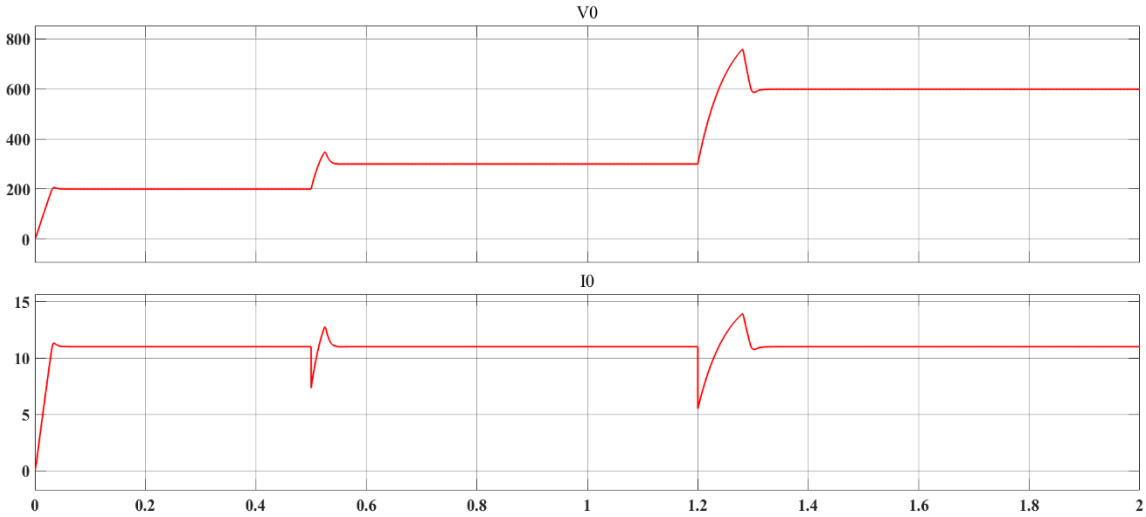

Fig.4.26(c). Load Voltage and Load Current with Varrying Load Conditions using New Compensation Parameters (1kHz Crossover Frequency) for CC Mode

It can be concluded based upon both the approaches that, the first approach is based on time-domain performance requirements, namely the percentage overshoot of the closed-loop response and the intended settling time. When the control objective stresses predictable system dynamics and smooth transient behaviour, this approach is especially practical and straightforward. Appropriate PI gains are then determined by using the damping ratio and natural frequency, which are obtained from the given settling time and overshoot using second-order system approximations. This method works effectively for systems that need well-damped responses and little transient variation because it gives immediate insight into how the system reacts to disturbances or changes in reference. Frequency-domain features like phase margin and gain crossover frequency, which are crucial in high-bandwidth systems or where switching noise and electromagnetic interference are issues, are not specifically addressed by this approach.

The second technique, often referred to as the pole placement or frequency shaping method, uses a frequency-domain strategy based on the intended crossover frequency and

phase margin. By adjusting the open-loop gain and making sure the crossover frequency falls within a bandwidth that strikes a compromise between speed and robustness, the PI controller in this technique is made to position the closed-loop system pole at a specific point on the complex plane. Better control over dynamic response and loop gain characteristics is provided by this approach, particularly for systems that are prone to disturbances or operate in noisy environments. Applications needing large bandwidth, quick dynamic performance, and improved rejection of high-frequency noise are a good fit for it. Additionally, it makes phase margin and gain margin analysis easier, which is crucial for digitally controlled power converters like DAB.

Table 4.1. Comparison of Various Controller Design Techniques

Approach	PI Parameters	Loop gain bandwidth	Overshoot profile	Dynamic response	Noise Profile
Approach-1	K_p = 3.818 K_i = 579.13	Low (f_c=500Hz)	Lowest	Slow	Lowest
Approch-2	K_p = 306.74 K_i = 96300	High (f_c =5kHz)	High	Fastest	High
Modified Approach-2	K_p=80.481 K_i =3992.37	Moderate (f_c=1kHz)	Low	Fast	Moderate

4.2 Peak Current Mode Control (PCMC) of DAB Converter:

An advanced control technique termed Peak Current Mode Control (PCMC) is used in power converters to increase current regulation, establish inherent current limiting, and improve transient response. By directly controlling the inductor current peak, PCMC provides an extra layer of dynamic control to Dual Active Bridge (DAB) converters, as opposed to depending just on feedback from average current or voltage. In applications where accurate current management and quick reaction to load variations are crucial, like electric vehicle (EV) charging, this technique is especially helpful. By providing protection against unexpected surges or short circuits, permitting cycle-by-cycle current limitation, and lessening the strain on external voltage or current loops during transient occurrences, PCMC improves system robustness.

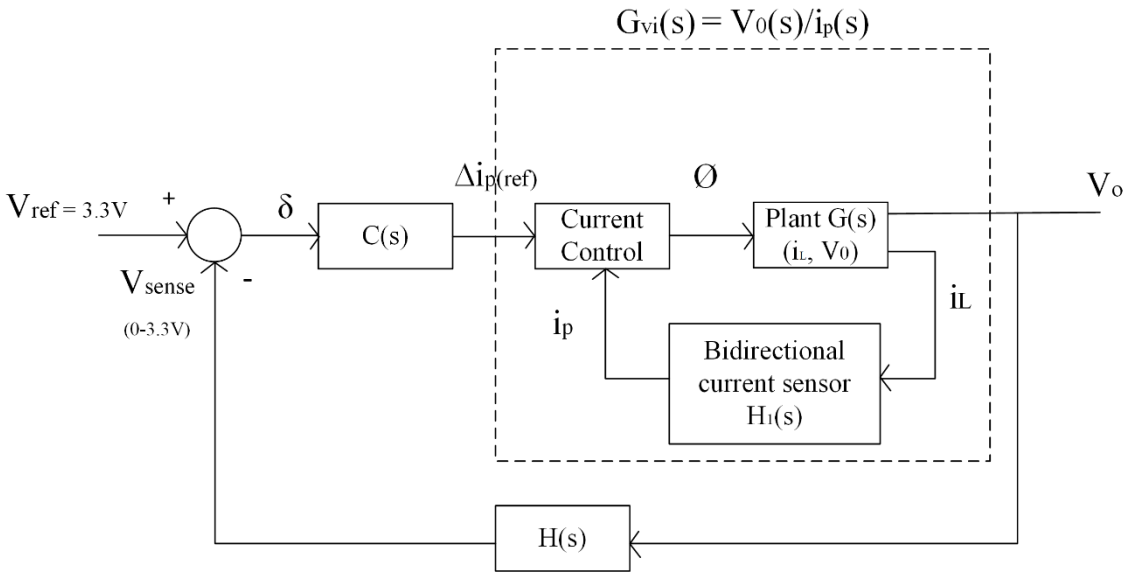

Fig.4.27. Peak Current Mode Control of DAB Converter

In order to apply PCMC, the instantaneous inductor current is measured and compared to a reference that is dynamically created as shown in Fig.4.27 , this reference is dynamic and is the difference between the reference and sensed voltages which vary as per the intervals depending upon the bandwidth of the outer loop. A control action, modification of the phase shift, initiates when the inductor current peak reaches this reference value. Compared to traditional control loops, this behaviour alters the power flow more responsively. It is necessary to create a transfer function that captures the relationship between the reference current and the ensuing inductor current peak to design and analyse such a control system. The inductor current waveform, which is typically trapezoidal under steady-state SPS modulation, is approximated, linearized around the operating point, and its slope properties are analysed as part of the derivation process. The resulting transfer function sheds light on the converter's small-signal performance under PCMC.

As per Fig.4.27 the inductor current is determined as;

$$i_L(\theta) = \begin{cases} \dfrac{V_1 + V_s}{\omega L}\theta - i_x & 0 \le \theta \le \emptyset \\ \dfrac{V_1 - V_s}{\omega L}(\theta - \emptyset) + \dfrac{V_1 + V_s}{\omega L}\emptyset - i_x & 0 \le \theta \le \pi \end{cases} \quad (4.35)$$

Therefore, due to half wave symmetry the value of inductor current at 'π' is calculated as, from Eqn.4.35,

$$i_L(\pi) = \frac{V_1 - V_s}{\omega L}(\pi - \emptyset) + \frac{V_1 + V_s}{\omega L}\emptyset - i_x = i_x \tag{4.36}$$

$$\therefore i_x = \frac{1}{2\omega L}[V_1(\pi) - V_s(\pi - 2\emptyset)] \tag{4.37}$$

From Eqn.4.36 and Eqn.4.37

$$i_T = \frac{1}{2\omega L}[V_1(2\emptyset - \pi) - V_s(\pi)] \tag{4.38}$$

Since, this transition current (i_T) is responsible for the changing phase shift accordingly, rather than considering (i_x) as the peak current (which actually in the case it is) we consider i_T as the peak current and can be concluded as;

$$i_T = i_p \tag{4.39}$$

from the modelling of DAB converter explained in chapter 3, the reduced order modelling equation modified with respect to θ can be given as;

$$\frac{dV_c}{d\theta} = -\frac{I_0}{\omega RC} + \frac{nV_i}{\omega^2 LC}\emptyset\left[1 - \frac{\emptyset}{\pi}\right] \tag{4.40}$$

Like normal CV-CC mode configuration if the converter was controlled by Phase Shift, then the Eqn.4.40 should be linearized around the operating point. But, in the case of PCMC the control is made with the "peak current" of the inductor.

Hence from Eqn.4.41

$$\emptyset = \frac{2\omega L i_p - \pi n V_c + V_i \pi}{2V_i} \tag{4.41}$$

Substituting Eqn.4.40 in the Eqn.4.41

$$\frac{dV_c}{d\theta} = -\frac{I_0}{\omega RC} + \frac{n}{4\omega^2 LCV_i} \times \left[-\frac{4\omega^2 L^2 i_p^2}{\pi} + 4\omega n L v_0 i_p - n^2 \pi v_0^2 + \pi V_i^2\right] \tag{4.42}$$

Using perturbation and linearization around operating point,

$$\frac{d\Delta v_0}{d\theta} = \left[\frac{n^2 I_p}{\omega CV_i} - \frac{n^3 \pi V_0}{2\omega^2 LCV_i}\right]\Delta v_0 + \left[\frac{2LnI_p}{\pi CV_i} + \frac{n^2 V_0}{\omega CV_i}\right]\Delta i_p \times \left[-\frac{1}{\omega RC}\right]\Delta i_0 \tag{4.43}$$

Using the Laplace transform, the obtained transfer functions are;

$$\frac{\Delta \boldsymbol{v_0}}{\Delta \boldsymbol{i_p}} = \boldsymbol{G_{vi}(s)} = \frac{\dfrac{\boldsymbol{n^2 V_0}}{\boldsymbol{CV_i}} - \dfrac{\boldsymbol{2\omega L I_p}}{\boldsymbol{\pi CV_i}}}{\boldsymbol{s} + \left(\dfrac{\boldsymbol{1}}{\boldsymbol{RC}} - \dfrac{\boldsymbol{n^2 I_p}}{\boldsymbol{CV_i}} + \dfrac{\boldsymbol{n^3 \pi V_0}}{\boldsymbol{2\omega LCV_i}}\right)} \tag{4.44}$$

As per the design parameters shown in Table 4.2,

Table 4.2. Design Parameters of DAB

Parameter	Notation	Value
Input Voltage	V_i	800 volts
Output Voltage	V_0	600 volts
Typical Power Level	P_{max}	10-25 kW
Target Output Power	P_0	6.6 kW
Inductor	L	80 µH
Nominal Phase Shift	$D_{\emptyset}$	38˚ (0.663)
Switching Frequency	f_s	100kHz
Output capacitor	C_0	1000 µF
Turns ratio	N1:N2	1.33:1

$$\emptyset = \frac{2\omega L i_p - \pi n V_c + V_i \pi}{2V_i} \tag{4.45}$$

$$0.663 = \frac{2 \times 2 \times \pi \times 100 \times 10^3 \times 80 \times 10^{-6} i_p - \pi \times 1.33 \times 600 + 800\pi}{2 \times 800}$$

$$I_p = 10.48A \tag{4.46}$$

$$G_{vi}(s) = \frac{\frac{n^2 V_0}{C V_i} - \frac{2\omega L I_p}{\pi C V_i}}{s + \left(\frac{1}{RC} - \frac{n^2 I_p}{C V_i} + \frac{n^3 \pi V_0}{2\omega L C V_i}\right)}$$

$$= \frac{1326.675 - 419.2}{s + (18.335 - 23.17 + 55.14)}$$

$$\boldsymbol{G_{vi}(s) = \frac{907.475}{s + 50.305}} \tag{4.47}$$

After deriving the peak current to load voltage transfer function, as shown in Eqn.4.35 and similarly in the Fig.4.26 the next step is to design a current controller, and the voltage controller as per the previously discussed approaches (Section 4.2) Since the controller designed by the modified approach 2 where the transfer function for phase shift to load voltage was derived, for crossover frequency of 1kHz. The same crossover frequency was chosen for outer voltage loop, and for quick response from the inner loop the crossover frequency for inner current loop was chosen five times that of outer loop (5kHz).

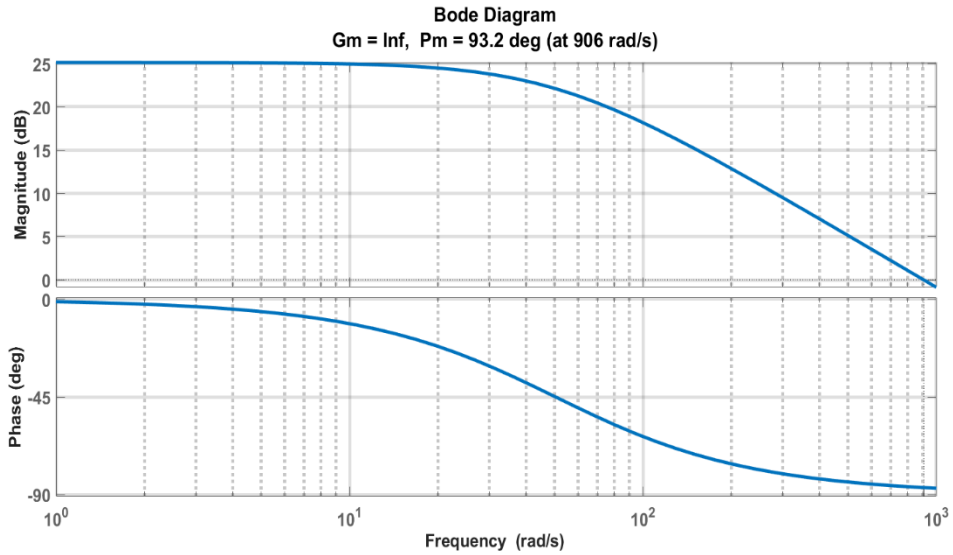

Fig.4.28. Bode Plot of Open Loop Gain ($G_{vi}(s)$) Peak Current Mode Control of DAB Converter

Once the parameters were obtained, the simulation analysis were performed for the same loading conditions

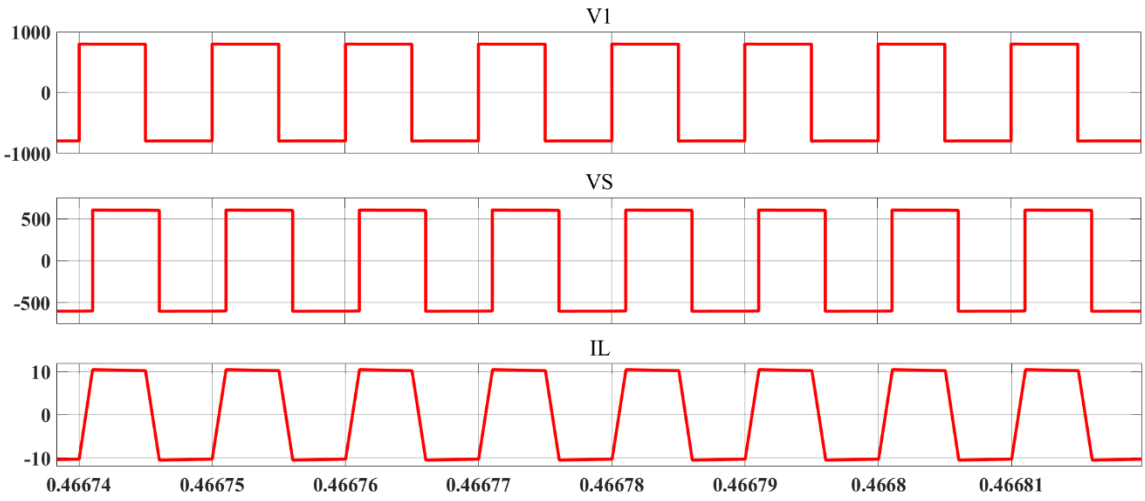

Fig.4.29. Bridge Output Voltage (V1), Transformer Primary Voltage (VP) and Inductor Current (IL) Implemented Using PCMC for 100% Loading (zoomed)

As per Fig.4.29, for rated output conditions (100% loading), for the sake of simplicity and to make transition current ($i_T = i_P$) the secondary side voltage of the transformer was referred to primary side (V_p) which makes voltages across inductor equal, and thus making slope of inductor current during interval of ($T_s/2-\emptyset$) as zero, resulting in trapezoidal waveform. And it can be seen as per the derived equation for peak current Eqn.4.34, the value of peak inductor current is equal to calculated value (10.48A).

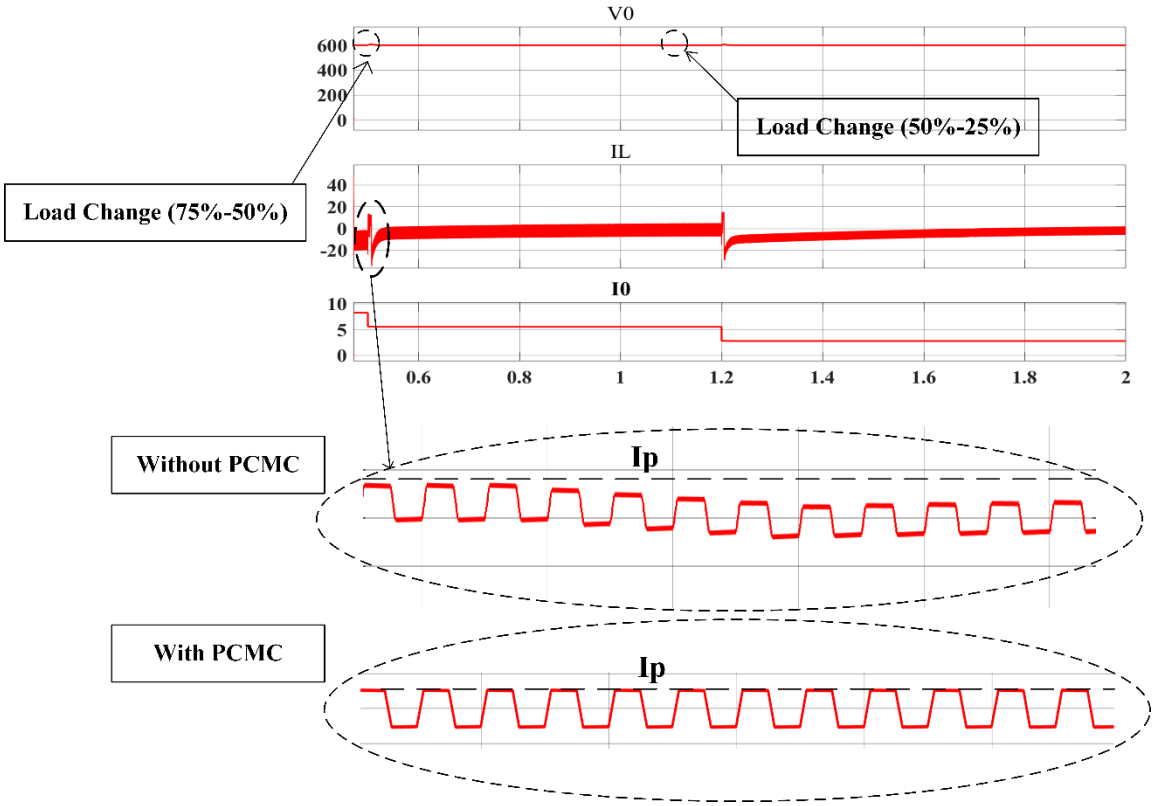

Fig.4.30. CV Mode Analysis of DAB Converter as per Design Parameters Comparison of Peak of Inductor Current During Transition Period (Without PCMC, With PCMC)

As shown in Fig.4.30 the Peak Current Mode Control was implemented on the CV mode of operation with the earlier configuration. It was observed that during the transition of load, from 75 to 50% and 50-25% the spike in inductor current was present between the transition period and settling time duration. This does not only affect the system parameters, efficiency but also increase the di/dt stresses on the switches, and magnetic components. PCMC ensures that there is a smooth transition and limiting of the peak of the current, by adjusting the phase shift accordingly for each instance by maintaining the load parameter (load voltage) constant and nature of current as desired throughout the operation. The only disadvantage PCMC holds is the complexity in execution, and simultaneous execution of processes, which needs a robust and fast control action thus demanding high bandwidth from the control loops, and robustness.

4.4 Conclusion

In the context of electric vehicle (EV) charging applications, this chapter has provided a thorough examination of control strategies for the Dual Active Bridge (DAB) converter. In order to implement typical battery charging profiles, a control architecture that supports both constant voltage (CV) and constant current (CC) modes of operation was built, building upon the modelling framework set up in the previous chapter.

With the help of two different approaches—one based on time-domain specifications like settling time and overshoot, and the other employing the traditional pole placement technique directed by crossover frequency and phase margin requirements—the chapter described the design of PI controllers for both voltage and current regulation. Every technique was examined for applicability for real-world application, design flexibility, and tuning effort. Through simulation, the controller's performance was verified, demonstrating how well the reduced-order model predicted system dynamics. Furthermore, the chapter presented Peak Current Mode Control (PCMC) as a way to improve the converter's transient response and current protection. By deriving the associated transfer function, it also offered the theoretical underpinnings for its implementation.

CHAPTER 5
EXPERIMENTAL VERIFICATION

5.1 High Level Block Diagram of Design of DAB Converter:

As shown in the Fig.5.1 the High-Level Block Diagram (HLBD) is presented, where the experimental setup for the converter is explained in detail, with highlighting the key components involved in the design.

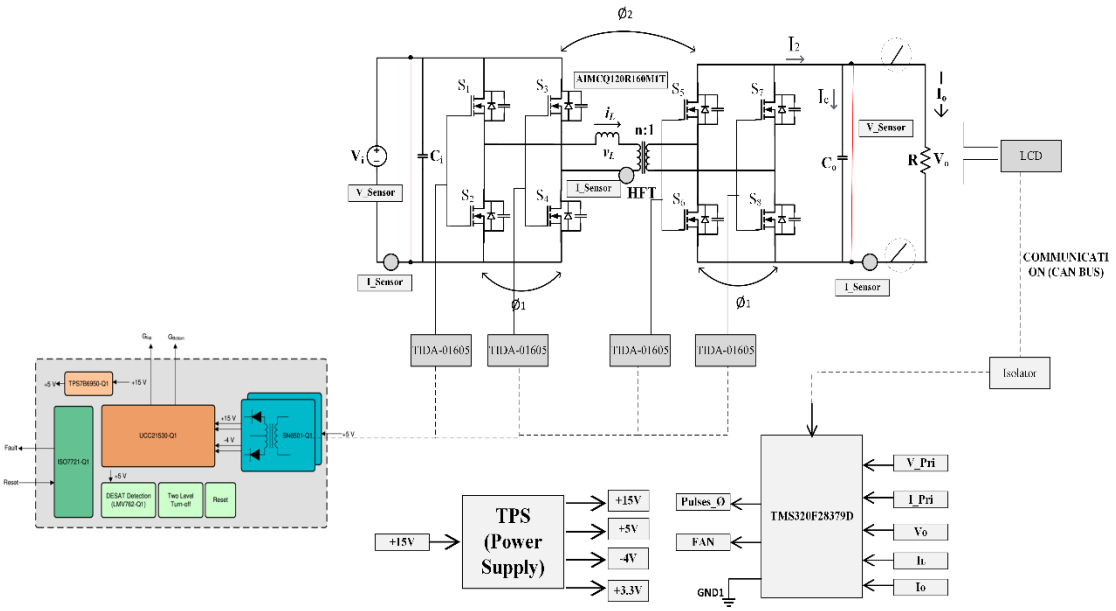

Fig.5.1 High Level Block Diagram for Design of Dual Active Bridge (DAB) Converter

- UCD3138A:

  Texas Instruments' highly integrated digital power controller, the UCD3138A, developed especially for advanced power conversion systems, including as DC-DC converters like the Dual Active Bridge (DAB). Because of its programmable control logic, integrated analog front ends, high-resolution PWM generation, and potent digital signal processing capabilities, it is perfect for implementing complex control algorithms in real time. The UCD3138A is used in this work to implement control techniques for off-board electric vehicle (EV)

charging applications, including peak current mode control (PCMC), constant voltage (CV), and constant current (CC).

The UCD3138A's Digital Pulse Width Modulator (DPWM), which enables phase-shifted and high-resolution modulation techniques required for DAB converters, is one of its primary features. Depending on the power stage needs, the DPWM module can function in a variety of modes, such as phase shift, resonant, triangular, and multi-mode. This module's deterministic timing and resolution guarantee precise power transfer control, particularly in situations with fluctuating load and battery voltage. For accurate output power regulation in this project, the primary-secondary bridge phase relationship is modulated using the phase-shift mode of DPWM.

Additionally, the controller has a strong analog front-end with adjustable signal conditioning blocks, specialized DACs for reference generation, and an Error Analog-to-Digital Converter (EADC). Implementing closed-loop control techniques requires precise feedback acquisition of output voltage and current, which these peripherals provide. Even in high-frequency switching settings, which are common in contemporary power converters, the EADC's programmable triggering, averaging, and oversampling enable steady and noise-immune signal processing.

Fig.5.2 UCD3138A Working Flow Block Diagram

Furthermore, the UCD3138A's filter and control loop modules enable the direct digital implementation of user-defined compensators, PID, or PI. Because of their high degree of configurable nature, these digital filters allow for real-time adjustment of output scaling, saturation limits, and control coefficients. Without having to reprogramme low-level code, this flexibility is essential for fine-tuning the controller during hardware testing. Fault detection, cycle-by-cycle current limiting, and programmable soft start/ramp features that increase the power stage's safety and dependability further strengthen the control loop.

5.2 Experimental Results of Open Loop Configuration:

The open loop hardware configuration of the Dual Active Bridge (DAB) converter is shown in the Fig.5.3 a bidirectional power supply is employed as the load.

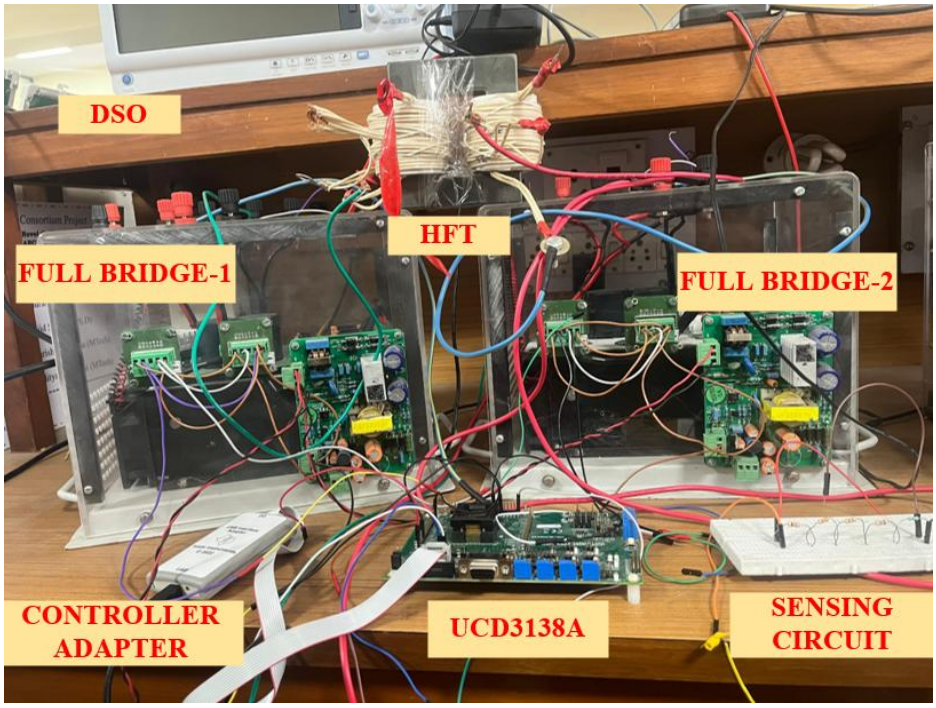

Fig.5.3 Hardware Setup of Dual Active Bridge (DAB) Converter

Table 5.1 Specification of Components

Components	Device	Rating
Bidirectional Power Supply	Chroma 62060D-600	6kW,40A
Silicon Carbide MOSFET	AIMCQ120RI160M	1200V,40mΩ
DSP Controller	Texas Instruments	UCD3138A64 OEVM
HFT	Ferrite Core	800V/800V, 25kVA, 80μH
DSO	Yokogawa	DL950

The relationship between output power and phase shift was experimentally investigated in two scenarios using the conventional Single-Phase Shift (SPS) control approach. An increase in output power is correlated with an increase in phase shift, according to the data shown in Figs. 5.4 and 5.5. The converter functions with a 1:1 voltage ratio in the first scenario and in the buck mode by altering the load in the second.

Table 5.2 Design Parameters for Hardware setup

Parameters		Case-1	Case-2
Input Voltage	V_i (volts)	100	100
Output Voltage	V_0 (volts)	100	75
Output Power	P_0 (W)	150	100
Frequency	f_s (kHz)	50	50
Inductor	L (µH)	80	80
Phase Shift	Ø (degrees)	38	38

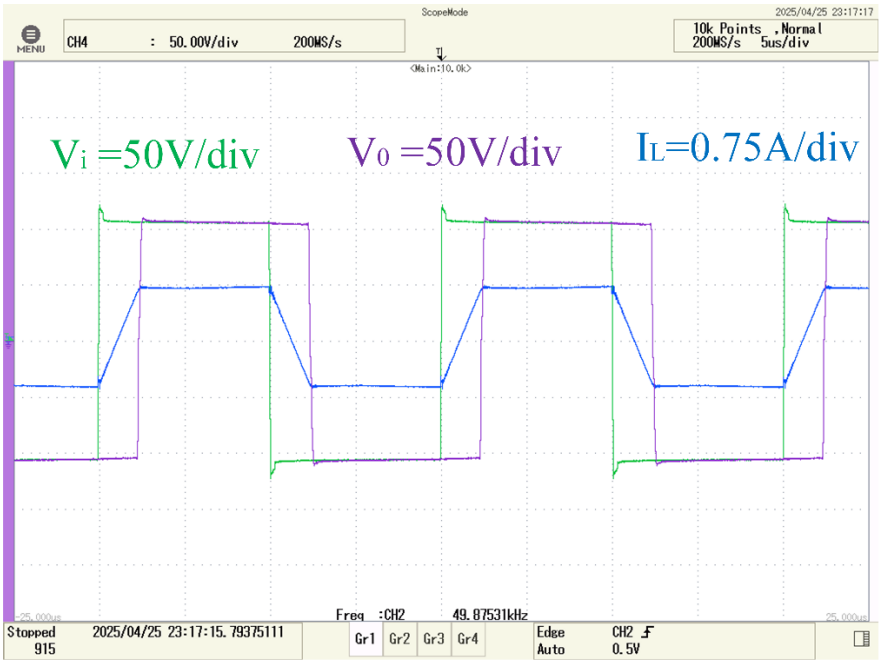

Fig.5.4 Case-1 (100/100V) Dual Active Bridge (DAB) Converter (50kHz) (Primary Side Bridge Output Voltage (V_i) Secondary Side Bridge Voltage (V_0) Inductor Current (i_L))

With a primary side input voltage of 100 V and a secondary side output voltage of 75 V, the Dual Active Bridge (DAB) converter operates in an open-loop configuration as shown by Fig.5.4. A regulated phase shift between the two square-wave voltages is seen in the figure, which displays the waveforms of the primary and secondary bridge voltages. According to the principles of phase shift modulation, this phase difference controls the power transmission from the high-frequency transformer's primary to secondary side. The precise switching edges and the square-wave structure of the voltages verify proper bridge operation and gate signal synchronization.

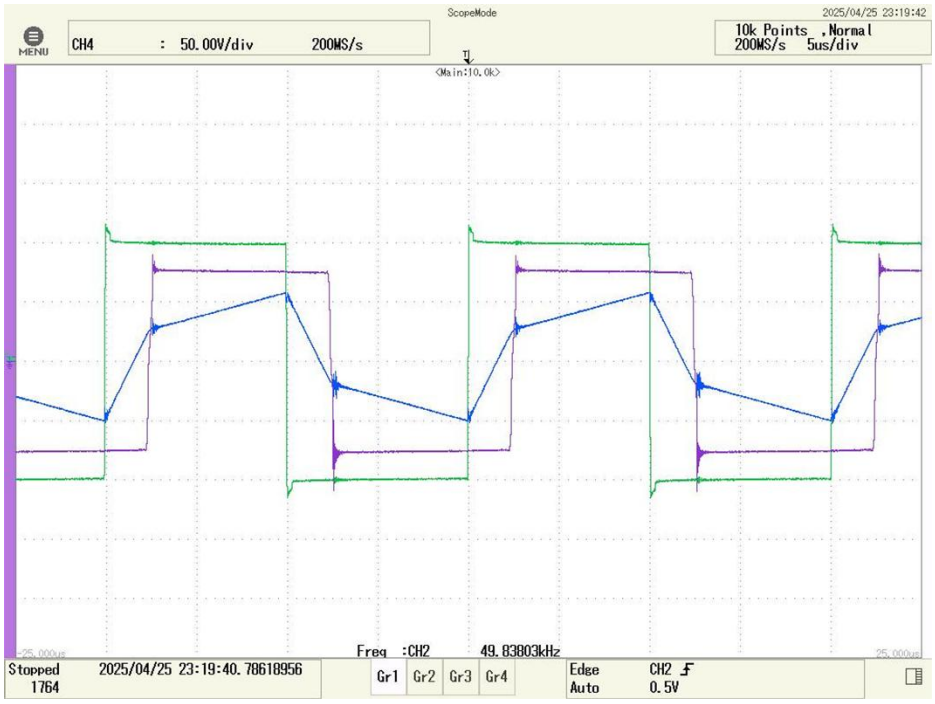

Fig.5.5 Case-2 (100/75V) Dual Active Bridge (DAB) Converter (50kHz) (Primary Side Bridge Output Voltage (V_i) Secondary Side Bridge Voltage (V_0) Inductor Current (i_L))

Since, the value of design parameters were calculated for 800/600V for the nominal values of phase shift (Ø=38°°) to fix the same values for inductor and phase shift, the voltage scale was decided to step down in the same ratio as per lab setup.

$$P_0 = \frac{nV_iV_0\emptyset(\pi - \emptyset)}{2\pi^2 fL} \tag{5.1}$$

$$P_0 = \frac{1.33 \times 800 \times 600 \times 0.663(\pi - 0.663)}{2\pi^2(100 \times 10^3)(80 \times 10^{-6})} \tag{5.2}$$

$$\boldsymbol{P_0 = 150W}$$

Hence, for a 150W output power the value of load resistance chosen is,

$$P_0 = \frac{V_0^2}{R_0} \tag{5.3}$$

$$150 = \frac{75^2}{R_0} \qquad \Rightarrow \boldsymbol{R_0 = 37.5\Omega}$$

Table 5.2 Design Parameters for Hardware setup

Parameters		Case-3	Case-3
Input Voltage	V_i (volts)	100	100
Output Voltage	V_0 (volts)	100	75
Output Power	P_0 (W)	150	100
Frequency	f_s (kHz)	100	100
Inductor	L (µH)	80	80
Phase Shift	Ø (degrees)	38	38

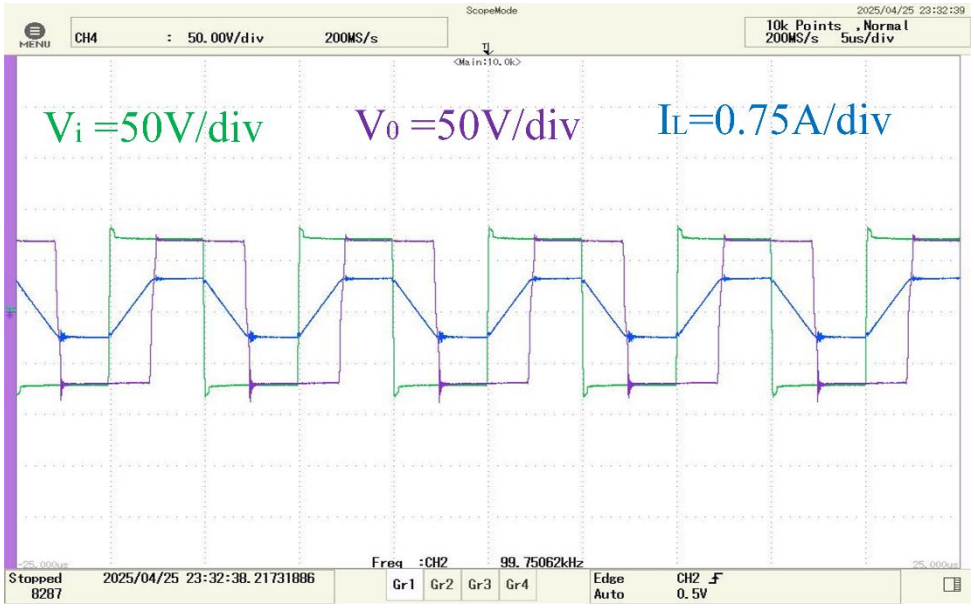

Fig.5.6 Case-3 (100/100V) Dual Active Bridge (DAB) Converter (100kHz) (Primary Side Bridge Output Voltage (V_i) Secondary Side Bridge Voltage (V_0) Inductor Current (i_L))

As shown in Fig.5.6 Both sides' symmetrical square-wave profiles show that the transformer is properly excited and that the switching process was successful. Interestingly, as would be predicted when input and output voltages are equal, there is very little phase shift between the primary and secondary voltages along with the Inductor current profile being symmetric between each timing instance. As studied in the previous chapters, the nature of inductor current matches with the slope change theory (section 2.1).

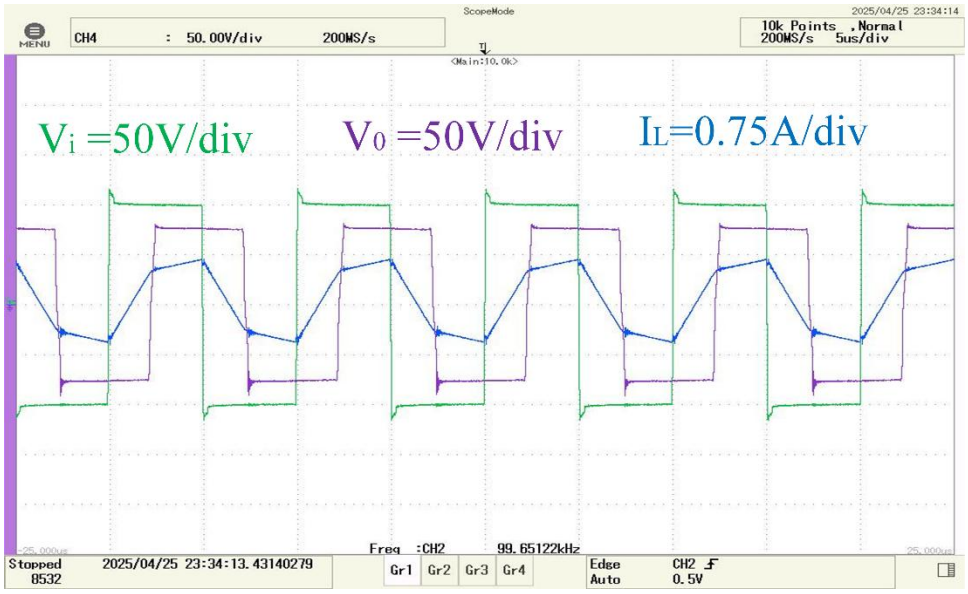

Fig.5.7 Case-4 (100/75V) Dual Active Bridge (DAB) Converter (100kHz) (Primary Side Bridge Output Voltage (V_i) Secondary Side Bridge Voltage (V_0) Inductor Current (i_L))

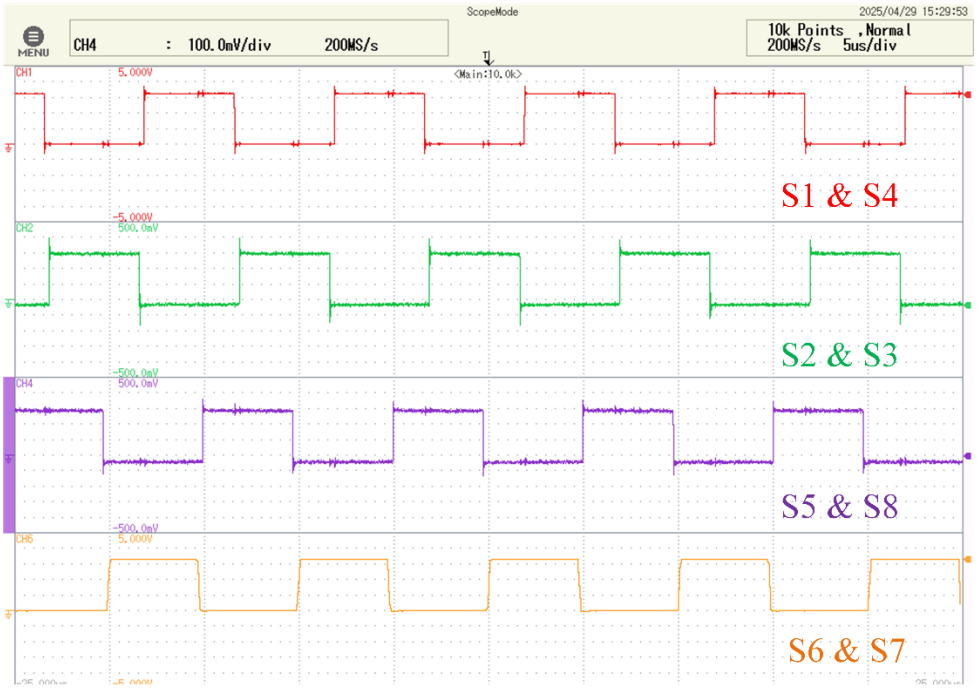

Fig.5.8 Phase Shifted Gate Signals for Switches of Dual Active Bridge (DAB) Converter (100kHz)

5.3 Conclusion:

The experimental verifications for the analysis of DAB converter operating under Single Phase Shift (SPS)control technique, as per the voltage ratio, calculated phase shift, and designing magnetics such as High Frequency Transformer (HFT) with the appropriate leakage inductance showed that the results and analytical calculations show similarity. The precise switching edges and the square-wave structure of the voltages verify proper bridge operation and gate signal synchronization.

CHAPTER 6
CONCLUSION AND FUTURE SCOPE

6.1 Conclusion:

The modelling, control, and experimental validation of a Dual Active Bridge (DAB) converter for off-board electric vehicle (EV) charging applications were thoroughly examined in this thesis. The growing need for effective, bidirectional, and galvanically separated power converters in the EV industry served as the impetus for this study. Because of their high-power density, soft-switching ability, and versatility in bidirectional power transfer, DAB converters are especially well-suited for these kinds of applications. The goal of the project was to provide a solid control strategy that was backed by both experimental validation and analytical modelling for operation of peak current mode control (PCMC), constant current (CC), and constant voltage (CV).

Electric vehicles (EVs) are becoming more and more popular, which has increased demand for high-power, bidirectional, efficient DC-DC converters that can facilitate quick and secure battery charging. The Dual Active Bridge (DAB) converter has become a viable option among many topologies because of its capacity to offer soft-switching, bidirectional power flow, and galvanic isolation. The actual implementation of an efficient control system for DAB converters that supports Peak Current Mode Control (PCMC), Constant Current (CC), and Constant Voltage (CV) is still a major obstacle, despite its potential.

The lack of a unified, workable, and experimentally proven control framework for DAB converters that can handle conventional EV charging profiles and integrate PCMC for enhanced current protection and transient performance is the main research gap this work attempts to fill. Although PCMC has been extensively studied in other converter topologies, nothing has been determined about or achieved to apply it in DAB converters, especially when combined with CC and CV modes.

Based on this, the objectives of the thesis were framed as follows:

To model the DAB converter using various modelling approaches and select a method suitable for control-oriented analysis.

- To design and implement control strategies for CC and CV modes with seamless transition capabilities based on battery state of charge (SOC).
- To investigate and derive the transfer function for PCMC in the context of a DAB converter.
- To validate the proposed control strategies using both simulation and hardware experimentation.

To achieve these objectives, the following **major contributions** were made through the course of this research:

- A comparative study of modelling techniques—reduced-order, generalized average, and discrete-time models—was conducted. The **reduced-order model** was selected for its balance of simplicity and accuracy and used as the basis for control design.
- Transfer functions for both CC and CV operation modes were derived analytically and verified using the signal injection technique in PLECS. The resulting Bode plots showed excellent agreement between theoretical and simulated responses.
- A dual-loop cascaded control architecture was proposed to handle mode switching between CC and CV modes. Two controller design techniques were investigated: One based on time-domain performance (settling time and overshoot), Another based on frequency-domain criteria (crossover frequency and pole placement).
- A new analytical model for Peak Current Mode Control (PCMC) in DAB converters was developed, filling a gap in existing literature and laying the groundwork for future hardware implementation of cycle-by-cycle current limiting.
- A hardware prototype of the DAB converter was developed using TI's UCD3138A digital controller, and experimental results were recorded for open-loop operation. The captured waveforms confirmed expected converter behaviour, validating the control structure and modelling approach.

6.2 Future Scope:

The dissertation includes Analysis, Modelling and Controller Design of Dual Active Bridge Converter considering traditional (Single Phase Shift) control technique. Furthermore, there is a scope for improvement in terms of performance and efficient operation, given below:

1. To implement closed loop control for the optimized Dual Phase Shift (DPS) control technique with Peak Current Mode Control (PCMC) in Hardware.
2. To extend the soft switching range of DAB converter under light load conditions.
3. To develop the fault tolerant optimized phase shift control of Dual Active Bridge converter.

REFERENCES

1. G. Lithesh, B. Krishna and V. Karthikeyan, "Review and Comparative Study of Bi-Directional DC-DC Converters," 2021 *IEEE International Power and Renewable Energy Conference (IPRECON)*, Kollam, India, 2021, pp. 1-6, doi: 10.1109/IPRECON52453.2021.9640712.
2. D.Das, M.J. Hossain, S. Mishra and B. Singh, “Bidirectional Power Sharing of Modular DABs to Improve Voltage Stability in DC Microgrids,” in *IEEE Transactions on Industry Applications,* vol. 58, no. 2, pp. 2369-2377, March-April 2022, doi: 10.1109/TIA.2022.3144653.
3. M. Forouzesh, Y. P. Siwakoti, S. A. Gorji, F. Blaabjerg and B. Lehman, "Step-Up DC–DC Converters: A Comprehensive Review of Voltage-Boosting Techniques, Topologies, and Applications," in *IEEE Transactions on Power Electronics*, vol. 32, no. 12, pp. 9143-9178, Dec. 2017, doi: 10.1109/TPEL.2017.2652318.
4. A. K. Rathore, D. R. Patil and D. Srinivasan, “Non-isolated bidirectional soft switching current-fed LCL resonant DC/DC converter to interface energy storage in DC microgrid,” *IEEE Trans Ind. Appl.*, vol. 52, no. 2, pp. 1711–1722, Mar./Apr. 2016.
5. R. K. Kanaparthi, J. P. Singh and M. S. Ballal, "A Review on Multi-Port Bidirectional Isolated and Non-Isolated DC-DC Converters for Renewable Applications," 2022 *IEEE International Conference on Power Electronics, Drives and Energy Systems (PEDES)*, Jaipur, India, 2022, pp. 1-6, doi: 10.1109/PEDES56012.2022.10080049.
6. M. N. Kheraluwala, R. W. Gascoigne, D. M. Divan and E. D. Baumann, "Performance characterization of a high-power dual active bridge DC-to-DC converter," in *IEEE Transactions on Industry Applications*, vol. 28, no. 6, pp. 1294-1301, Nov.-Dec. 1992
7. Zhao, Q. Song, W. Liu and Y. Sun, "Overview of Dual-Active-Bridge Isolated Bidirectional DC–DC Converter for High-Frequency-Link Power-Conversion System," in *IEEE Transactions on Power Electronics*, vol. 29, no. 8, pp. 4091-4106, Aug. 2014, doi: 10.1109/TPEL.2013.2289913.
8. R. T. Naayagi, A. J. Forsyth and R. Shuttleworth, "High-Power Bidirectional DC–DC Converter for Aerospace Applications," in *IEEE Transactions on Power Electronics*, vol. 27, no. 11, pp. 4366-4379, Nov. 2012.
9. R. W. A. A. De Doncker, D. M. Divan and M. H. Kheraluwala, "A three-phase soft-switched high-power-density DC/DC converter for high-power applications," in *IEEE*

Transactions on Industry Applications, vol. 27, no. 1, pp. 63-73, Jan.-Feb. 1991, doi: 10.1109/28.67533.

10. D. C. Pandey, P. K. Behera and M. Pattnaik, "Steady-State Analysis of Dual Active Bridge Converter with Single Phase Shift and Dual Phase Shift Modulation," *2023 IEEE International Students' Conference on Electrical, Electronics and Computer Science (SCEECS)*, Bhopal, India, 2023, pp. 1-6, doi: 10.1109/SCEECS57921.2023.10062987.
11. A. R. Rodríguez Alonso, J. Sebastian, D. G. Lamar, M. M. Hernando and A. Vazquez, "An overall study of a Dual Active Bridge for bidirectional DC/DC conversion," 2010 *IEEE Energy Conversion Congress and Exposition*, Atlanta, GA, USA, 2010, pp. 1129-1135, doi: 10.1109/ECCE.2010.5617847.
12. N. Hou, W. Song, Y. Zhu, X. Sun and W. Li, "Dynamic and static performance optimization of dual active bridge DC-DC converters," in *Journal of Modern Power Systems and Clean Energy,* vol. 6, no. 3, pp. 607-618, May 2018, doi: 10.1007/s40565-017-0343-7.
13. R. T. Naayagi, A. J. Forsyth and R. Shuttleworth, "Performance analysis of extended phase-shift control of DAB DC-DC converter for aerospace energy storage system," *2015 IEEE 11th International Conference on Power Electronics and Drive Systems*, Sydney, NSW, Australia, 2015, pp. 514-517, doi: 10.1109/PEDS.2015.7203567.
14. K. S. Parihar, W. Khan, J. A. Dar and M. K. Pathak, "Optimal Control Path for DAB Based Solid-State Transformer," in *IEEE Transactions on Industry Applications*, vol. 60, no. 1, pp. 1860-1869, Jan.-Feb. 2024, doi: 10.1109/TIA.2023.3326417.
15. A. Kumar, A. H. Bhat and P. Agarwal, "Comparative analysis of dual active bridge isolated DC to DC converter with single phase shift and extended phase shift control techniques," *2017 6th International Conference on Computer Applications In Electrical Engineering-Recent Advances (CERA)*, Roorkee, India, 2017, pp. 397-402.
16. D. Yadeo, P. Chaturvedi, H. M. Suryawanshi, D. Atkar and S. K. Saketi, "Five Level Bidirectional Dual Active Bridge with Symmetrical Configuration," IECON 2019 - *45th Annual Conference of the IEEE Industrial Electronics Society*, Lisbon, Portugal, 2019, pp. 6761-6766, doi: 10.1109/IECON.2019.8926841.
17. D. D. Atkar, P. Chaturvedi, H. M. Suryawanshi, P. P. Nachankar, D. Yadeo and S. K. Saketi, "Three-Phase Integrated-Optimized Power Electronic Transformer for Electric

Vehicle Charging Infrastructure," in *IEEE Transactions on Industry Applications*, vol. 58, no. 4, pp. 5198-5213, July-Aug. 2022, doi: 10.1109/TIA.2022.3170285.

18. . Fan, Y. Li, Y. Yuan, X. Hu and W. Dai, "Comparative Analysis of Isolated Bidirectional Dual-Active-Bridge DC-DC Converter Based on EPS and DPS," *2019 22nd International Conference on Electrical Machines and Systems (ICEMS)*, Harbin, China, 2019, pp. 1-6.
19. R. Zgheib, I. Kamwa and K. Al-Haddad, "Comparison between isolated and non-isolated DC/DC converters for bidirectional EV chargers," 2017 *IEEE International Conference on Industrial Technology (ICIT)*, Toronto, ON, Canada, 2017, pp. 515-520, doi: 10.1109/ICIT.2017.7913285.
20. L. Li, G. Xu, D. Sha, Y. Liu, Y. Sun and M. Su, "Review of Dual-Active-Bridge Converters with Topological Modifications," in *IEEE Transactions on Power Electronics*, vol. 38, no. 7, pp. 9046-9076, July 2023, doi: 10.1109/TPEL.2023.3258418.
21. A. Ranjan, A. Abhishek, B. K. Verma, S. K. Ram, S. Devassy and A. K. Dhakar, "Analysis of Dual Active Bridge Converter in Dual-Phase-Shift mode using Pulse-Width Modulation Technique," 2020 *IEEE 17th India Council International Conference (INDICON)*, New Delhi, India, 2020, pp. 1-7, doi: 10.1109/INDICON49873.2020.9342318.
22. N. Naik, C. Vyjayanthi and C. Modi, "Design, Loss Analysis and MFA Modeling of DAB-based Fast Charger for Bidirectional Grid to EV Power Transfer," 2023 *International Conference for Advancement in Technology (ICONAT)*, Goa, India, 2023, pp. 1-7, doi: 10.1109/ICONAT57137.2023.10080578.
23. P. Wang, X. Chen, C. Tong, P. Jia and C. Wen, "Research on Optimal Control Strategy for Dual Active Bridge Converter with Phase Shift Control," 2021 *IEEE 12th Energy Conversion Congress & Exposition - Asia (ECCE-Asia)*, Singapore, Singapore, 2021, pp. 1934-1939, doi: 10.1109/ECCE-Asia49820.2021.9479040.
24. H. Bai and C. Mi, "Eliminate Reactive Power and Increase System Efficiency of Isolated Bidirectional Dual-Active-Bridge DC–DC Converters Using Novel Dual-Phase-Shift Control," in *IEEE Transactions on Power Electronics*, vol. 23, no. 6, pp. 2905-2914, Nov. 2008, doi: 10.1109/TPEL.2008.2005103.
25. B. Zhao, Q. Song, W. Liu, G. Liu and Y. Zhao, "Universal High-Frequency-Link Characterization and Practical Fundamental-Optimal Strategy for Dual-Active-Bridge

DC-DC Converter Under PWM Plus Phase-Shift Control," in *IEEE Transactions on Power Electronics*, vol. 30, no. 12, pp. 6488-6494, Dec. 2015, doi: 10.1109/TPEL.2015.2430934.

26. Sharma, J.K. (2009) Operations Research: Theory and Applications. 4th Edition, Macmillan India Ltd., New Delhi.
27. S. Shao *et al*., "Modeling and Advanced Control of Dual-Active-Bridge DC–DC Converters: A Review," in *IEEE Transactions on Power Electronics*, vol. 37, no. 2, pp. 1524-1547, Feb. 2022
28. Bidirectional, Dual Active Bridge Reference Design for Level 3 Electric Vehicle Charging Stations. TIDA- 010054.
29. W. Li, W. Li, Y. Deng, and X. He, “Single-stage single-phase high-step up ZVT boost converter for fuel-cell microgrid system,” IEEE Trans. Power Electron., vol. 25, no. 12, pp. 3057–3065, Dec. 2010.
30. TEXAS INSTRUMENTS- “DAB vs CLLLC”- https://www.ti.com/document-viewer/lit/html/SSZTCW7.